POLITECNICO DI TORINO

Master of Science Course in

BIOMEDICAL ENGINEERING



Master of Science Thesis

Alginate–Poly-L-Lysine–Alginate (APA)-Encapsulated Electrogenetically Engineered Cells for Controlled Therapeutic Secretion

Supervisors

Prof. Valentina Alice CAUDA

Prof. Alessandro GRATTONI

Candidate

Davide ANDOLFI

SEPTEMBER 2026

Ai sognatori, a chi vede il bicchiere mezzo pieno,
ai poliedrici, a chi sa esserci per gli altri,
alla mia famiglia e ai miei amici,
infine a me stesso.

ABSTRACT

Engineered cell-based therapies let us use living cells as ongoing sources of important biological molecules, but it's still tough to get them working smoothly in implantable systems. The big issues are keeping the cells where they're supposed to stay, organizing them well, allowing things to move in and out, keeping them alive, and shielding them from the immune system. These challenges really matter for engineered cells that are designed to respond to specific signals - since their treatment effect depends not just on staying alive, but on still being able to detect outside cues and react with a controlled response. This thesis investigated alginate–poly-L-lysine–alginate (APA) microencapsulation as an alternative strategy for the controlled loading, confinement, and functional maintenance of electrogenetically engineered HEK293 cells intended for integration into implantable cell-based therapeutic platforms.

A reproducible fabrication workflow was developed for the production of cell-loaded alginate beads and multilayer APA microcapsules. The resulting system was characterized in terms of capsule morphology, cellular distribution, viability, recoverable cell content, molecular transport, basal secretory activity, responsiveness to chemical and electrical stimulation, and preliminary interaction with immune cells. This suggests that Adding an APA coating resulted in capsules that looked more uniform and rounded than plain alginate beads. The cells inside stayed put and kept up their metabolic activity during the culture period we tested. Experiments using fluorescent dextrans in a range of sizes showed that the APA coating remained open to dissolved macromolecules, and the speed of movement depended on how large the molecules were. When we tested how the cells functioned, those in APA capsules kept up their base-level SEAP secretion and reacted strongly when we triggered membrane depolarization. That confirmed the engineered calcium/NFAT signaling system was still working after encapsulation. Applying electrical stimulation showed the cells still responded as expected, but pushing up the stimulation made their metabolic activity drop, so it's clear the stimulation settings need some work. Preliminary macrophage and primary splenocyte co-culture experiments were additionally performed to investigate the interaction between the APA system and immune-cell populations and to identify the main limitations that must be addressed in future immunoprotection studies.

Finally, the encapsulated cellular payload was incorporated into a mesh-based implantable chamber, demonstrating practical microcapsule loading and retention together with inward accessibility of an externally applied stimulus and outward recovery of the secreted reporter. All in all, APA microencapsulation looks like a promising way to load engineered, stimulus-responsive cells into implantable

devices. It offers tight cell containment, lets molecules through as needed, keeps secretory functions intact, and works with the architectures required for these implants. But, for this strategy to really deliver on controlled cell-based therapies, more work is needed to fine-tune the electrical stimulation, check how the cells hold up over time, and make sure they're well protected from the immune system in real body conditions.

Acknowledgements

First of all, I would like to thank Professor Alessandro Grattoni for opening the doors of his laboratory to me and giving me the opportunity to spend eight months working alongside his wonderful team. I am especially grateful that he never made me feel out of place or under pressure. Instead, he gave me the freedom to work independently while making sure I always had the support I needed. This freedom encouraged my curiosity and allowed me to explore an environment that was completely new to me, but full of opportunities.
I would also like to thank Politecnico di Torino and Professor Valentina Cauda, who made it possible for me to carry out my thesis in Houston. She was also the one who convinced me not to give up on this opportunity when bureaucratic difficulties were starting to make me question whether I should leave. She always reminded me of the value of the experience I was about to have, not only from a professional and educational perspective, but also on a personal level.
A special thank you goes to Marco Maria Paci, my supervisor and the person with whom I spent most of my time in the laboratory. We shared ideas, methods, results, thoughts, and hobbies, and our relationship quickly evolved from being colleagues to becoming friends, making everything much easier. I am grateful for his humility, for always listening to me, and for bringing me along and helping me discover all the opportunities the laboratory and hospital had to offer. Throughout these eight months, he has been a role model for me in many ways, from his approach to research to the way he interacts with people in such a stimulating environment as the Grattoni Lab.
I also want to thank the Italian group in the laboratory: Elisa, Francesco, Danilo, Vincenzo, Alessio, Annarita, and Nicola. From my very first day, they welcomed me into this new world in the best possible way. Before being outstanding researchers, they are wonderful people, and I feel lucky to have met them.
My thanks also go to Ana, Gabby, Camden, Casey, Serena, Rim, Arya, Ayla, Lin, Nikitha, and Alex, who supported me and put up with my endless questions of all kinds, not to mention my not-so-perfect English!
Finally, I am grateful to Houston Methodist and the city of Houston for giving me the chance to spend eight months in such a stimulating, multicultural, and

completely new environment. This experience helped me open my mind, broaden my horizons, and discover a world I had never experienced before.

Table of Contents

List of Tables VII

List of Figures VIII

List of Abbreviations X

1 Introduction 1

1.1 Engineered Cell-Based Therapies and Cell Transplantation 1

1.1.1 Therapeutic potential of engineered cell-based approaches . . 1

1.1.2 Biological and Translational Barriers to Cell Transplantation 2

1.2 Cell Encapsulation and Immunoisolation 3

1.2.1 Principles of Cell Encapsulation and Immunoisolation 3

1.2.2 Microencapsulation, Macroencapsulation, and Hybrid Strategies 5

1.2.3 Transport and Geometric Design Constraints in Cell Encapsulation 6

1.3 Alginate-Based Cell Encapsulation 7

1.3.1 Alginate as a Cell-Encapsulation Biomaterial 7

1.3.2 Immunoisolation Properties of Alginate-Based Capsules . . . 8

1.3.3 Alginate–Poly-L-Lysine–Alginate capsule architecture 10

1.3.4 Advantages, Limitations, and Design Trade-Offs of APA Encapsulation 11

1.4 Engineered Cells for Controlled Therapeutic Secretion 12

1.4.1 Engineered Mammalian Cells as Therapeutic Platforms . . . 12

1.4.2 Stimulus-Responsive Engineered Cells 13

1.4.3 Electrically Responsive and Electrogenetic Cell Systems . . . 14

1.4.4 The Engineered HEK–SEAP Cell Model 15

1.5 Implantable Devices for Cell-Based Therapeutics 16

1.5.1 Implantable Devices Containing Engineered Cells 16

1.5.2 Electrical Actuation and Closed-Loop Integration 17

1.6 Experimental Context and Limitations of the Previous Cell-Loading Strategy . . . 19
1.6.1 Direct Cell Loading and Nanoporous Membrane Constraints 19
1.6.2 The Previous Implantable Device as an Experimental Design Case . . . 20
1.7 Rationale and Objectives of the Thesis . . . 21
1.7.1 APA Encapsulation as an Alternative Cell-Loading and Retention Strategy . . . 21
1.7.2 Specific Objectives . . . 22

2 Materials and Methods 24
2.1 Engineered HEK Cell Model and Culture . . . 24
2.1.1 Engineered HEK–SEAP Cell Line . . . 24
2.1.2 Cell Culture and Maintenance . . . 25
2.1.3 SEAP Quantification and Calibration . . . 25
2.2 Electrical Stimulation Platform . . . 27
2.2.1 C-Dish/C-PACE Electrical Characterization . . . 27
2.2.2 Preliminary Electrical Stimulation of Non-Encapsulated HEK293 Cells . . . 28
2.3 Alginate and APA Microcapsule Fabrication . . . 29
2.3.1 Cell-Free Optimization of Alginate Bead Formation . . . 29
2.3.2 Cell Encapsulation and APA Coating . . . 30
2.3.3 Capsule Standardization and Estimation of Cell Loading . . . 32
2.4 In Vitro Characterization of APA Microcapsules . . . 34
2.4.1 Morphological Characterization . . . 34
2.4.2 Cell Viability and Intracapsular Distribution . . . 34
2.4.3 Longitudinal Cell Recovery from Alginate Beads . . . 35
2.4.4 Molecular Diffusion Characterization of APA Microcapsules 36
2.5 Functional Characterization of Encapsulated Engineered HEK293 Cells . . . 38
2.5.1 Basal SEAP Secretion under Adherent, Non-Adherent, and APA-Encapsulated Conditions . . . 38
2.5.2 Chemical Depolarization with KCl . . . 40
2.5.3 Electrical Stimulation of APA-Encapsulated Cells . . . 41
2.6 In Vitro Immunocompatibility and Immunoresistance Assessment . 43
2.6.1 Preliminary RAW 264.7 Macrophage Co-Culture . . . 43
2.6.2 Primary Rat Splenocyte Challenge and Immune Activation Profiling . . . 44
2.7 BioHybrid Device Adaptation and APA Integration . . . 49
2.7.1 Previous Cellular-Chamber Configuration and Design Constraints . . . 49

2.7.2 Redesign of the Cellular Compartment and Mesh Characterization . . . 50
2.7.3 Device Assembly, Sterilization, and Preconditioning . . . 53
2.7.4 APA Microcapsule Loading into the Redesigned Device . . . 53
2.7.5 Short-Term In Vitro Assessment of SEAP Release from the Mesh-Based Device . . . 54
2.8 Data Processing and Statistical Analysis . . . 55

3 Results and Discussion 58
3.1 Preliminary Analytical and Electrical Characterization . . . 58
3.1.1 SEAP Calibration and Detector-Gain Selection . . . 58
3.1.2 C-Dish/C-PACE Electrical Characterization . . . 60
3.1.3 Preliminary Electrical Stimulation of Non-Encapsulated HEK293 Cells . . . 62
3.2 In Vitro Characterization of Alginate and APA Microcapsules . . . 64
3.2.1 Morphological Characterization . . . 64
3.2.2 Qualitative Assessment of Cell Viability within APA Microcapsules . . . 66
3.2.3 Longitudinal Cell Recovery from Alginate Beads . . . 68
3.2.4 Molecular Transport through APA Microcapsules . . . 69
3.3 Functional Characterization of Encapsulated Cells . . . 73
3.3.1 Basal SEAP Secretion and Metabolic Activity . . . 73
3.3.2 Chemical Depolarization with KCl . . . 76
3.3.3 Electrical Stimulation of APA-Encapsulated Cells . . . 77
3.4 In Vitro Immunocompatibility and Immunoresistance Assessment . 79
3.4.1 RAW 264.7 Macrophage Response to APA Microcapsules . . 79
3.4.2 Primary Rat Splenocyte Challenge . . . 81
3.5 Integration of APA Microcapsules into the Redesigned BioHybrid Device . . . 88
3.5.1 Evaluation of the 3D-Printed Retention Mesh . . . 88
3.5.2 APA Loading and Retention within the Redesigned Cellular Chamber . . . 90
3.5.3 Device-Level SEAP Release across the Mesh-Based Interface 90

4 Conclusions 93
4.1 From Encapsulation to a Functional Electrogenetic Cell Platform . 93
4.2 Integration of the APA Strategy into the BioHybrid Device . . . 95
4.3 Limitations and Concluding Remarks . . . 97

5 Future Perspectives 100
5.1 Optimization and Repetition of the Primary Splenocyte Challenge . 100

5.2 Long-Term In Vitro Validation of the APA-Loaded Device 101
5.3 Repeated Electrical Stimulation in the Fully Integrated APA Device 102
5.4 In Vivo Validation of Immunoprotection and Integrated Device Performance 103
5.5 Toward a Therapeutic and Closed-Loop BioHybrid System 105

References 107

Self-declaration on the use of generative AI 111

List of Tables

2.1 Experimental groups used for the primary rat splenocyte challenge. Cell-loaded APA microcapsules and naked engineered HEK293 cells were evaluated either alone or in the presence of primary rat splenocytes. LPS and PHA were included as positive controls for inflammatory cytokine production and T-cell activation/proliferation, respectively. 46

3.1 Linear-regression parameters obtained for the low- and high-range SEAP calibration curves at different detector gains. Concentrations for both calibration ranges are expressed in ng/mL. Gain 125, subsequently selected for cross-experiment comparisons, is highlighted in bold. 60

List of Figures

1.1 Conceptual immunoisolating function of an APA microcapsule containing engineered HEK293 cells. 9

2.1 Alginate bead formation by Ca^{2+}-mediated ionic gelation. 30
2.2 APA microcapsule fabrication and multilayer architecture. 32
2.3 Representative cell-loaded APA microcapsule after encapsulation and coating. 33
2.4 Custom platinum-mesh configuration for electrical stimulation of APA-encapsulated cells. 42
2.5 Exploded schematic of the redesigned APA-compatible BioHybrid device. 52

3.1 SEAP calibration curves acquired at detector gain 125. 59
3.2 Cell-free electrical characterization of the C-Dish/C-PACE stimulation platform. 61
3.3 Exploratory electrical stimulation of non-encapsulated engineered HEK293 cells. 63
3.4 Morphological characterization of alginate-only beads and APA microcapsules. 65
3.5 Qualitative Live/Dead assessment of APA-encapsulated engineered HEK293 cells. 67
3.6 Longitudinal recovery of engineered HEK293 cells from alginate-only beads. 69
3.7 Molecular-weight-dependent dextran penetration into APA microcapsules. 71
3.8 Representative fluorescence images of dextran penetration into APA microcapsules. 72
3.9 Basal SEAP secretion and metabolic activity under adherent, non-adherent, and APA-encapsulated conditions. 75
3.10 Response of engineered HEK293 cells to chemical depolarization with 60 mM KCl. 77

3.11 Electrical-stimulation response of APA-encapsulated engineered HEK293 cells. 79
3.12 TNF-α response of RAW 264.7 macrophages to APA microcapsules. 81
3.13 TNF-α production during the primary rat splenocyte challenge. . . 82
3.14 SEAP output during the primary rat splenocyte challenge. 84
3.15 Primary rat splenocyte viability following the 72-h immune challenge. 85
3.16 T-cell activation-associated markers during the primary rat splenocyte challenge. 86
3.17 Flow-cytometric gating strategy for primary rat splenocyte analysis. 87
3.18 Characterization of the 3D-printed retention mesh and comparison with APA capsule size. 89
3.19 Device-level SEAP release from APA-encapsulated engineered HEK293 cells. 92

List of Abbreviations

APA	Alginate–poly-L-lysine–alginate
BFP	Blue fluorescent protein
CaV1.2	L-type voltage-gated calcium channel 1.2
CFSE	Carboxyfluorescein succinimidyl ester
DMEM	Dulbecco's Modified Eagle Medium
D-PBS	Dulbecco's phosphate-buffered saline
FBS	Fetal bovine serum
HEK293	Human embryonic kidney 293 cells
IL-6	Interleukin 6
Kir2.1	Inwardly rectifying potassium channel 2.1
LLOQ	Lower limit of quantification
LPS	Lipopolysaccharide
MTT	3-(4,5-dimethylthiazol-2-yl)-2,5-diphenyltetrazolium bromide
NFAT	Nuclear factor of activated T cells
PBS	Phosphate-buffered saline
PCB	Printed circuit board
PEDOT	Poly(3,4-ethylenedioxythiophene)
PES	Polyethersulfone
PHA	Phytohemagglutinin
PLL	Poly-L-lysine
RLU	Relative light units
ROI	Region of interest
SEAP	Secreted alkaline phosphatase
TNF-α	Tumor necrosis factor alpha

Chapter 1

Introduction

1.1 Engineered Cell-Based Therapies and Cell Transplantation

1.1.1 Therapeutic potential of engineered cell-based approaches

Cell-based therapies themselves work by putting living cells to use as active treatments - restoring lost functions, replacing damaged tissues, adjusting biology, or producing important proteins right where they're needed. Instead of being single chemical doses like traditional drugs, these cells stay alive and active and keep influencing their surroundings for a long time. Depending on the disease, engineered cells might help rebuild tissue, encourage regeneration, modulate the immune system, or churn out therapeutic proteins locally. Local protein production is especially appealing for chronic illnesses: because the implanted cells have all the machinery for making and secreting proteins, they can keep up a steady supply without the ups and downs of repeated dosing - as long as they're kept alive and working the way they should be.[1, 2, 3].

Thanks to genetic engineering and synthetic biology, we can push these cells beyond what they'd normally do. You can get them to make new proteins, or sense certain signals in the body and respond in a specific, pre-set way - so the cell's state, or its environment, is linked directly to what it delivers in terms of treatment. Depending on the design, activation may occur autonomously in response to a biological signal or be imposed externally, allowing secretion to be initiated or modulated when required rather than maintained constitutively. This capacity to combine living cellular machinery with programmable regulation has made engineered cells particularly attractive for therapeutic systems in which biological production must be coupled to temporal control [1, 4, 5, 6, 7].

The source of the cells brings up a whole different set of questions. If you use the patient's own cells, you're less likely to run into immune rejection, but you have to go through the whole process - isolating, engineering, growing, and checking the cells for each person. Using donor (allogeneic) cells makes it easier to standardize and scale manufacturing, but these cells can still be attacked by the immune system. Taking cells from another species (xenogeneic) means you might have plenty of cells to work with, but you run higher risks when it comes to immune responses and biosafety. Standardized engineered cell lines are therefore appealing for the development of reproducible cellular products, although their therapeutic use depends on maintaining appropriate localization, survival, functional stability, and controlled interaction with the host [1, 2].

1.1.2 Biological and Translational Barriers to Cell Transplantation

The performance of engineered cells under controlled *in vitro* conditions does not necessarily predict their behavior after implantation. Once the graft is moved into a living body, it suddenly faces a lot it didn't deal with in culture - immune cells checking it out, inflammation, mechanical stress, and a local environment whose blood vessels and tissue makeup could look nothing like what it's used to from the lab. For cells coming from a different person (allogeneic) or species (xenogeneic), the immune system can kick in through both adaptive defenses (like T and B cells) and innate cells (macrophages and natural killers). Genetic tweaks to the cells only add more layers, since new proteins or engineered changes can make the immune response even more unpredictable. Although systemic immunosuppression can mitigate rejection, its long-term use introduces clinically relevant risks and does not eliminate inflammatory responses associated with the implanted material itself [8, 1].

The interaction between the graft, its supporting material, and the surrounding tissue creates a second layer of complexity. Protein adsorption at an implanted surface can contribute to inflammatory-cell recruitment and macrophage activation, eventually promoting foreign-body giant-cell formation, fibroblast accumulation, and extracellular-matrix deposition.If a fibrotic capsule forms around the implant, that's not just an immune problem, either. This new layer of tissue pushes the implanted cells further from the host's blood vessels, which means the body's response to this 'foreign' object also messes with how well oxygen, nutrients, and cell byproducts can get in and out. Oxygen is especially tricky - cells need it, it doesn't dissolve well, and as you cram more cells into a tight spot or add extra barriers, the risk of low oxygen (hypoxia) climbs. So, when you're trying to protect these cells, you're working in a really tight zone: make the isolation too strong, and suddenly you've starved your graft of everything it needs to stay alive and do

its job Veiseh2015, Bochenek2018, Colton2014, Farina2019. [9, 10, 11, 2].
Long-term safety and graft effectiveness also hinge on keeping control over where these cells go and how they keep acting after you put them in. If the cells aren't contained, they might wander, get washed away, or wind up somewhere unexpected - which makes tracking and removing them a headache, especially if they multiply or have been genetically engineered. Physical containment can reduce these risks and facilitate removal or replacement of the graft, but larger or more complex enclosures may themselves increase diffusion distances. Meanwhile, transgene expression, proliferation, metabolic state, and responsiveness to repeated stimulation can change over time, so a cell population that initially exhibits the desired phenotype may not maintain the same secretion profile indefinitely [2, 1].
These biological uncertainties are accompanied by manufacturing and translational requirements that become increasingly demanding as living cells are combined with biomaterials and implantable hardware. Identity, purity, viability, potency, genetic stability, sterility, and batch-to-batch reproducibility must be controlled at the cellular-product level, while the final system must also preserve compatibility between the cells and any membranes, hydrogels, electrodes, or structural components with which they interact. Immune rejection, foreign-body reactions, transport limitations, uncertain localization, and functional instability therefore cannot be treated as isolated problems; together they explain why direct implantation of engineered cells is often insufficient for applications requiring long-term localized function and why strategies that provide physical containment and immunological separation while preserving molecular exchange have become central to the development of cell-based implants [1, 4].

1.2 Cell Encapsulation and Immunoisolation

1.2.1 Principles of Cell Encapsulation and Immunoisolation

Cell encapsulation confines living therapeutic cells within a biocompatible material or semipermeable structure before implantation, establishing an artificial interface between the graft and the recipient. In the context of cell transplantation, this interface is expected to perform more than simple physical containment: it must reduce immune-mediated damage while preserving the communication required for cellular survival and function. Immunoisolation is therefore achieved through the combined action of barrier selectivity, material–host interactions, and structural containment, rather than through complete separation of the implanted cells from their biological environment [2, 12].
The most direct mechanism is physical exclusion. The dimensions and organization of the encapsulating network can restrict or prevent host immune cells from reaching and directly contacting the transplanted population, thereby limiting rejection

pathways that depend on cell–cell interaction. At the same time, the barrier still needs to let through oxygen, nutrients, ions, metabolites, normal body signals, and whatever molecules the graft releases. Just blocking things by size doesn't fully protect against immune responses. Soluble antigens from inside the capsule can slip out and trigger the host's immune system, while antibodies, parts of the complement system, cytokines, chemokines, and other immune molecules might get inside, depending on their size, shape, charge, and how they interact with the capsule material. Immunoisolation therefore depends strongly on selective molecular transport rather than simple impermeability, and the permeability required to sustain cell function may also permit indirect immune communication between graft and host [12, 8].

A second mechanism operates at the material–tissue interface itself. Before immune cells interact with an implanted capsule or membrane, proteins from blood and interstitial fluids can adsorb onto its surface and form a conditioning layer whose composition and conformation influence subsequent cellular adhesion and activation. How much of this happens comes down to the material's properties: things like surface chemistry, hydration and how easily it gets wet, charge, surface roughness, texture, how stiff it is, and whether it has spots that help cells stick. These features can tip the balance - either the surface resists cell build-up, or it encourages macrophages to stick, sparks inflammation, leads to big foreign-body giant cells, and ends up with scar tissue forming. Surface charge isn't as simple as just positive or negative; its effect depends on the entire makeup of the material. In the same way, more water-loving (hydrophilic) surfaces often help cut down on unwanted cell sticking - if the rest of the interface is designed right - but that alone isn't enough to guarantee the immune system will ignore it[2, 9].

Whether immunoisolation really works depends on how well these characteristics hold up over time. A capsule might start out blocking immune cells but lose that protection if it swells, breaks down, cracks, ends up with defects, or gets wrapped up in tough scar tissue. On the flip side, making it too tough or too closed off might keep its shape but wind up starving the cells inside or stopping the graft's outputs from escaping. Some new strategies add antifouling coatings or include local immunomodulatory ingredients to try and cut down on immune cell build-up and scarring, though how well these work still comes down to the specific material and application. Encapsulation also helps keep cells right where they're needed, stopping them from drifting away from the original implant site. Cytocompatibility, selective permeability, interfacial behavior, mechanical stability, and spatial organization must consequently be considered together when selecting an encapsulation architecture, with microencapsulation, macroencapsulation, and hybrid systems distributing these functions across different physical scales [2, 12, 13].

1.2.2 Microencapsulation, Macroencapsulation, and Hybrid Strategies

Encapsulation strategies can be distinguished according to the physical scale at which the cellular population is organized. Microencapsulation distributes cells among numerous small capsules, typically as small cellular populations or confined aggregates, whereas macroencapsulation concentrates a larger population within a single retrievable structure such as a chamber, membrane device, or hollow fiber. This difference in scale affects not only molecular transport, but also how the cellular dose is packaged, implanted, recovered, and integrated with other technological components [12, 2, 14].

Microencapsulation breaks the graft up into lots of small cell clusters, which means there's more surface area compared to volume, and molecules only need to diffuse over short distances. This setup helps the capsules interact with their surroundings and gives much shorter diffusion paths than you'd get with a big chunk of cells. Each capsule's size and make-up lets you control how the cells are spread out. But splitting everything up like this isn't all good news: getting enough cells for treatment may require implanting large numbers of capsules, which can increase the total implanted volume and make it harder to deliver them all evenly. Once implanted as free particles, capsules may also migrate, sediment, aggregate, or distribute irregularly, and complete retrieval can become challenging when long-term removal of the cellular product is required [12, 10].

Macroencapsulation adopts the opposite strategy by concentrating the graft within a single identifiable structure. This facilitates localization, mechanical protection, retrieval, and replacement, and also provides a physical framework in which membranes, electrodes, sensors, fluidic interfaces, or electronic components can be positioned relative to the cells. The resulting architecture is particularly attractive when the biological component must interact with an engineered device, although increasing the dimensions of the cellular compartment inevitably changes the spatial relationship between the cells and the surrounding tissue. Intravascular designs can exploit immediate access to the circulation but introduce thrombosis-related risks, whereas extravascular systems avoid direct blood contact at the cost of greater dependence on local tissue vascularization and implantation site [12, 2, 15].

Hybrid architectures attempt to combine the local organization of microencapsulation with the macroscopic control offered by a retrievable device. Instead of asking a single structure to perform every function, cellular protection and organization can be distributed across multiple physical levels: individual capsules define the immediate cellular microenvironment, while an external enclosure retains the capsules, determines their position, and supports integration with stimulation or sensing hardware. This strategy is especially relevant to implantable cell-based systems, including biohybrid platforms, in which the biological payload must remain locally

organized without sacrificing the possibility of device retrieval or technological control. The platform investigated in this thesis follows this general architecture by combining microencapsulated engineered cells with a macroscopic compartment designed to provide mechanical retention and electrical access [4].

1.2.3 Transport and Geometric Design Constraints in Cell Encapsulation

Once a cellular barrier has been selected, its suitability cannot be established from nominal pore size or molecular-weight cut-off alone. The rate at which a molecule crosses an encapsulation system depends on the effective diffusivity and permeability of the material, which are influenced by barrier thickness, porosity, tortuosity, network organization, chemical composition, charge, and interactions between the diffusing species and the matrix. The relevant transport distance also extends beyond the encapsulating material itself. Depending on the architecture, oxygen, nutrients, metabolites, signaling molecules, and secreted products may encounter surrounding tissue, protein or fibrotic deposits, a device wall, the encapsulating matrix, and the cellular compartment in sequence. These elements behave as successive transport resistances, so improving one highly permeable component cannot compensate for a strongly restrictive interface elsewhere in the pathway [2, 12].

Among the molecules required for cell survival, oxygen frequently imposes the most stringent constraint because it has limited solubility in aqueous biological environments and is continuously consumed by the cellular population. The resulting concentration profile reflects not only material permeability but also local vascularization and oxygen tension, cellular consumption rate, cell density, and the distance separating individual cells from the external supply. Geometry ties directly into how things move around. Spherical microcapsules have the bonus of a good surface-area-to-volume balance, letting substances pass through across the whole surface. But this only works up to a point: when you make the capsules bigger, the path for anything trying to reach the cells in the middle gets longer, so you can end up with steep concentration differences inside, even if the outer layer lets things through easily. The same kind of issue shows up when cells start to grow into dense clumps or get packed unevenly. Suddenly, the cells in some areas want a lot more resources, even though the capsule itself hasn't changed size. Capsule diameter, cell loading, spatial organization, and material permeability must consequently be considered as coupled variables rather than optimized independently[11, 4].

The transport environment is also dynamic rather than fixed at the time of fabrication. Hydrogel swelling or degradation, changes in cell density and organization, protein accumulation, and fibrotic tissue formation can alter diffusion pathways after implantation, while inadequate oxygenation may itself damage cells and

promote the release of inflammatory signals that further modify the surrounding interface. For engineered cells meant to react to specific triggers, there's more to consider. All the activating chemicals or ions still need to reach every cell, and whatever product the cells make has to get out of the capsule quickly enough to do its job. In systems that use electric signals to trigger a response, the makeup and water content of the matrix around the cells matter, too, since they shape the environment where the stimulation actually happens. Effective encapsulation design must therefore reconcile short transport distances and sufficient permeability with cellular containment, mechanical stability, and preservation of the functional input–output pathway of the engineered cells [4].

1.3 Alginate-Based Cell Encapsulation

1.3.1 Alginate as a Cell-Encapsulation Biomaterial

Alginate is a naturally derived anionic polysaccharide obtained mainly from brown algae, although it can also be produced by bacterial species such as *Azotobacter* and *Pseudomonas*. Its linear chains are composed of β-D-mannuronic acid (M) and α-L-guluronic acid (G) residues organized into M-rich, G-rich, and alternating sequences; because the abundance and distribution of these blocks depend on the biological source and extraction process, alginate cannot be regarded as a chemically uniform biomaterial. Differences in M/G composition, molecular weight, and chain organization are reflected in properties such as solution viscosity, gelation behavior, elasticity, permeability, and stability [16, 12]. Hydrogels like alginate are commonly used for cell encapsulation because you can form them under gentle, water-based conditions. The process relies on divalent cations bonding with the negatively charged carboxyl groups along neighboring polymer chains. This creates a three-dimensional structure - often called the "egg-box" model - that lets you mix cells right into the starting solution and trap them, all without using high heat, organic solvents, or harsh chemicals. The resulting gel is highly formulation-dependent, since alginate composition and concentration, molecular weight, crosslinking conditions, and cation identity collectively determine its mechanical and transport properties [16, 12].

Cell-encapsulation formulations contain a relatively small polymer fraction, leaving the crosslinked network highly hydrated and filled predominantly by an aqueous electrolyte. This characteristic provides an environment compatible with molecular and ionic exchange and is especially relevant to the electrically responsive system considered in this thesis. Alginate itself doesn't conduct electricity like a metal or a conjugated polymer. In a hydrated hydrogel, electrical current mainly moves by ions flowing through the water within. So, an alginate capsule isn't exactly an insulating barrier; things like the way it's made, how crosslinked the hydrogel is, its

shape, local ion concentrations, and any added coatings all play a part in shaping the electrical environment the encapsulated cells feel. Consistent with this behavior, electrogenetic studies have demonstrated that engineered mammalian cells can retain responsiveness to electrical stimulation after alginate-based encapsulation [17, 4].
The versatility of alginate is inseparable from this formulation dependence. G-rich compositions generally produce stiffer networks, whereas M-rich formulations tend toward softer and more elastic gels, and calcium-crosslinked matrices may progressively lose stability through ionic exchange under physiological conditions. Material purity is equally consequential: residual proteins, polyphenols, endotoxins, and other contaminants can stimulate innate immune responses and contribute to the substantial variation reported between alginate preparations. When sufficiently purified and appropriately formulated, alginate also presents few native mammalian cell-adhesion motifs, a property that becomes particularly relevant when the material is used as an interface between an encapsulated graft and host tissue [16, 12, 18].

1.3.2 Immunoisolation Properties of Alginate-Based Capsules

The immunoisolating behavior of alginate is closely linked to the physicochemical nature of its interface with biological fluids. In addition to forming a hydrated semipermeable network that physically confines the cellular population, unmodified alginate contains few native mammalian cell-adhesion motifs and generally provides a poor substrate for stable mammalian cell attachment in the absence of additional adhesive functionalization. The carboxylate groups in the polymer chains of alginate grab onto water, making the surface stay very hydrated. This can make it harder for sticky protein layers to form and cling on. Because these same groups give alginate a net negative charge, they affect how the material interacts at the surface, influencing things like how much water it holds, how it reacts with ions, and how proteins stick. But it isn't just the surface charge that matters for how the body responds - other things play a part too, like the details of the polymer's chemistry, how pure it is, its physical properties, and the surrounding conditions in the body. These characteristics are advantageous for the host compatibility of an immunoisolating interface because limiting stable protein adsorption and host-cell anchoring can interfere with the sequence that otherwise progresses from macrophage adhesion and activation to foreign-body giant-cell formation, fibroblast recruitment, extracellular-matrix deposition, and pericapsular fibrosis [12, 9].
This behavior should not, however, be interpreted as an intrinsic or absolute "stealth" property of alginate. Protein adsorption and inflammatory-cell accumulation can still occur, and the host response is strongly influenced by polymer

purity, surface chemistry and charge, roughness, mechanical properties, capsule dimensions, crosslinking conditions, and implantation site. Residual contaminants may themselves activate innate immune pathways, while macrophages and other inflammatory cells positioned around capsules without extensive surface overgrowth can release cytokines and additional soluble mediators capable of diffusing through the hydrogel and affecting the encapsulated graft. The effectiveness of alginate-based immunoisolation therefore depends not simply on preventing direct cellular contact, but on maintaining a sufficiently benign and stable host–material interface throughout implantation [12, 9, 19].
These competing requirements are schematically summarized in Figure 1.1, which illustrates the intended balance between cellular confinement and molecular exchange in an APA-based immunoisolation strategy.

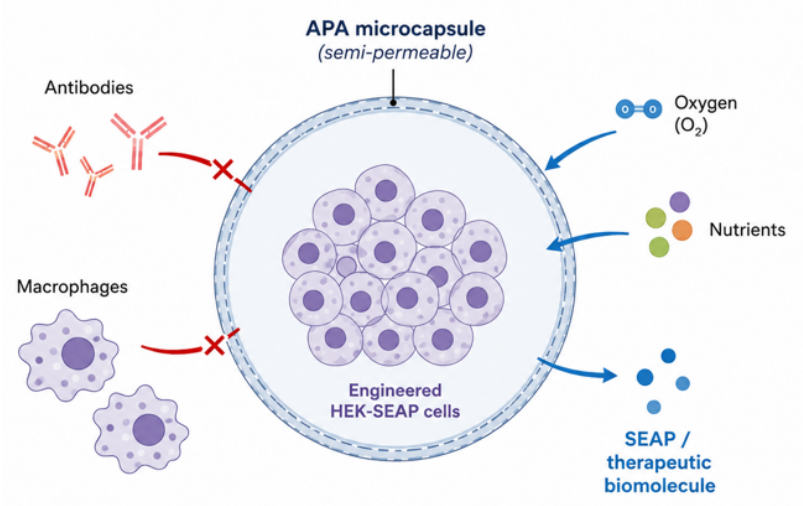


Figure 1.1: Conceptual representation of the intended immunoisolating function of an APA microcapsule containing engineered HEK293 cells. The capsule itself puts a physical barrier between the cells inside and the host's immune cells, but it's still porous enough for small stuff - like oxygen, nutrients, and molecules the cells release (such as SEAP) - to get through. The diagram is meant to show the basic idea behind this encapsulation, but it's not suggesting the capsule blocks every single immune molecule; how much gets through will depend on what the capsule is made of and the size and properties of those molecules.

The importance of formulation is evident experimentally. In non-human primates, conventional alginate formulations have been associated with substantial cellular attachment and pericapsular fibrotic overgrowth, whereas selected chemically modified alginate spheres produced a markedly reduced foreign-body response [13]. Bochenek and colleagues showed that allogeneic pancreatic islets encapsulated within an optimized alginate formulation could remain viable and glucose-responsive for up to four months without systemic immunosuppression, illustrating that functional

immunoisolation is achievable when macrophage recruitment and fibrotic deposition are sufficiently controlled [10]. At the same time, these results emphasize that alginate itself does not guarantee immune protection and that biological performance depends on the complete capsule formulation. For applications requiring additional mechanical reinforcement and control over macromolecular transport, the ionically crosslinked alginate core can therefore be combined with an interfacial polycationic layer, giving rise to multilayer architectures such as alginate–poly-L-lysine–alginate capsules.

1.3.3 Alginate–Poly-L-Lysine–Alginate capsule architecture

Alginate-poly-L-lysine-alginate (APA) capsules start with an ionically crosslinked alginate bead, then add a polycationic layer that holds everything together and changes how large molecules move through the structure. First, the alginate core is formed with cells inside. Next, poly-L-lysine (PLL), which is positively charged, is applied to the negatively charged alginate - so the lysine's protonated groups and alginate's carboxylate groups stick together electrostatically, creating a polyelectrolyte layer. This process should not be interpreted as the deposition of a completely independent membrane onto an otherwise unchanged hydrogel: PLL can penetrate the peripheral region of the alginate network, producing an interpenetrating alginate–PLL interface whose thickness and organization depend on the properties of both polymers and on the coating conditions [12, 2].
The final alginate treatment has both structural and biological relevance. Additional alginate interacts with residual cationic groups associated with the PLL-rich interface and establishes a hydrated, predominantly anionic external surface, thereby reducing direct exposure of the surrounding biological environment to the polycation. This masking function is important because free or insufficiently complexed PLL can interact strongly with negatively charged cellular membranes and biological macromolecules and has been associated with cytotoxic and inflammatory effects. APA capsules are consequently better understood as a functional multilayer architecture rather than as three perfectly discrete concentric shells: the inner alginate-rich region accommodates the cellular payload, the alginate–PLL interphase contributes to mechanical reinforcement and permeability control, and the outer alginate-rich interface modulates the interaction between the capsule and the host environment. The properties of this architecture depend on alginate composition, PLL molecular weight and concentration, incubation time, washing conditions, coating uniformity, and overall capsule dimensions [12, 8, 2, 20, 21].
The compatibility of this structure with electrically controlled cellular systems has already been demonstrated in an electrogenetic context. In the DART platform, engineered human cells enclosed within APA microcapsules remained functional after implantation and could be activated by externally applied electrical stimulation

to induce production of an encoded output. The underlying mechanism differed from the voltage-gated calcium pathway used in the present work, relying instead on electrically generated reactive oxygen species and downstream redox-sensitive signaling, but the study provides an important precedent showing that APA encapsulation can coexist with cellular containment, molecular exchange, and electrically triggered gene regulation within the same implantable electrogenetic system [17].

1.3.4 Advantages, Limitations, and Design Trade-Offs of APA Encapsulation

APA encapsulation offers a degree of tunability that is difficult to obtain with an uncoated ionically crosslinked alginate bead. The mechanics, how easily substances pass through, what the capsule surface feels like, and even the way cells inside interact with their surroundings - all of these can be tweaked just by changing the types of polymers or the way they're processed. That's useful, but it also creates complications. If you adjust the formulation to make the capsule stronger, you might introduce new problems. For example, reinforcing the interface can help the capsule hold its shape and keep cells inside, but if you make it too dense, it gets harder for molecules to move through. On the other hand, if you keep it very permeable, it may allow molecules to move freely but won't protect the cells as well or keep the capsule stable. So, APA capsule design isn't about making one property as strong as possible; it's really about finding that sweet spot - balancing stability, accessibility to molecules, compatibility with cells, and some level of immune shielding. [12, 2].

This balance is touchy, too. Even small shifts in how you make the capsules - like changing the alginate's composition or thickness, how many cells you add, crosslinking methods, the PLL's features, how long you coat, or how thoroughly you wash - can affect several properties at once. For an electrically responsive cellular system, this variability has an additional functional consequence: changes in capsule geometry, hydration, ionic composition, and interfacial structure may influence not only cell survival and outward product transport but also the electrical environment through which stimulation reaches the encapsulated population. The suitability of an APA formulation for an electrogenetic implant must consequently be demonstrated experimentally rather than inferred from its composition alone, with evaluation encompassing reproducible fabrication, cellular viability and function, molecular transport, host compatibility, and responsiveness to the intended electrical stimulus [17, 4].

1.4 Engineered Cells for Controlled Therapeutic Secretion

1.4.1 Engineered Mammalian Cells as Therapeutic Platforms

Mammalian cells are particularly suited to engineered secretory systems because they combine the biosynthetic machinery required for transcription, translation, post-translational processing, and secretion with endogenous signaling networks that can be repurposed for synthetic control. Receptors, ion channels, transcription factors, synthetic promoters, and output transgenes can be introduced or reorganized so that a native intracellular pathway becomes part of an artificial input–output connection. In this sense, the cell functions as a programmable biological chassis: the engineered components define how an input is detected and coupled to the cellular machinery, while the mammalian host supplies much of the molecular infrastructure required to process that signal and produce the encoded protein. Such modularity allows sensing, signaling, and output functions to be modified independently to a certain extent, providing a flexible basis for regulated protein production [1, 4].

Among mammalian platforms, HEK293-derived cells are widely used in synthetic biology because they are readily expanded, tolerate genetic manipulation, and support robust recombinant protein expression. Their endogenous signaling pathways can be interfaced with heterologous receptors and ion channels, making them particularly useful for constructing systems in which an externally imposed stimulus must ultimately regulate transcription. HEK293 cells have consequently served as hosts for several electrically controlled gene-expression strategies, including systems based on membrane depolarization and voltage-gated ion channels as well as electrochemical approaches that activate endogenous redox-sensitive pathways [15, 17, 4]. In this setting, the real value isn't about duplicating what a specialized secretory tissue does. It's about having a cell background you can tweak, control, and test - a setup where you can build a specific input-output pathway, keep outside variables in check, and really figure out how it works.

Once you've got a well-characterized engineered cell line, the perks for consistency are pretty clear. You can grow more cells from the same starting batch, run all your experiments under the same culture and stimulation setup, and reliably compare things like baseline activity, response strength, cell survival, and how stable the function stays over time. But just having the right genetic construct isn't enough for everything to fall into place. Cells can vary even when the DNA is the same - through differences in clones, gene silencing, changes in how fast they grow, metabolism tweaks, or even from keeping them in culture too long. Any

of those can mess with their behavior. So, you've got to check whether the link between stimulus and biological output actually holds up in the conditions you care about. For applications that rely on controlled secretion, this means a lot rides on getting the stimulus-responsive circuit right - that's the part of the cell that detects an input and flips on the relevant gene expression.

1.4.2 Stimulus-Responsive Engineered Cells

Stimulus-responsive engineered cells are designed so that a defined input is coupled to a measurable biological output through an intracellular regulatory pathway. Conceptually, the system can be divided into sensing, signal-processing, and output functions, although these elements may rely on both engineered components and endogenous cellular machinery rather than existing as completely independent modules. The triggering signal may be chemical, physiological, or physical, and regulation can be implemented at different stages of the cellular response. Physical control of engineered mammalian cells has been demonstrated using light, radiofrequency or magnetic fields, mechanically generated piezoelectric signals, and direct electrical or electrochemical stimulation, illustrating the breadth of externally addressable cellular interfaces [3, 7, 22, 23, 15, 17].Circuits based on transcription tie the stimulus to promoter activity and protein synthesis, so you get stronger and longer-lasting output, but you also have to deal with the inevitable lag from writing, translating, processing proteins, and finally secreting them. If you use post-transcriptional or post-translational methods instead, you can act much faster - by tweaking things like protein stability, turning proteins on or off, holding them inside the cell, or quickly releasing something you've already made before. The regulatory architecture must therefore be matched to the timescale and magnitude of the response required for the intended application [1, 4].
The functional performance of a responsive circuit cannot be established simply by demonstrating an increase in output after stimulation. A useful system must be characterized in terms of basal activity, activation threshold, dynamic range, dose dependence, response kinetics, reversibility, and reproducibility across repeated stimulation cycles. These factors all influence each other: cutting down on basal production makes sense if you want to avoid constant secretion, but you still need a system that can turn on reliably when needed. If background levels get too low, you risk losing that responsiveness. Pushing the intensity or length of stimulation can boost output, though only up to a point - cell stress, cell death, or triggering other unwanted cell pathways can start to cancel out any benefits. Even within the same batch, cells can vary in how much of the transgene they express, their metabolism, or how much stimulus they actually get, so the overall response gets even patchier. Optimization therefore involves identifying an operating range in which output is sufficiently strong and reproducible without compromising the

cellular state required for sustained or repeated function [1, 4].
When responsive cells are encapsulated or incorporated into an implant, circuit performance can no longer be interpreted independently of the surrounding material. The activating stimulus must reach the cells under conditions sufficient to trigger the engineered pathway, whereas the resulting secreted product must subsequently cross the cellular microenvironment and any additional material interfaces before it can be detected or exert its intended effect. So, any changes in what you measure might show more than just what's happening inside the synthetic circuit - they could also be picking up differences in transport, where the cells are, whether they're still alive, or how the stimulus interacts with whatever's around the cells. Physical cues offer an appealing solution here because they can be created and adjusted from outside the system. Of these, electrical stimulation stands out: it works well with electronic hardware and lets you set specifics like how strong, how long, what pattern, and how often you stimulate. Its use with engineered mammalian cells, however, requires a mechanism through which the applied electrical input is converted into a signal that the cellular machinery can recognize and process [4, 5].

1.4.3 Electrically Responsive and Electrogenetic Cell Systems

Electrogenetics provides a functional interface between electronic hardware and genetically engineered cells, allowing an electrical input to regulate cellular behavior, gene expression, or secretion.Making these systems work together means you have to translate between very different ways of moving signals around. Electronics move electric charge, but mammalian cells deal mostly with ions, membrane voltage changes, second messengers, and all sorts of chemical signaling. So, the electrical signal from an electrode somehow has to get turned into something a cell can recognize and react to. There are two main ways to do this. Electrophysiological approaches modify membrane excitability so that electrical stimulation alters the membrane potential and activates intracellular signaling; Krawczyk and colleagues demonstrated this concept in engineered mammalian cells by coupling membrane depolarization to a voltage-gated calcium response and subsequent control of gene expression [15, 23]. Electrochemical approaches instead exploit molecular species generated at the electrode. In the DART platform, direct-current stimulation induces electrochemical generation of reactive oxygen species that activate the endogenous KEAP1–NRF2 pathway, allowing an electrochemical event to regulate synthetic gene expression; the same concept was subsequently applied to implanted microencapsulated engineered human cells for electrically controlled insulin production [17]. More recently, the EMPOWER platform extended redox-responsive electrogenetic control to a wireless magneto-electrogenetic configuration, in which

low-frequency electromagnetic fields act through multiferroic nanoparticles to generate intracellular ROS and activate KEAP1–NRF2-dependent transgene expression in APA-encapsulated engineered cells [24].
Each method brings its own challenges when connecting biology with electronics. For electrophysiological coupling, you've got to get the cell's membrane to polarize just right, have the ion channels actually working, and pick stimulation settings that shift the membrane potential enough - while keeping the cell alive. On the other hand, electrochemical systems rely on finely tuned reactions at the electrode, producing just enough signaling molecules to affect the cell but not so much that it becomes toxic. In both cases, electrode geometry, stimulation intensity and duration, waveform, and the ionic and electrical characteristics of the surrounding medium influence the magnitude and reproducibility of the cellular response [4, 5]. The platform investigated in this thesis belongs to the electrophysiological category: electrical stimulation is translated into membrane depolarization and calcium-dependent intracellular signaling, while the specific molecular architecture responsible for this conversion is defined by the engineered HEK–SEAP model.

1.4.4 The Engineered HEK–SEAP Cell Model

The cellular model employed in this thesis derives from the depolarization-responsive HEK platform developed by Krawczyk and colleagues. Its electrical sensitivity depends principally on coordinated expression of the inwardly rectifying potassium channel Kir2.1 and the L-type voltage-gated calcium channel CaV1.2. Kir2.1 helps keep the cell's resting membrane potential more negative, which makes it harder for CaV1.2 channels to open by default. That means there's less of a baseline flow through the pathway, so SEAP expression stays low until you really stimulate the system - as seen in the original setup, where adding Kir2.1 cut down on background SEAP activity and sharpened the response when it was triggered [15].
MWhen the membrane depolarizes, CaV1.2 channels open, letting calcium from outside the cell rush in. The spike in calcium gets picked up by calmodulin, which turns on the enzyme calcineurin. Calcineurin strips phosphates off NFAT, which then moves into the nucleus and switches on a synthetic promoter linked to the transgene output. The applied electrical stimulus is thus translated through two successive domains of signal transduction—first from membrane voltage to intracellular Ca^{2+} and then from Ca^{2+} signaling to transcription—rather than acting directly on gene expression [15].
In the present model, secreted alkaline phosphatase (SEAP) serves as the extracellular reporter of circuit activation rather than as the ultimate therapeutic product. Its secretion permits repeated quantification from culture supernatants without disrupting the cellular population, but the measured concentration should be interpreted as the integrated outcome of NFAT activation, transcription, translation,

protein processing, secretion, and subsequent extracellular transport. SEAP acts as a reporter for this whole electrogenetic pathway, but its signal comes with some lag - it responds much later than the membrane changes themselves. The initial system showed that how strong or long you stimulate it matters; SEAP output ramped up over a few hours and could drop off again if you stopped the trigger[15]. You can also trigger the same signaling pathway without electrodes, just by chemically depolarizing the cells with extra KCl in the media. Upping the amount of potassium outside the cell flattens the potassium gradient across the membrane, making it easier to depolarize and activate CaV1.2 - no electrode needed. without requiring the electrode interface. KCl can consequently be used as a functional control to distinguish failure of the cellular depolarization–Ca^{2+}–NFAT machinery from insufficient or variable electrical stimulation. The original electrogenetic study used KCl-depolarized cells alongside electrically stimulated and unstimulated conditions when characterizing SEAP output [15].
This distinction becomes particularly important after encapsulation. A change in extracellular SEAP does not uniquely report the magnitude of the electrical field experienced by the cells: cell number and viability, basal circuit activity, channel functionality, transcriptional state, secretion efficiency, and transport through the surrounding hydrogel can all modify the final measured signal. In this thesis, the HEK–SEAP platform therefore serves simultaneously as the electrically responsive biological component and as a functional probe through which the effects of encapsulation and stimulation on the complete input–output pathway can be evaluated.

1.5 Implantable Devices for Cell-Based Therapeutics

1.5.1 Implantable Devices Containing Engineered Cells

Implantable devices containing engineered cells differ fundamentally from conventional drug-delivery implants because their biological output is produced by a living cellular component rather than supplied exclusively from a finite preloaded reservoir. Depending on the engineered circuit, production may occur constitutively or be regulated in response to physiological or externally applied signals. The implant must therefore support two systems with very different requirements: cells need an aqueous environment compatible with metabolism, molecular exchange, and long-term function, whereas structural and electronic components must remain mechanically stable and, where necessary, isolated from physiological fluids. From an electronic-design perspective, chronic implantation additionally requires stable barrier materials that limit water and ion ingress into circuitry and interconnects, since

exposure of electronic components to the wet, ion-rich physiological environment can promote degradation, short circuits, and unintended electrochemical reactions [25]. Membranes, hydrogels, porous enclosures, meshes, electrodes, and packaging elements consequently cannot be considered independent additions around the cellular payload; together they determine its spatial organization, its access to the surrounding biological environment, and its relationship with the technological components of the implant. This interdependence between living cells, biomaterials, and engineered hardware defines the biohybrid character of such systems and makes device performance a property of the integrated architecture rather than of any single subsystem [4, 2, 6, 26].
For engineered cells (like allogeneic ones), the whole setup has to make sure you maintain physical control over what the cells are doing. Keeping them confined on a larger scale stops them from drifting away unchecked, and makes it possible to find, remove, or swap out the graft if something goes wrong. Physically separating the cells from the technology (like electrodes or sensors) also means you can optimize both parts without them interfering with each other's needs. If you're using external controls, having everything contained means you always know where the cells are compared to the electrodes and such - so you don't get weird, random stimulation just because a few cells wandered off. So, an implantable device that holds engineered cells isn't just there for protection; it's setting up the direct line between your cells, the host, and any artificial control you want to use. Electrogenetic implants, in which engineered cells are maintained in proximity to stimulation electrodes and electronically controlled actuation systems, represent a direct application of this integrated organization[15, 6, 26, 4].

1.5.2 Electrical Actuation and Closed-Loop Integration

Electrical actuation provides a programmable means of regulating the biological component of an electrogenetic implant, but the stimulus experienced by the cells depends on the complete electrode–cell interface rather than on the programmed electrical parameters alone. Electrode material, geometry, exposed surface area, spacing, and orientation influence current distribution and the electrical environment established across the cellular compartment, while the position and spatial organization of the cells determine how uniformly that stimulus is experienced. Configurations in which the biological compartment is located between opposing electrodes can provide a defined stimulation geometry, provided that electrode spacing and cellular distribution remain controlled. Porous or mesh electrodes may be particularly useful in cell-containing systems because they can provide a relatively large electroactive interface while preserving fluid continuity through the biological compartment. At the same time, stimulation electronics and electrical connections must remain protected from physiological fluids without compromising

the electrode interface with the cells. Electrical performance therefore emerges from the coordinated design of electrodes, biomaterials, cellular organization, and device packaging rather than from stimulation voltage or current in isolation [15, 23, 4, 5].

Wireless or remotely controlled operation extends this principle by allowing stimulation to be initiated or modified after implantation without permanent transcutaneous electrical connections. Depending on the architecture, implanted electronics may receive power, control commands, or both from an extracorporeal system and subsequently generate the required electrical stimulus locally within the cellular compartment. Such configurations preserve external control over cellular activation while maintaining the biological and electronic components within an implanted platform [6, 7, 15, 26, 4]. Power architecture is therefore a central design constraint: conventional implanted batteries impose finite lifetime and volume requirements, whereas battery-free and wirelessly powered bioelectronics can reduce the implanted hardware burden by transferring or harvesting energy only when required [27].

Remote activation, however, should not be considered equivalent to closed-loop therapeutic control. In an open-loop configuration, stimulation is delivered according to a predefined schedule or external command without being automatically adjusted on the basis of physiological feedback. Closed-loop systems go a step further: they include sensors and controllers to watch a physiological variable, process its signal, and use that info to adjust when and how hard the cells get stimulated. The engineered cells answer back by producing the desired biological effect, which can then change the very variable the system is tracking - making the loop complete. This architecture combines the rapid sensing, computation, and temporal precision of electronics with the capacity of living cells to synthesize complex biological molecules, but it also introduces dependencies across the entire chain from sensing and signal processing to electrical delivery, cellular activation, secretion, and therapeutic action. Closed-loop performance therefore requires reliable operation of the complete feedback pathway rather than successful electrical stimulation alone [4, 5]. Practical implementations have begun to demonstrate this principle: smartphone-linked optogenetic systems have coupled glucose measurements to engineered-cell activation, while more recent metabolic fuel-cell platforms have used glucose itself both as the physiological input and as the energy source for activating insulin-secreting engineered cells [7, 28].

1.6 Experimental Context and Limitations of the Previous Cell-Loading Strategy

1.6.1 Direct Cell Loading and Nanoporous Membrane Constraints

The development of the encapsulation-based strategy investigated in this thesis originated from limitations encountered when engineered cells were introduced directly into an implantable electrical-stimulation chamber as a free suspension. In the previous configuration, approximately 40,000 cells were loaded into the space defined by two parallel platinum-mesh electrodes and subsequently left undisturbed in an attempt to promote their distribution and interaction with the PEDOT-coated electrode surfaces. In practice, getting the cell population to stick well to the PEDOT interface didn't work out. Without a scaffold or some other way to keep the cells in place, their position and the way they organized themselves ended up unpredictable. That wasn't just a loading headache - it also messed with stimulation, since electrical exposure changed depending on where the cells ended up relative to the electrodes.

Direct loading also placed most of the burden of cellular containment and immunological separation on the external interface of the device. The previous chamber was closed by a polyethersulfone membrane with a nominal pore size of 30 nm, selected to retain the cellular population and limit direct interaction with the host while permitting molecular exchange. Direct permeability or mass-transfer properties of the PES membrane were not successfully quantified in isolation. Nevertheless, experimental observations were consistent with restricted outward molecular exchange across the overall device–environment pathway: SEAP accumulated at relatively high levels within the cellular chamber while substantially lower concentrations were recovered outside the device. In subsequent *in vivo* experiments, circulating SEAP was also low or below the detection threshold, although systemic dilution, distribution, and clearance prevent this observation from being attributed specifically to membrane transport. The discrepancy between internal production and external recovery therefore supported the presence of substantial transport resistance somewhere along the device–environment pathway without allowing the isolated contribution or permeability of the PES membrane itself to be determined. Cell survival deteriorated concurrently, with the naked-cell population failing to remain viable beyond approximately one week. The limited movement of substances across the device interface might have played a role in the drop, since it could block oxygen and nutrients from getting in or keep waste from being cleared out, but that idea wasn't tested on its own. There was also the environment around the electrode inside the device to consider. Early versions were smaller and held less

medium, but exposed cells to more PEDOT. Later designs cut down the amount of PEDOT and upped the medium volume. This made us wonder if keeping cells next to the electrode coating for a long time might hurt their survival, though we didn't actually pin down how much PEDOT alone was to blame compared to other aspects of the device.
The old approach exposed a mix of problems rather than just one main issue: loading cells directly didn't give enough control over how they organized, while the same large-scale interface also had to keep the cells in, keep them apart from the host, and let molecules pass through. Trying to do all these jobs at once clearly led to compromises. The resulting coupling between protective and transport functions provided the experimental rationale for relocating part of the cellular organization and protection from the device boundary to the cellular payload itself.

1.6.2 The Previous Implantable Device as an Experimental Design Case

The previous BioHybrid device translated the general principles of a cell-containing electrogenetic implant into a compact architecture in which the biological and electronic compartments were physically distinct but functionally connected. This device measured about 39.7 mm long, 22.7 mm at its widest point, and 6 mm thick. The upper round part, roughly 20.5 mm across, held the battery and electronics. Below that, a square chamber for cells took up a 13 mm x 13 mm space. Inside the chamber, two platinum-mesh electrodes, each around 1 cm2 and spaced about 2 mm apart, sat facing each other so that the cells ended up between them. These electrodes were coated with a PEDOT hydrogel, which made for better electrical contact and also narrowed the mesh openings to help keep the cells in place. Each electrode was wired to the electronics compartment next door, which was sealed off from the fluid chamber to protect the battery and circuitry.
Two silicone ports gave access to the cell chamber, making it possible to load cells, fill the chamber, and let air out as needed. During development, smaller and larger device configurations contained approximately 0.6 and 1.8 mL of culture medium, respectively, while the target cellular load remained approximately 40,000 cells per device. The host-facing side of the chamber was closed by a PES membrane with a nominal pore size of 0.03 μm and an exposed area of approximately 1.56 cm^2. Electrical stimulation could then be initiated remotely through a smartphone-controlled electronic system, creating an externally actuated configuration in which the cellular population could be stimulated after implantation without direct physical access to the device.
This architecture demonstrated the feasibility of combining a defined electrode geometry, remote electrical control, and a confined engineered-cell compartment within the same implant. At the same time, cellular performance depended strongly

on a small number of multifunctional interfaces: the platinum/PEDOT electrodes contributed to both stimulation and attempted cell retention, whereas the external nanoporous membrane simultaneously served as the principal containment and host-separation barrier while also mediating molecular exchange with the surrounding environment. The limitations described above therefore arose not from the absence of technological integration, but from the concentration of several biological and engineering functions within the same macroscopic device elements.

1.7 Rationale and Objectives of the Thesis

1.7.1 APA Encapsulation as an Alternative Cell-Loading and Retention Strategy

The limitations identified in the previous BioHybrid configuration indicated that the problem could not be addressed simply by modifying a single device component. Direct loading made cellular retention, spatial organization, and immunological separation strongly dependent on the macroscopic chamber, thereby coupling biological protection to the restrictive external membrane required to contain the naked-cell population. The strategy investigated in this thesis instead transfers a substantial part of the cellular confinement and organization, together with the candidate immunoisolating function, to the cellular payload itself. The engineered HEK cells were packed into alginate-poly-L-lysine-alginate microcapsules. The hydrogel in these capsules kept the cells confined in three dimensions, stopped them from spreading out too much, and created a moist, semipermeable barrier. This barrier separated the engineered cells from direct contact, with host cells while still allowing molecules to pass through. Because the APA capsules provide cellular confinement and are intended to serve as the principal immunoisolating interface, the macroscopic enclosure no longer requires nanometer-scale pores solely to prevent cell escape. In the redesigned concept, capsules predominantly within an approximate diameter range of 300–700 μm are retained by a nylon mesh with nominal openings of approximately 100 μm, so that the mesh functions primarily as a mechanical retaining structure rather than as the main immunoisolating barrier. The transition from the 30 nm PES membrane to this more open interface replaces a nanoporous macroscopic barrier with a capsule-retention structure while retaining transport resistance associated with the APA capsule itself. Host cells can consequently approach the APA capsules through the mesh openings, making the integrity and host–material interactions of the capsule surface central to the intended immunoisolating function.

With this setup, the device boundary took on a new function compared to the earlier version where cells were not encapsulated. That earlier design used about

40,000 engineered HEK293 cells per device, which acted as the standard when developing the APA (alginate-poly-L-lysine-alginate) microcapsule method. But, in the final short-term feasibility test, they didn't stick to that specific cell count. Instead, they worked at the batch level, counting capsules and estimating how many cells could be recovered, and put more focus on loading and keeping the capsules inside the device than on matching the old cell dose exactly. This approach allowed practical loading and retention of the encapsulated cellular payload, together with functional exchange between the internal cellular compartment and the surrounding environment, to be evaluated within the redesigned mesh-based architecture.

1.7.2 Specific Objectives

The overall objective of this thesis was to develop and experimentally evaluate APA microencapsulation as an encapsulation-based cell-loading strategy for electrogenetically engineered HEK cells, with subsequent proof-of-concept integration into an implantable electrical-stimulation chamber. The work addressed the encapsulation strategy as an integrated biological and engineering problem, with emphasis on fabrication reproducibility, cellular confinement and organization, molecular transport, preservation of cellular and secretory function, responsiveness to chemical and electrical stimulation, preliminary interaction with immune-cell populations, and practical compatibility with an implantable device architecture.
More specifically, the study aimed to establish a reproducible workflow for producing alginate beads and APA microcapsules containing engineered HEK–SEAP cells and to compare the morphology of alginate-only beads with that of the final APA architecture. To estimate how many cells could be recovered, they broke open alginate-only beads, while microscopy and Live/Dead analysis were used to check cell distribution and overall viability inside the capsules. Cell metabolism was tested separately as another sign of function. They also checked how well molecules could move through by using fluorescent dextrans of different sizes, and then measured if the engineered traits held up by looking at basal SEAP secretion, chemically triggered depolarization, and electrical stimulation. The interaction between cell-containing capsules and immune cells was subsequently examined first with RAW 264.7 macrophages and then with primary rat splenocytes, providing a preliminary assessment of immunocompatibility and immune-mediated interactions rather than definitive evidence of long-term immunoprotection. In parallel, the BioHybrid cellular chamber was used as an experimental integration case for microcapsule loading and retention: an initial configuration based on an integrated 3D-printed mesh was evaluated, and insufficient printing fidelity motivated the subsequent use of a separate nylon mesh with approximately 100 μm openings. Collectively, these objectives were designed to determine whether APA microencapsulation could

provide a reproducible and functionally suitable cell-loading strategy for stimulus-responsive engineered cells and whether the resulting encapsulated payload could be practically integrated into an implantable electrogenetic architecture, while identifying the biological and engineering limitations that remain to be addressed for longer-term application.

Chapter 2

Materials and Methods

2.1 Engineered HEK Cell Model and Culture

2.1.1 Engineered HEK–SEAP Cell Line

The principal cellular model used throughout this study was an engineered HEK293 cell line carrying a membrane-depolarization-responsive calcium/NFAT transcriptional circuit and expressing human placental secreted alkaline phosphatase (SEAP) as the reporter output. The electrosensitive architecture comprised the full L-type voltage-gated calcium channel CaV1.2, composed of the pore-forming α1C subunit together with the auxiliary α2/δ1 and β3 subunits, and the inwardly rectifying potassium channel Kir2.1. The channel components were encoded by Sleeping Beauty transposon constructs designed for SB100X-mediated genomic integration: pKK66 contained a constitutively expressed α1C–P2A–Kir2.1 cassette together with blue fluorescent protein (BFP) and puromycin-resistance markers, whereas pMX251 encoded constitutive expression of α2/δ1–P2A–β3 together with dTomato and blasticidin resistance. The reporter module consisted of a Ca^{2+}-responsive P_{NFAT3}-driven SEAP expression unit (pMX57, P_{NFAT3}–SEAP–pA), in which the synthetic P_{NFAT3} promoter contains tandem NFAT-responsive elements [15].
Kir2.1 contributes to maintaining a hyperpolarized resting membrane potential, thereby limiting basal activation of CaV1.2. Following membrane depolarization, CaV1.2 opening promotes extracellular Ca^{2+} influx. The resulting increase in cytosolic calcium activates calmodulin and the calcium-dependent phosphatase calcineurin, leading to NFAT dephosphorylation and nuclear translocation. Nuclear NFAT subsequently activates the P_{NFAT3} promoter, coupling membrane depolarization to SEAP transcription and secretion.
SEAP released into the extracellular medium was used throughout the experimental work as the principal functional readout of activation of the engineered pathway. Its secretion allowed cellular output to be quantified directly from collected culture

supernatants without disrupting the cellular population. Functional responsiveness of the engineered cells was investigated using both electrically induced membrane depolarization and chemical depolarization by increasing extracellular KCl concentration, while SEAP output was quantified using the chemiluminescent assay described in Section 2.1.3.

2.1.2 Cell Culture and Maintenance

Engineered HEK293 cells were maintained in high-glucose Dulbecco's Modified Eagle Medium (DMEM) supplemented with 10% fetal bovine serum (FBS) and 1% penicillin–streptomycin. Cells were cultured at 37 °C in a humidified atmosphere containing 5% CO_2 and routinely monitored by bright-field microscopy. Cultures were passaged at approximately 80% confluence to maintain the cells in an actively proliferating state. To limit variability associated with prolonged in vitro propagation, cultures were maintained for a maximum of approximately 12 passages after thawing. Once this passage range was reached, cultures were replaced with cells from a freshly thawed cryovial containing approximately 1×10^6 cells.
For regular passaging, cells were lifted using 0.05% trypsin-EDTA with about 0.53 mM EDTA. Once detached, complete DMEM was added to stop the trypsin, and the cell mixture was collected and spun down for 5 minutes at around 400-500 ×g. The supernatant was removed and the remaining cell pellet was resuspended in fresh complete medium, either for expansion or for experiments. Cell count and viability were checked with trypan blue and an automated cell counter. Cell suspensions were mixed 1:1 with trypan blue before analysis, and the viable-cell concentration obtained from the measurement was used to calculate the cell number required for reseeding and individual experiments.

2.1.3 SEAP Quantification and Calibration

SEAP released into the culture medium was quantified using the NovaBright™ Secreted Placental Alkaline Phosphatase (SEAP) Enzyme Reporter Gene Chemiluminescent Detection System 2.0. Conditioned-medium samples were collected at experiment-specific time points and stored at −80 °C when analysis was not performed on the day of collection. Before assay preparation, frozen samples were thawed, gently mixed, and briefly centrifuged to remove bubbles or suspended debris. Assay Buffer and Reaction Buffer were equilibrated to room temperature before use, with the Reaction Buffer maintained protected from light. Twenty-five microliters of each sample were transferred to a white 96-well chemiluminescence plate in technical duplicate. After addition of 50 μL of Assay Buffer, samples were heat-treated at 65 °C for 5 min and subsequently allowed to return to room temperature. Fifty microliters of Reaction Buffer were then added, and the plate

was incubated for 20 min at room temperature protected from light. Chemiluminescence was measured as relative light units (RLU) using a PlateRunner luminometer, with medium-only wells processed in parallel as blanks.
The quantitative response of the assay was characterized using the control enzyme supplied with the NovaBright kit. The control-enzyme stock, supplied at 300 ng/mL, was initially diluted to a 10 ng/mL working solution using the same culture-medium matrix used for the experimental samples. Two calibration ranges were subsequently prepared by 1:2 serial dilution. The high-range curve comprised 10, 5, 2.5, 1.25, 0.625, and 0.3125 ng/mL, whereas the low-range curve comprised 1, 0.5, 0.25, 0.125, 0.0625, and 0.03125 ng/mL. Each concentration was analyzed in triplicate together with distributed matrix blanks.
Calibration plates were acquired using multiple detector-gain settings to assess sensitivity, linearity, and detector saturation across the two concentration ranges. Gain settings evaluated during assay characterization included 100, 110, 125, 150, 175, 200, 225 and 255. AutoGain measurements were additionally acquired during individual experimental runs to optimize signal acquisition within the intensity range of a given plate. Because AutoGain could select different amplification settings between independent measurements, raw RLU values obtained using different gain settings were not directly compared across experiments.
Calibration data were handled separately for each detector gain and concentration range. For each standard measurement, the average signal from the matrix blanks was subtracted to get the blank-corrected chemiluminescent signal (RLU_{net}). For every concentration, the mean, standard deviation, and coefficient of variation were worked out from the three repeated measurements. High and low calibration curves were fit on their own using linear regression, following the equation

$$RLU_{\mathrm{net}} = mC + b,$$

where C is the SEAP concentration, m is the slope, and b is the intercept. For each curve, the coefficient of determination (R^2) was also calculated. TThe quantifiable range for each detector gain was set by looking at how clearly the signal stood out from the blanks, the consistency between repeats, the linearity of the calibration, and whether detector saturation was avoided. This way, the practical quantification window could be established for each detector gain.
In the end, a fixed gain of 125 was chosen for comparing different experiments, since it offered enough sensitivity and kept the measurement signals safely below the detector's saturation limit. Measurements acquired using other gain settings were retained for calibration characterization and assessment of assay performance but were not directly combined with gain-125 RLU values for quantitative comparison.

2.2 Electrical Stimulation Platform

2.2.1 C-Dish/C-PACE Electrical Characterization

Electrical stimulation experiments were initially performed using C-Dish electrode platforms connected to a C-PACE EM tissue-culture stimulator. The setup gave us a reliable way to test how engineered HEK293 cells respond to electrical signals and to look at how different stimulation strengths and exposure times affect them. The range of settings we got from this initial work helped shape later tests using a custom electrode layout in the BioHybrid device. Since things like the shape and spacing of the electrodes, the area in contact with the medium, the amount of liquid, and the way the current spreads out weren't the same in both test setups, we treated the stimulation values from the C-Dish as reference points instead of using them directly for the BioHybrid device. In the 6-well format, the C-Dish electrodes faced each other about 2.3 cm apart. The electrical pulses sent through them had two phases: 2 ms positive, then 2 ms negative, at a 10 Hz frequency. Before working with cells, we first checked how the C-Dish behaved electrically without any cells present. We tried out two different versions: the C-Dish 95 and the older C-Dish 40. Including both allowed us to see if differences between the two would affect the way current was delivered, and to check if the electrical response was similar in each design under the same test settings. For these tests, we used either PBS or DMEM at 2 or 5 mL per well. We increased the stimulation in steps - 1, 5, 10, 20, and 32 V - but only powered up one well at a time so we could measure the current for that specific spot. Three replicate measurements ($n = 3$) were acquired for each voltage, medium, volume, and C-Dish configuration.
A 30 Ω shunt resistor was connected in series with the stimulation circuit, and the voltage drop across the resistor was measured using a UNI-T UT-P30 differential probe connected to a Keysight InfiniiVision DSOX1204G oscilloscope. Peak current was calculated from the measured voltage drop according to

$$I_{\text{peak}} = \frac{V_{R,\text{peak}}}{30\ \Omega}.$$

Current–voltage relationships were generated separately for each medium, volume, and C-Dish configuration and analyzed by linear regression, providing an electrical calibration reference for subsequent cellular stimulation experiments.
A nominal electric field could be estimated from the applied voltage and the approximately 2.3 cm electrode separation. However, this geometric estimate was not considered an accurate representation of the field experienced by the cells because only part of the electrodes was immersed in the culture medium and the resulting electric field within the well was spatially non-uniform. Consequently, measured peak current under the relevant DMEM and volume conditions was

considered a more informative experimental descriptor of the delivered stimulation than the nominal voltage-to-distance ratio alone.

2.2.2 Preliminary Electrical Stimulation of Non-Encapsulated HEK293 Cells

To characterize the electrical responsiveness of the engineered HEK293 cells before encapsulation, a series of exploratory stimulation experiments was performed in tissue-culture-treated 6-well plates using the C-Dish/C-PACE system. Cells were seeded at 3×10^5 cells per well in 2 mL of complete HEK culture medium approximately 24–48 h before stimulation and maintained at 37 °C and 5% CO_2. On Day 0, the culture medium was replaced with 5 mL of fresh complete medium per well before insertion of the C-Dish electrodes. Electrical stimulation was delivered using the biphasic waveform described in Section 2.2.1, consisting of a 2 ms positive phase followed by a 2 ms negative phase at 10 Hz.

Voltage amplitude and stimulation duration were investigated through sequential voltage-series experiments performed during exploratory optimization of the stimulation protocol. Separate experiments were carried out using voltages of 2, 7.5, 10, 20, and 40 V. For each voltage, groups received electrical stimulation at that level for either 1, 4, 8, or 24 hours. Each condition included in the comparison was tested three times. Since these voltage tests were set up as independent exploratory runs, not as parts of a larger balanced experiment, results were always compared within each run against its own control samples. The C-Dish electrodes remained immersed in the culture medium for a total of 24 h in all electrode-containing groups, regardless of active stimulation duration. At the end of the assigned 1, 4, or 8 h stimulation period, electrical output was switched off while the electrodes remained immersed until the common 24 h removal time. The 24 h group remained actively stimulated until electrode removal.

Each voltage-series experiment included an unstimulated-electrode control (US), in which the C-Dish remained immersed for 24 h without electrical stimulation, an untreated control containing cells without electrodes, and a chemical-depolarization control exposed to 60 mM KCl. Medium-only wells were included for background correction. The US condition served as the primary within-run reference for evaluation of the effect of active electrical stimulation, while the untreated and KCl-treated groups provided additional basal and chemical-depolarization controls. SEAP-containing supernatant was collected at 24 and 96 h after initiation of stimulation. At 24 h, 100 μL of culture supernatant were collected from each well following removal of the C-Dish platforms and stored at $-80\,^{\circ}$C. No medium replacement was performed after this collection, and the cells remained in the original culture medium until the final endpoint. At 96 h, 1 mL of supernatant was collected for the second SEAP measurement. The 96 h SEAP endpoint was

not acquired for the 2 V voltage series because the corresponding 24 h screening measurements showed only a weak response during the exploratory optimization phase. Samples were subsequently analyzed using the chemiluminescent SEAP assay described in Section 2.1.3. For comparative presentation within and across the independently performed voltage-series experiments, SEAP values were normalized to the corresponding within-run US condition, defined as 100%.
Following the final SEAP collection at 96 h, cellular metabolic activity was evaluated using the MTT assay. The remaining culture medium was removed and replaced with 1 mL of fresh complete medium, after which 100 μL of MTT reagent were added to each well, corresponding to a 1:10 reagent-to-medium ratio. Plates were incubated for 4 hours at 37°C with 5% CO_2, giving metabolically active cells time to reduce tetrazolium and form formazan crystals. After incubation, the MTT-containing medium was removed, and 2 mL of isopropanol was added to each well. The plates were then shaken at 250 rpm for 10 minutes to dissolve the formazan. Absorbance was measured directly from 6-well plates using a Synergy H1 microplate reader set at 570 nm, with readings at 690 nm used to correct for background. Corrected metabolic activity was calculated as $A_{570} - A_{690}$. Medium-only wells were subjected to the complete MTT procedure and used for blank correction. For comparison across voltage-series experiments, metabolic activity was normalized to the corresponding US condition, defined as 100%.

2.3 Alginate and APA Microcapsule Fabrication

2.3.1 Cell-Free Optimization of Alginate Bead Formation

Before encapsulating engineered HEK293 cells, the bead-generation process was optimized under cell-free conditions to identify fabrication parameters capable of producing reproducible and morphologically consistent alginate beads. A standard-viscosity sodium alginate (350–550 mPa·s) was prepared at 1.0% (w/v) in 0.9% (w/v) NaCl. The alginate solution was loaded into a syringe mounted vertically on a syringe pump and extruded through a 32G needle. The final standardized operating conditions consisted of a flow rate of approximately 3 mL/min and a needle-to-bath distance of approximately 8 cm. Alginate droplets were collected in approximately 20 mL of 100 mM $CaCl_2$, maintained under gentle magnetic stirring at approximately 400 rpm without formation of a vortex. Upon contact with Ca^{2+} ions, the droplets underwent ionic gelation and formed hydrogel beads. After completion of extrusion, the beads remained in the $CaCl_2$ bath for an additional 5 min before recovery by gravity sedimentation and subsequent washing in 0.9% NaCl.
The principle of alginate bead generation used throughout the experimental workflow is schematically illustrated in Figure 2.1. Extrusion of sodium alginate into the

$CaCl_2$ bath promotes Ca^{2+}-mediated ionic crosslinking of neighboring alginate chains, resulting in rapid formation of the three-dimensional hydrogel network.

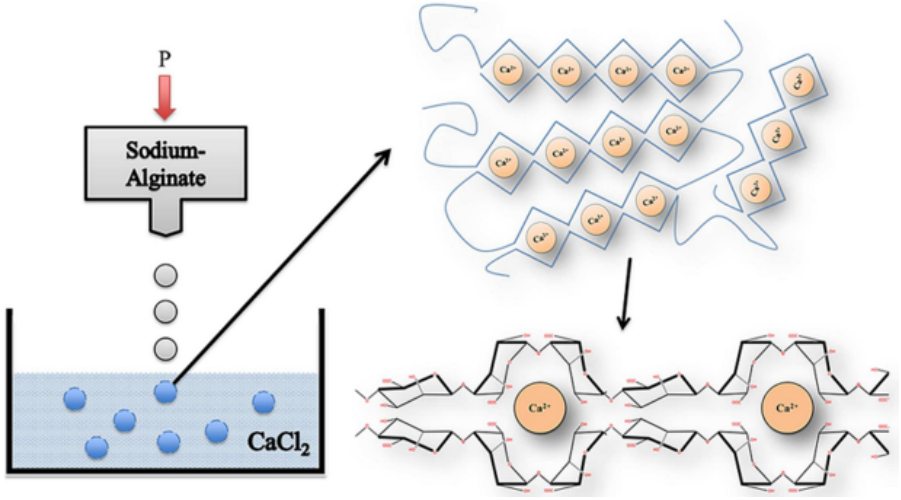


Figure 2.1: Schematic representation of alginate bead formation by Ca^{2+}-mediated ionic gelation. Sodium alginate is extruded into a $CaCl_2$ gelling bath, where divalent Ca^{2+} ions interact with neighboring alginate chains and promote formation of the crosslinked hydrogel network. The schematic illustrates the general principle underlying the syringe-pump-based bead-generation procedure used in this study.

The final fabrication parameters were selected through an iterative optimization process performed before the introduction of cells. Next, cell-free batches were made while adjusting key factors for droplet creation, such as needle gauge, flow rate, distance from needle to bath, and stirring speed. Each batch was checked with bright-field microscopy right after fabrication. Bead diameter was the main factor used to fine-tune the process, along with circularity, shape consistency, and how reliably the batches could be reproduced. Once a set of conditions reliably gave spherical beads in the desired size range and with little variation in shape, these same syringe-pump settings were moved over to sterile work in the biosafety cabinet for cell encapsulation.

2.3.2 Cell Encapsulation and APA Coating

Following optimization of the cell-free fabrication process, the same syringe-pump configuration was transferred to sterile conditions for encapsulation of engineered HEK293 cells. Sterile 1.0% (w/v) sodium alginate prepared in 0.9% (w/v) NaCl was degassed before contact with the cells to minimize bubble formation during mixing and bead generation. Cells were harvested, counted, pelleted, and gently resuspended directly in the degassed alginate. The resulting cell–alginate suspension was transferred to the syringe while minimizing material loss and was extruded using

the standardized parameters described in Section 2.3.1: vertical syringe orientation, a 32G needle, a flow rate of approximately 3 mL/min, an approximately 8 cm needle-to-bath distance, and a 100 mM $CaCl_2$ gelling bath maintained under gentle stirring at approximately 400 rpm. Following completion of extrusion, the cell-loaded alginate beads remained in the $CaCl_2$ bath for an additional 5 min before recovery. A small sample was checked under a microscope to make sure the beads held together and that cells were present inside the hydrogel before moving on to the coating step.

The alginate beads containing cells were then turned into alginate-poly-L-lysine-alginate (APA) microcapsules through a series of surface treatments. For each step, beads were allowed to settle in conical tubes for 1-2 minutes so that the liquid above could be gently removed. Fresh solutions were added gently along the tube wall to minimize mechanical disturbance, aggregation, and bead loss. The beads were first washed three times in 0.9% NaCl for 2–3 min per wash. They were then incubated for 5 min with 0.05% (w/v) poly-L-lysine (PLL; 15–30 kDa) prepared in 0.9% NaCl, followed by three additional 2–3 min washes in 0.9% NaCl.

After coating with PLL, the beads were incubated for 5 minutes in 0.10% (w/v) sodium alginate (in 0.9% NaCl), which added an outer alginate layer. Once the coating solution was removed, these APA capsules were briefly treated with 50 mM $CaCl_2$ for about 2 minutes - just enough to firm up the outer layer without causing the capsules to clump together. Capsules were then quickly rinsed in 0.9% NaCl and placed into regular growth medium. The finished APA microcapsules were checked using bright-field microscopy to confirm the shape, structure, and that the cells remained inside.

The sequential coating procedure and the resulting multilayer capsule architecture are schematically summarized in Figure 2.2. The fabrication workflow illustrates the successive washing, PLL deposition, outer-alginate coating, and final stabilization steps, while the final schematic highlights the organization of the alginate core, intermediate PLL-containing interface, and outer alginate-rich layer.

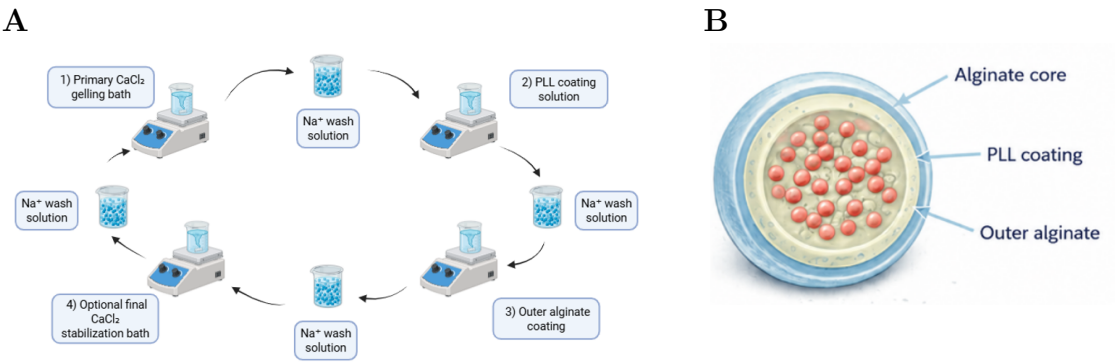


Figure 2.2: Schematic representation of APA microcapsule fabrication and final multilayer architecture. (A) Sequential coating workflow following primary $CaCl_2$ gelation, including NaCl washing, PLL deposition, additional washing, outer alginate coating, and final $CaCl_2$ stabilization. (B) Simplified representation of the resulting APA microcapsule, showing the cell-containing alginate core, the intermediate PLL-containing interface, and the external alginate-rich layer.

2.3.3 Capsule Standardization and Estimation of Cell Loading

Because APA microcapsules sediment rapidly in suspension and both capsule concentration and cellular content varied between fabrication batches, each batch was standardized before use in downstream experiments. Following fabrication, the final capsule suspension was adjusted to approximately 30 mL of complete culture medium and gently homogenized immediately before sampling. A minimum of six independent 500 μL aliquots were collected from each batch, and the number of capsules within each aliquot was determined by bright-field microscopy. The 500 μL sampling volume was selected because it corresponded to the operational suspension volume subsequently used for loading the cellular chamber of the BioHybrid device. Repeated capsule counts were used to characterize the number of capsules contained within this volume and to standardize capsule dosing across experimental conditions. When comparisons with non-encapsulated cells were performed, the batch-specific estimate of cellular content was additionally used to define the corresponding naked-cell equivalent.

The cellular content of each fabrication batch was estimated using representative cell-loaded alginate-only beads collected before PLL deposition and formation of the external alginate layer. Alginate-only beads were used because mature APA microcapsules could not be decapsulated reproducibly under the same conditions. For each analysis, the exact number of beads contained in each sampled aliquot was determined by microscopy before decapsulation. Each aliquot was processed separately in an individual well using 1 mL of a decapsulation solution containing 55 mM sodium citrate and 30 mM EDTA for approximately 5 min at room

temperature. Once the beads fully dissolved (which you could see under the microscope because the bead outlines disappeared), everything from each well was collected and combined.
Every well got an extra two or three rinses with small amounts of Ca^{2+}/Mg^{2+}-free PBS, and those rinses were also added to the main pool to get as many cells as possible. After that, the pooled mixture was spun down, the liquid on top was taken off, and the cell pellet was resuspended in a specific amount of complete culture medium for automated counting. Cell concentration and viability were both measured using trypan blue exclusion, and multiple technical counts were done when cell numbers were low to make sure the readings were reliable. For each batch, the total number of cells recovered was divided by the total number of beads used to get a per-bead estimate. The number of live cells per bead was also calculated based on overall cell recovery and cell viability measurements. These values were used as operational estimates of recoverable cellular content for normalization and dose matching in subsequent experiments. Because the procedure quantifies cells successfully recovered after chemical dissolution, the resulting value was interpreted as recovered cells per bead rather than as an absolute measurement of the true number of cells originally encapsulated within each bead. A representative bright-field image of a final cell-loaded APA microcapsule is shown in Figure 2.3, illustrating the confinement and spatial organization of the engineered cellular population within the fabricated capsule.

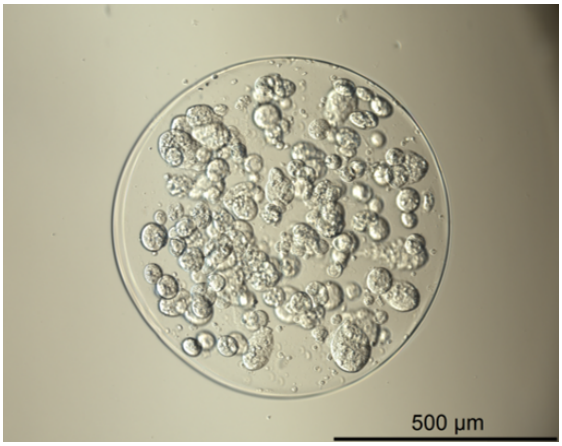


Figure 2.3: Representative bright-field image of a cell-loaded APA microcapsule following completion of the encapsulation and coating procedure. Engineered HEK293 cells are visible as confined cellular clusters distributed within the microcapsule interior. Scale bar, 500 μm. The image is shown as a representative illustration of the final cell-loaded APA configuration and was not used for quantitative morphometric analysis.

2.4 In Vitro Characterization of APA Microcapsules

2.4.1 Morphological Characterization

Morphological characterization of alginate-only beads and fully coated alginate–poly-L-lysine–alginate (APA) microcapsules was performed by bright-field microscopy using a Keyence microscope. Diameter and circularity were selected as the principal quantitative morphological parameters. Capsule diameter was considered relevant because it defines the characteristic distance between the external capsule surface and the internal regions of the hydrogel and therefore represents an important geometric parameter for subsequent transport and cell-encapsulation experiments. The fabrication process mostly produced beads between 300 and 700 μm in diameter, clustering around 500 μm.

To judge how regular the shapes were, circularity was measured alongside diameter. Having both measurements helped give a full picture of each capsule's size and how close it was to being perfectly round. On top of that, beads were also checked by eye for defects - things like clumping, breaking, misshapen capsules, uneven surfaces, or obvious irregularities.

Bright-field images were taken from typical areas for each sample, then examined with ImageJ. For the quantitative analysis, 100 individual structures from one batch of plain alginate beads and one batch of coated APA microcapsules were measured in each group. Size was reported as equivalent diameter, and circularity was based on the outline of each capsule in two dimensions.

The plain alginate beads and the final APA capsules were tested separately to see if coating with PLL and forming the extra alginate layer changed their shape. Measurements for each bead and capsule were kept to show how shapes were distributed in each group.

Other batches made using the same process looked nearly identical in terms of bead and capsule shapes when checked under bright-field microscopy, so the method seemed consistent. However, only the main batches described above were analyzed in detail. The reported diameter and circularity data come from these batches, not from separate runs.

2.4.2 Cell Viability and Intracapsular Distribution

Cell viability and spatial distribution within APA microcapsules were qualitatively evaluated using a Live/Dead fluorescence assay at Days 0, 1, 3, and 7 after encapsulation. Independent capsule samples were used at each time point to avoid repeated exposure of the same capsules to the staining procedure. Before staining, capsules were gently washed with sterile D-PBS to reduce residual serum-associated

background and transferred to fresh D-PBS containing 2 μM Calcein AM and 4 μM ethidium homodimer-1 (EthD-1). To see how regular the shapes were, both circularity and diameter were measured. Looking at both gave a better sense of each capsule's size and how close it came to being a true circle. In addition, the beads were inspected by eye for flaws - like clumping, breakage, weird shapes, rough surfaces, or other obvious defects.
Bright-field images were taken from typical spots for each sample and then checked in ImageJ. For the numbers, 100 individual structures were measured from one batch of plain alginate beads and one batch of coated APA microcapsules in each group. Size was given as an equivalent diameter, and circularity was calculated from the outline of each capsule in two dimensions.
The plain alginate beads and the finished APA capsules were analyzed separately to see if coating with PLL and adding an extra alginate layer changed their shape. Each bead and capsule's measurements were kept to show how shapes varied within each group.
Other batches produced qualitatively similar bead and capsule morphologies, under the same fabrication conditions. Still, only the main batches mentioned above were analyzed in detail. The diameter and circularity results come from these main batches, not from separate runs. Quantitative assessment of the recoverable cell population and recovered-cell viability over time was performed independently through alginate-bead decapsulation and automated cell counting, as described in Section 2.4.3.

2.4.3 Longitudinal Cell Recovery from Alginate Beads

Longitudinal recovery of encapsulated cells was evaluated using cell-loaded alginate-only beads at Days 0, 1, 3, and 7 after encapsulation. Alginate-only beads were used for this analysis because they could be reproducibly dissolved under mild chelating conditions, whereas mature APA microcapsules could not be consistently decapsulated without introducing additional variability in cell recovery. Parallel alginate-only samples were therefore retained before PLL deposition and formation of the external alginate layer.
At each time point, a minimum of six technical bead-sampling aliquots was collected, corresponding in total to at least approximately 500 beads. The exact number of beads present in each aliquot was recorded before decapsulation. Each aliquot was processed separately in an individual well using 1 mL of a solution containing 55 mM sodium citrate and 30 mM EDTA at room temperature for approximately 5 min. When complete bead dissolution was not achieved within this interval, incubation was extended to approximately 8–10 min. Following dissolution, released cells were recovered together with two to three washes performed using Ca^{2+}/Mg^{2+}-free PBS. The cell suspensions obtained from the separately processed aliquots were

subsequently pooled, centrifuged, and resuspended to generate a single recovered-cell suspension for each time point.
Cell concentration and viability were checked using an automated counter with trypan blue to identify dead cells. After gently mixing the pooled recovered cells, three separate samples were taken for counting. Each sample was counted in both chambers of the slide - so, six readings total for every time point. Mean and standard deviation were calculated from these six numbers. These measurements therefore represented technical counting variability within the same pooled recovered-cell suspension and were not treated as independent biological replicates.
The total number of recovered cells was estimated from the measured cell concentration and the final recovered suspension volume and normalized to the cumulative number of beads included in the corresponding pooled sample. Results were expressed as total recovered cells per bead, live recovered cells per bead, dead recovered cells per bead, and recovered-cell viability. Because the procedure quantified cells successfully retrieved following bead dissolution, these measurements were interpreted as the recoverable cell population per bead rather than as a direct determination of the absolute number of cells present within each bead. Temporal changes in recovered cell number were therefore used to characterize the evolution of the recoverable encapsulated-cell population over culture time and were not interpreted as a direct measurement of cellular proliferation.

2.4.4 Molecular Diffusion Characterization of APA Microcapsules

Molecular transport through APA microcapsules was characterized using fluorescent dextrans of increasing molecular weight as model solutes. Empty APA microcapsules were used to isolate transport through the capsule structure from cellular uptake, secretion, metabolism, or other biological effects. Four dextran tracers were evaluated: 3 and 10 kDa tetramethylrhodamine-labeled dextrans and 40 and 70 kDa Texas Red-labeled dextrans. To compare how different-sized molecules moved from the outside to the inside, a series of molecular weights was tested. This helped track how long it took fluorescence to reach the center of the capsules. The assay was meant to compare relative molecular movement through the APA structure, not to measure an exact permeability value or precise molecular-weight cutoff.
The experiment ran in 48-well plates, using an endpoint-transfer setup. For each tracer and time point, six independent APA microcapsules ($n = 6$) with comparable size distributions were analyzed. Capsules were dispensed in 300 μL of phenol red-free DMEM. Fluorescent dextran working solutions were freshly prepared at 0.40 mg/mL in phenol red-free DMEM, protected from light, and used on the same day. Five hundred microliters of the corresponding working solution were

added to each incubation well, resulting in a final volume of 800 μL and a final dextran concentration of 0.25 mg/mL. Timing started right after dextran was added. Fluorescence intensity in the central region of the capsules was measured at 0, 5, 10, 30, 60, and 120 minutes. For some tracers, later points at 240 and 360 minutes were checked to see how the penetration leveled off.

Direct imaging in the dextran solution wasn't used - background fluorescence from the solution made it impossible to clearly see inside the capsules. Instead, every incubation well was paired with a separate imaging well filled with PBS. At each time point, capsules were moved to the PBS well, rinsed quickly, and imaged immediately to minimize tracer redistribution during imaging. Once sampled, capsules weren't put back into the dextran, making each time point its own data point.

Both bright-field and fluorescence images were taken using a Keyence microscope with a 10× lens and the CH2/red fluorescence channel. For each tracer, fluorescence settings stayed the same across all time points to avoid saturating the images. A single optical plane was focused near the largest capsule diameter to match the equator of the capsule as closely as possible.

When it was hard to see fluorescence contrast early on, capsule shape was outlined using the corresponding bright-field image, and that outline was used for measuring fluorescence. For each capsule, a line was drawn across its diameter in the bright-field image. The midpoint marked the center, and the length gave the diameter. Matching regions were then mapped onto the fluorescence image - these included the whole capsule, a central circle, an outer edge, and an area outside the capsule for background. Mean fluorescence was recorded for each region and corrected for background with

$$I_{\text{corr}} = I_{\text{ROI}} - I_{\text{background}}.$$

Background-corrected center intensity was used as the principal quantitative measure of tracer penetration toward the capsule core, whereas whole-capsule and edge intensities were retained as complementary spatial readouts. Corrected values at $t = 0$ were set to zero to define the experimental baseline.

Because the 3 and 10 kDa tracers were conjugated to tetramethylrhodamine whereas the 40 and 70 kDa tracers were conjugated to Texas Red, absolute fluorescence amplitudes were not considered directly comparable across all four molecular-weight conditions. For cross-tracer comparison, background-corrected center fluorescence values were normalized to the corresponding plateau value measured for each tracer over its complete time course. The resulting normalized center-intensity curves therefore describe the relative progression toward the tracer-specific plateau signal observed over the measured time course and were used to compare penetration kinetics across molecular-weight conditions while minimizing differences related to fluorophore brightness and detector response.

2.5 Functional Characterization of Encapsulated Engineered HEK293 Cells

2.5.1 Basal SEAP Secretion under Adherent, Non-Adherent, and APA-Encapsulated Conditions

Before investigating stimulated secretion, basal SEAP production was evaluated to determine whether APA encapsulation altered the constitutive functional output of the engineered HEK293 cells during culture. Three cell-containing configurations were compared: adherent naked cells cultured in standard tissue-culture-treated 24-well plates, naked cells maintained in non-treated 24-well plates, and APA-encapsulated cells. The non-adherent setup was used so that cells could clump together on their own without sticking to a standard surface, giving a bare-bones 3D cell group to compare with both regular flat cultures and those trapped in the APA matrix. This made it possible to tease apart the effects caused just by cells losing grip and forming clusters versus any extra changes that come from being enclosed in the gel.

All cell-containing groups had approximately the same estimated starting cell number, around 90,000 cells per well. Adherent and non-adherent naked-cell groups were seeded directly at 90,000 cells per well. For the encapsulated condition, approximately 180 cell-loaded APA microcapsules were added per well, corresponding to approximately 90,000 cells based on the batch-specific recovered-cell-per-bead estimate obtained using the decapsulation procedure described in Section 2.3.3. The exact capsule dose was therefore adjusted according to the cellular-content estimate of the corresponding fabrication batch rather than assuming a fixed number of cells per capsule. Approximately 180 empty APA microcapsules per well were included as capsule-associated background controls, and medium-only wells served as assay blanks. Cell-containing groups were analyzed in triplicate at each endpoint ($n = 3$), whereas empty-capsule and medium-only controls were prepared in duplicate ($n = 2$). All groups were maintained in 2.5 mL of phenol red-free complete DMEM per well at 37 °C and 5% CO_2.

The experiment was performed as a destructive longitudinal time course using independent wells assigned to Day 1, Day 3, and Day 7. All wells were prepared on Day 0, and no medium replacement was performed throughout the culture period. Immediately before collection at each endpoint, representative bright-field images were acquired to document cell morphology, spontaneous aggregate formation, APA capsule integrity, and intracapsular cellular organization. The complete culture supernatant was then recovered, its volume recorded, and the sample stored at $-80\,^{\circ}\mathrm{C}$ until SEAP quantification according to Section 2.1.3. Since each measurement had its own set of wells and the culture medium was left

untouched, SEAP levels reflected the total build-up from the very beginning up to whatever time point was sampled - not just what was secreted in a short window. Total SEAP per well was found by multiplying the SEAP concentration by however much supernatant was collected:

$$M_{\mathrm{SEAP}} = C_{\mathrm{SEAP}}\, V_{\mathrm{collected}}.$$

Once SEAP was gathered, the same wells were checked for metabolic activity using the PrestoBlue (resazurin) assay. Fresh phenol red-free complete DMEM was added, and PrestoBlue reagent was used at a final concentration of 10% (v/v). Adherent and non-adherent naked cells were incubated for 2 h, whereas APA-encapsulated cells were incubated for 4 h at 37 °C and 5% CO_2, allowing additional time for transport of the assay reagent through the three-dimensional hydrogel environment. After incubation, 100 μL of assay medium from each well were transferred to a separate microplate for fluorescence measurement. Medium-only wells served as background controls for the naked-cell measurements, while empty APA microcapsules did the same for the encapsulated samples. For tracking changes over time, PrestoBlue fluorescence (after background subtraction) was normalized within each culture setup to the Day 1 value, which was always set at 100%. These final numbers reflected relative metabolic activity, not exact counts of live cells or how quickly they grew. Since the assay incubation times weren't the same for naked and APA-encapsulated cells, the normalized data was mostly used to follow changes over time within each culture setup, instead of comparing exact metabolic rates between them.

PrestoBlue was used for all experiments involving APA-encapsulated cells because its resazurin chemistry produces resorufin, a fluorescent molecule that's soluble. This makes it possible to measure metabolic activity directly in the assay medium around the microcapsules. In contrast, the MTT assay used for non-encapsulated cells in Section 2.2.2 produces insoluble formazan crystals that require a subsequent solubilization step before absorbance measurement. This makes MTT less suitable for cells confined within a three-dimensional hydrogel, where reagent penetration, intracellular crystal formation, and complete recovery of the formazan product may introduce additional variability. PrestoBlue therefore provided a more practical metabolic readout for intact APA microcapsules without requiring capsule disruption or extraction of an insoluble reaction product. The result showed how active the cells were, roughly - it's not a direct count of living cells.

The main comparisons were: regular adherent cells versus non-adherent 3D aggregates (to see what happens when cells lose their usual surface and clump together); those same non-adherent clumps versus APA-encapsulated cells (to spot any extra changes from being stuck in hydrogel); and finally, adherent cells against encapsulated ones (comparing the gel-trapped setup with the standard monolayer approach). SEAP and metabolic-activity measurements were evaluated longitudinally across

the independent Day 1, Day 3, and Day 7 endpoints.

2.5.2 Chemical Depolarization with KCl

Chemical depolarization was used to determine whether engineered HEK293 cells retained functional activation of the depolarization-sensitive Ca^{2+}/NFAT pathway after APA encapsulation and to compare the response with that of non-encapsulated cells independently of the electrical-stimulation interface. Both non-encapsulated engineered HEK293 cells and cell-loaded APA microcapsules were exposed to 60 mM KCl, which was used throughout this study as the standardized positive chemical-depolarization condition. Increasing extracellular K^+ reduces the transmembrane potassium concentration gradient and depolarizes the plasma membrane, promoting activation of the voltage-gated CaV1.2 channel and the downstream calcium-dependent NFAT pathway. KCl stimulation therefore provided an electrode-independent functional control for the responsiveness of the engineered cells in both culture configurations.

For each culture configuration, untreated and KCl-stimulated groups were prepared with six replicate wells per condition ($n = 6$). APA microcapsules were obtained from the same fabrication batch and distributed between untreated and stimulated groups using matched capsule doses based on the batch-standardization procedure described in Section 2.3.3. All groups were maintained in a final volume of 2 mL of phenol red-free complete DMEM per well. On Day 0, untreated groups received fresh phenol red-free complete DMEM, whereas stimulated groups received the same medium supplemented with KCl to a final concentration of 60 mM. In the APA groups, capsules were given about 1-2 minutes to settle before changing the medium to avoid losing any capsules. The medium containing KCl stayed with the cells the whole time until the 72-hour endpoint - there was no full medium change during this period. So, instead of a single KCl pulse, the experiment involved steady chemical depolarization.

Supernatant samples of 100 μL per well were taken at 24 hours (Day 1) and again at 72 hours (Day 3). These samples were stored at $-80\,^{\circ}$C until SEAP was measured later, as described in Section 2.1.3. The medium wasn't changed after the Day 1 collection, so the cells stayed under constant KCl exposure until Day 3. Since part of the medium was taken out at Day 1, the total SEAP produced by the endpoint had to factor in what was removed earlier. With an initial volume V_0, a Day 1 sample size of s_{24}, and measured SEAP concentrations C_{24} and C_{72}, the total SEAP was figured out like this:

$$M_{24} = C_{24}V_0$$

and

$$M_{72} = C_{24}s_{24} + C_{72}(V_0 - s_{24}).$$

To compare setups, SEAP made in response to KCl was shown as a fold-change against the untreated controls for each culture type.
After the last SEAP sample at 72 hours, all six wells per condition went through PrestoBlue analysis. PrestoBlue was added at 10% of the sample volume. Non-encapsulated cells incubated for 2 hours. APA-encapsulated cells needed 4 hours at 37°C with 5% CO_2, since the hydrogel made diffusion take longer. After incubation, 100 μL of assay medium from each well were transferred to a separate microplate for fluorescence measurement. Appropriate medium-only and empty-APA controls were used for background correction of the corresponding non-encapsulated and encapsulated conditions. Metabolic activity was expressed relative to the corresponding untreated group, defined as 100%. PrestoBlue measurements were interpreted as relative metabolic activity rather than as a direct measurement of cell viability or cell number.

2.5.3 Electrical Stimulation of APA-Encapsulated Cells

The electrical responsiveness of APA-encapsulated engineered HEK293 cells was initially explored using the C-Dish/C-PACE platform described in Section 2.2.1. Because encapsulation introduced a three-dimensional hydrogel environment and altered the spatial relationship between the cells, conductive medium, and stimulating electrodes, stimulation parameters established for non-encapsulated cells were not assumed to be directly transferable. A series of exploratory experiments was therefore performed using both 6-well and 24-well C-Dish configurations. Across successive trials, stimulation amplitude, duration, medium volume, well geometry, and stimulation schedule were varied empirically. Conditions included approximately 2.5–20 V, stimulation periods ranging from 30 min to 24 h, and medium volumes between approximately 0.5 and 5 mL, while biphasic stimulation was maintained using approximately 2 ms per phase at approximately 9–10 Hz. These experiments were treated as an exploratory screening phase rather than as a formal multivariable optimization because several parameters changed between successive experimental runs. The screening phase was used to identify stimulation amplitudes and exposure durations capable of producing measurable SEAP responses while retaining sufficient cellular metabolic activity, thereby defining an empirical starting range for subsequent experiments with the custom platinum-mesh electrode configuration. Because things like electrode shape, the amount of medium, and how current flowed were different between the C-Dish and custom setups, the exploratory experiments were mainly used to help choose parameters rather than copied exactly.
After that, a new experiment used a custom electrode setup designed to match the BioHybrid cellular compartment's shape more closely. APA microcapsules with cells were placed between a top and bottom platinum mesh electrode, and

both electrodes were hooked up to the external stimulation source using platinum wires. This configuration allowed the encapsulated cellular population to remain confined between opposing platinum surfaces rather than being stimulated by the wider-spaced C-Dish geometry. The custom arrangement therefore served as a device-relevant in vitro stimulation model rather than as a direct reproduction of the electrical conditions generated by the C-Dish. The experimental configuration is shown schematically in Figure 2.4.

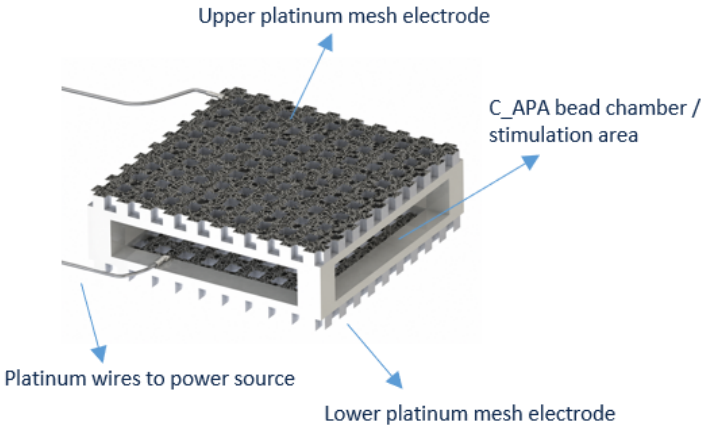


Figure 2.4: Custom platinum-mesh electrode configuration used for electrical stimulation of APA-encapsulated engineered HEK293 cells. APA microcapsules were positioned within the stimulation region between opposing upper and lower platinum-mesh electrodes connected to the external stimulation source through platinum wires. The configuration was designed to approximate the interelectrode geometry of the BioHybrid cellular compartment while allowing controlled in vitro stimulation of the encapsulated cellular population.

Cell-loaded APA microcapsules from the same fabrication batch were distributed among four stimulated groups receiving 2.5, 5, 10, or 20 V. Electrical stimulation was applied for 4 h using the biphasic waveform previously established for the electrogenetic platform. An unstimulated electrode-control group was included in which the complete electrode assembly remained in contact with the culture medium under otherwise equivalent conditions but no voltage was applied. Cell-free blank wells were additionally included for background correction. Each condition was performed in triplicate ($n = 3$), resulting in six experimental groups and 18 wells in total. Capsule dosing was standardized using the batch-specific capsule concentration and recovered-cell-per-bead estimate described in Section 2.3.3, allowing comparable estimated cellular inputs to be used across stimulation groups. Culture supernatants were collected at Day 1 and Day 3 and analyzed for SEAP using the chemiluminescent assay described in Section 2.1.3. SEAP output from the electrically stimulated groups was evaluated both as the measured signal and after normalization to the corresponding unstimulated electrode-control condition.

Voltage-dependent activation was therefore expressed as fold change relative to the unstimulated group, which was assigned a reference value of 1. This normalization was used to distinguish stimulation-associated changes from basal secretion and from effects associated with exposure to the electrode assembly itself.
At the final endpoint, cellular metabolic activity was evaluated using the 10% (v/v) PrestoBlue assay described in Section 2.5.1. Fluorescence values were first corrected using the corresponding cell-free background and were subsequently normalized to the unstimulated electrode-control group, which was defined as 100% relative metabolic activity. This approach allowed voltage-dependent changes in SEAP production to be considered together with the metabolic status of the encapsulated cellular population following electrical stimulation.

2.6 In Vitro Immunocompatibility and Immunoresistance Assessment

2.6.1 Preliminary RAW 264.7 Macrophage Co-Culture

A preliminary in vitro immunocompatibility assay was performed using RAW 264.7 murine macrophages to evaluate the early innate inflammatory response associated with the APA encapsulation system. This assay served as an initial screening model before progression to the more complex primary rat splenocyte challenge. The experimental design was intended to compare macrophage responses in the presence of empty APA microcapsules and cell-loaded APA microcapsules, using RAW 264.7 cells cultured alone as the basal macrophage reference and LPS-stimulated RAW 264.7 cells as the positive inflammatory control.
RAW 264.7 macrophages were seeded in 48-well plates at approximately 1×10^5 cells per well and allowed to adhere overnight before initiation of the immune challenge. Five experimental conditions were established: cell-loaded APA microcapsules without macrophages, RAW 264.7 cells cultured alone, RAW 264.7 cells co-cultured with cell-loaded APA microcapsules, RAW 264.7 cells co-cultured with empty APA microcapsules, and RAW 264.7 cells stimulated with lipopolysaccharide (LPS) as a positive inflammatory control. LPS was used at a final concentration of 100 ng/mL. Each condition was performed in triplicate ($n = 3$). Capsule doses were standardized according to the corresponding fabrication batch using the bead-counting and recovered-cell-per-bead procedures described in Section 2.3.3. All groups were maintained in phenol red-free complete DMEM under standard culture conditions.
For macrophage-containing groups, RAW 264.7 cells were plated on the day preceding the immune challenge. On Day 0, the corresponding cell-loaded or empty APA microcapsules were introduced into the pre-established macrophage cultures.

Cell-loaded APA microcapsules maintained without macrophages provided a reference condition for the encapsulated cellular system in the absence of immune challenge, whereas RAW-only cultures represented the basal macrophage condition. LPS-treated RAW 264.7 cells were used to check if the macrophage model could trigger an inflammatory response in these experimental conditions.
Supernatant samples were collected at 0, 6, 24, and 72 hours after starting the coculture. The sample taken at 0 hours set the baseline, right after the experiment began. Samples collected later made it possible to track how TNF-α release changed over time. After each sample was drawn, the same amount of fresh culture medium was added back to keep the working volume steady. All samples were frozen until they were tested for TNF-α and, if relevant, SEAP.
To measure macrophage activation, mouse TNF-α levels in the culture supernatants were quantified using the Invitrogen Mouse TNF alpha ELISA Kit (BMS607-3). Every sample, standard, and blank was run in technical duplicate. The supplied mouse TNF-α standard was reconstituted to 2 ng/mL and serially diluted 1:2 to generate a seven-point calibration curve: 2000, 1000, 500, 250, 125, 62.5, and 31.3 pg/mL Sample Diluent served as the blank. Before adding anything, the antibody-coated microwell strips were washed twice with about 400 μL of Wash Buffer for each well.
For readings from the culture supernatant, 50 μL of Sample Diluent and 50 μL of either sample or standard were added per well, then 50 μL of biotin-conjugated anti-mouse TNF-α antibody (diluted 1:200 for these samples) was added on top. Plates were incubated for 2 h at room temperature on a microplate shaker and subsequently washed six times. One hundred microliters of Streptavidin-HRP diluted 1:100 were then added and incubated for 1 h at room temperature with shaking, followed by six additional washes. Color development was initiated by addition of 100 μL of TMB substrate and allowed to proceed for approximately 30 min at room temperature. The reaction was terminated by addition of 100 μL of Stop Solution, and absorbance was measured at 450 nm, with 620 nm used as a reference wavelength when applicable. TNF-α concentrations were calculated from the corresponding standard curve. The manufacturer reports an analytical sensitivity of 3.7 pg/mL, while the lowest concentration included in the experimental standard curve was 31.3 pg/mL.

2.6.2 Primary Rat Splenocyte Challenge and Immune Activation Profiling

A second-stage immunoresistance assay was performed using freshly isolated primary rat splenocytes to evaluate the interaction between APA-encapsulated engineered HEK293 cells and a heterogeneous immune-cell population. Compared with the preliminary RAW 264.7 assay, this experiment incorporated soluble inflammatory

readouts, flow-cytometric T-cell phenotyping, and acquisition of CFSE fluorescence as an intended proliferation readout, while simultaneously monitoring SEAP secretion from the engineered-cell payload.

Rat splenocytes were isolated from freshly collected spleens by mechanical dissociation through a sterile 40 μm cell strainer positioned over a 50 mL collection tube. The spleen was gently pressed through the strainer using the flat end of a sterile syringe plunger while being rinsed with cold RPMI 1640. The resulting suspension was centrifuged at 400 $\times g$ for 5 min at 4 °C. Red blood cells were lysed by resuspending the pellet in 2 mL of ACK lysis buffer and incubating for 2–5 min at room temperature with gentle agitation. Lysis was quenched with 4 mL of complete RPMI or azide-free buffer, followed by centrifugation at 400 $\times g$ for 5 min at 4 °C. The pellet was resuspended and passed through a new 40 μm strainer to clear out any leftover tissue clumps before measuring total cell count and viability. Splenocytes were kept in RPMI 1640 with 10% fetal bovine serum, 1% penicillin-streptomycin, L-glutamine, 25 mM HEPES, and 50 μM β-mercaptoethanol. Before plating, the cells were labeled using CellTrace CFSE as described by the manufacturer, then thoroughly washed to remove any excess dye and resuspended in complete RPMI. CFSE-labeled splenocytes were seeded at 0.5×10^6 cells per well in 48-well plates at a final working volume of 1.0 mL per well and maintained overnight before initiation of the immune challenge. CFSE fluorescence was subsequently acquired as an intended readout of splenocyte proliferation.

Eight experimental conditions were established to distinguish the effects associated with the APA material, the encapsulated engineered-cell payload, direct exposure of naked engineered cells to the immune population, and defined positive immune stimuli: cell-loaded APA microcapsules without splenocytes, cell-loaded APA microcapsules with splenocytes, empty APA microcapsules with splenocytes, naked engineered HEK293 cells without splenocytes, naked engineered HEK293 cells with splenocytes, splenocytes alone, LPS-stimulated splenocytes, and PHA-stimulated splenocytes. Cell-loaded APA without splenocytes, cell-loaded APA with splenocytes, naked engineered HEK293 cells without splenocytes, and naked engineered HEK293 cells with splenocytes were prepared in six replicate wells per condition ($n = 6$). Empty APA with splenocytes, splenocytes alone, LPS-stimulated splenocytes, and PHA-stimulated splenocytes were prepared in triplicate ($n = 3$). LPS was added at a final concentration of 1 μg/mL as a positive control for inflammatory cytokine production, whereas PHA was added at 5 μg/mL as a positive control for T-cell activation and proliferation. The complete experimental design is summarized in Table 2.1.

Table 2.1: Experimental groups used for the primary rat splenocyte challenge. Cell-loaded APA microcapsules and naked engineered HEK293 cells were evaluated either alone or in the presence of primary rat splenocytes. LPS and PHA were included as positive controls for inflammatory cytokine production and T-cell activation/proliferation, respectively.

Group	**Experimental condition**	**Splenocytes**	**Stimulus**	n
G1	Cell-loaded APA microcapsules	No	–	6
G2	Cell-loaded APA microcapsules + splenocytes	Yes	–	6
G3	Empty APA microcapsules + splenocytes	Yes	–	3
G4	Naked engineered HEK293 cells	No	–	6
G5	Naked engineered HEK293 cells + splenocytes	Yes	–	6
G6	Splenocytes only	Yes	–	3
G7	Splenocytes + LPS	Yes	1 μg/mL LPS	3
G8	Splenocytes + PHA	Yes	5 μg/mL PHA	3

A splenocyte-to-engineered-cell ratio of approximately 10:1 was targeted, using the estimated engineered-cell input for the encapsulated conditions. With 0.5×10^6 splenocytes per well, naked engineered HEK293 cells were therefore introduced at 0.5×10^5 cells per well. For the encapsulated groups, the number of APA microcapsules required to provide an equivalent estimated engineered-cell dose was calculated from the batch-specific recovered-cell-per-bead value described in Section 2.3.3. Cell-loaded and empty APA microcapsules were resuspended in complete RPMI before addition to the experimental wells, and all conditions were adjusted to a final volume of 1.0 mL per well.

Culture supernatants were collected after 24 and 72 h. Before each collection, APA microcapsules were allowed to sediment briefly and 400 μL of supernatant were carefully withdrawn from the upper portion of each well to minimize capsule carryover. Samples were clarified by brief centrifugation, after which 350 μL of cleared supernatant were recovered while approximately 50 μL were retained with the pellet-containing fraction. For groups containing engineered HEK293 cells, 100 μL of cleared supernatant were allocated to SEAP analysis and 250 μL to cytokine measurements. For conditions without engineered HEK293 cells, the complete 350 μL cleared fraction was allocated to cytokine analysis. At the 24-h time point, the residual 50 μL pellet-containing fraction was gently resuspended and returned to the original well, after which 350 μL of fresh complete RPMI were added to restore the working volume. At 72 h, samples were collected using the same procedure without subsequent medium replacement. All collected samples were stored at $-80\,^{\circ}\mathrm{C}$ until analysis. Consequently, the 24-h samples represented accumulation during the initial 0–24-h interval, whereas the 72-h samples contained contributions from both analyte remaining after the partial medium replacement and additional production during the subsequent 24–72-h period and were therefore not interpreted as isolated 24–72-h secretion measurements.

SEAP secretion from groups containing engineered HEK293 cells was quantified using the chemiluminescent assay described in Section 2.1.3. Inflammatory cytokine production was evaluated by quantification of rat TNF-α and IL-6 in the corresponding culture supernatants.

Rat TNF-α was quantified using the Invitrogen Rat TNF-α ELISA Kit (KRC3011). Culture supernatants were diluted 1:2 in Standard Diluent Buffer before analysis, and standards and samples were processed according to the manufacturer's assay procedure. Standards and samples were added to plates at 100 μL per well and left for 2 hours at room temperature. After, the wells were washed four times and treated with 100 μL of biotin-tagged anti-rat TNF-α antibody for 1 hour. Four more washes came next, followed by 100 L of Streptavidin-HRP for 30 minutes. After another four washes, 100 μL of TMB substrate was added, then left in the dark for 30 minutes at room temperature. The reaction was stopped by adding 100 μL of Stop Solution, and absorbance was checked at 450 nm.

Cytokine levels were worked out using the matching standard curve and adjusted for how much the samples were initially diluted. Measurements below 31.3 pg/mL (the lower limit of the standard curve for the assay, set by the conditions used here) were considered too low to be reliably measured.

Rat IL-6 was quantified using the Invitrogen Rat IL-6 ELISA Kit (BMS625). Samples, standards, and blanks were analyzed in technical duplicate. A seven-point standard curve ranging from 31.3 to 2000 pg/mL was prepared by two-fold serial dilution. Fifty microliters of Assay Buffer and 50 μL of culture supernatant were added to each sample well, followed by 50 μL of diluted biotin-conjugated anti-rat IL-6 antibody. Plates were incubated for 2 h at room temperature and subsequently washed six times. Then, 100 μL of diluted Streptavidin-HRP was added and set at room temperature for 1 hour, followed by six washes. The color reaction began when 100 μL of TMB substrate was added for about 10 minutes, then stopped with 100 μL of Stop Solution. Absorbance was measured at 450 nm, with 620 nm used for background correction if needed. Concentrations were adjusted for the 1:2 sample dilution. According to the manufacturer, the lowest detectable limit is 12 pg/mL.

After 72 hours, each co-culture well was gently resuspended and filtered through a 70 μm strainer to separate APA microcapsules from the splenocyte suspension. Splenocytes from the flow-through were spun down, washed with serum-free PBS or D-PBS, and stained using LIVE/DEAD Fixable Blue in a protein-free buffer. After another wash, the cells were resuspended in FACS buffer and blocked with rat Fc block, then stained with the surface-antibody mix: CD45-BUV737, CD3-PE, CD4-BV421, CD8a-Alexa Fluor 647, CD25-BV711, and CD44-RB705. After staining, the cells were washed, resuspended in FACS buffer, kept at 4°C in the dark, and run on a Cytek Aurora spectral flow cytometer.

Flow cytometry included gating out debris and doublets, identifying viable $CD45^+$ leukocytes, and then gating for $CD3^+$ T cells. $CD4^+$ and $CD8a^+$ T cells were then analyzed separately. CD25 and CD44 expression were used as activation-associated markers, whereas CFSE fluorescence profiles were acquired to evaluate potential dilution associated with cellular proliferation. Fluorescence-minus-one controls were used to support the definition of marker-specific gating thresholds.

2.7 BioHybrid Device Adaptation and APA Integration

2.7.1 Previous Cellular-Chamber Configuration and Design Constraints

The BioHybrid platform investigated in this study originated from a previous implantable architecture developed for electrical stimulation of non-encapsulated engineered HEK293 cells. The cellular compartment had an approximately 13 × 13 mm footprint and contained two opposing square platinum-mesh electrodes, each with an exposed area of approximately 1 cm^2, separated by approximately 2 mm. Platinum wires connected the meshes to the adjacent electronic compartment through small passages between the cellular and electronic regions, while the battery and associated circuitry were isolated from the fluid-containing chamber by resin sealing. This configuration allowed electrical stimulation to be delivered across the cellular region while maintaining physical separation between the biological and electronic compartments.

Each platinum-mesh electrode was coated with approximately 100 μL of PEDOT-based hydrogel, corresponding to approximately 200 μL per device in this configuration. The coating had a dual intended function: to modify the electrode–electrolyte interface and support electrical charge transfer during stimulation, and to reduce the effective openings of the platinum mesh to improve confinement of freely suspended cells within the interelectrode region. Approximately 4×10^4 engineered HEK293 cells were loaded directly into the chamber as a non-encapsulated suspension, and the device was subsequently maintained undisturbed for approximately 30–60 min in an attempt to favor cellular retention and interaction with the coated electrode surfaces.

Two silicone access ports provided access to the cellular chamber and were used during loading, medium filling, sampling, removal of trapped air, and sealing. During development, two chamber configurations were used, containing approximately 0.6 mL and 1.8 mL of culture medium, respectively, while maintaining a target cellular load of approximately 4×10^4 cells per device. The external surface of the cellular compartment was covered by a polyethersulfone (PES) membrane with a nominal pore size of 0.03 μm (30 nm) and an exposed area of approximately 1.56 cm^2. The membrane served as the principal macroscopic barrier for cellular retention and separation of the internal cellular compartment from the surrounding environment.

In this architecture, freely suspended cells lacked an independent three-dimensional retaining or immunoisolating matrix. Cellular localization therefore depended largely on the chamber geometry, the PEDOT-coated electrodes, and the external

PES membrane. Stable attachment of the naked cells to the PEDOT-coated meshes was not achieved during the post-loading incubation, limiting control over their final position within the stimulation region. Moreover, the PES membrane simultaneously performed cellular-retention and host-separation functions while potentially contributing additional transport resistance between the internal chamber and its surroundings. Transport across this membrane was investigated experimentally but could not be successfully quantified as an isolated permeability parameter; consequently, its contribution to overall device transport was not determined independently.
These constraints motivated the transition to an encapsulation-based architecture in which cellular confinement and the intended immunoisolating function were transferred from the macroscopic device boundary to individual APA microcapsules. This change allowed the external chamber interface to be redesigned primarily for capsule retention and molecular exchange while preserving the opposing-electrode geometry required for electrical stimulation.

2.7.2 Redesign of the Cellular Compartment and Mesh Characterization

The transition from naked-cell loading to APA microcapsules required adaptation of the cellular compartment while preserving the opposing platinum-mesh electrodes and the interelectrode stimulation region of the previous BioHybrid architecture. Because the encapsulated cellular payload consisted of microcapsules substantially larger than individual cells, the external chamber interface could be redesigned around capsule retention rather than direct retention of freely suspended cells.
An initial design incorporated the capsule-retention structure directly into the 3D-printed cellular chamber, with nominal mesh openings of approximately 200 μm. The dimensional fidelity of this integrated retention structure was evaluated using a Keyence optical and laser profiling system. Optical images, surface height maps, and 3D reconstructions were collected from the printed mesh. Diameters of individual pores were measured from Keyence microscope images and used to plot a pore-size distribution, which was compared to the size range found for APA microcapsules. The standard 100 m opening on the chosen nylon mesh provided a size reference.
The finished printed mesh showed a lot of variation in pore size, with a spread that overlapped the lower end of the APA capsule size range. Because this geometry did not provide sufficient dimensional separation between retention openings and the encapsulated payload, the integrated printed mesh was not adopted for the final chamber configuration. Instead, the retention element was implemented as a separate nylon mesh with nominal openings of approximately 100 μm.
The nylon mesh was positioned across the external cellular-chamber interface and

was selected primarily to provide mechanical retention of intact APA microcapsules while maintaining a substantially more open macroscopic interface than the 30-nm PES membrane used in the previous naked-cell device. The nylon mesh was not intended to provide immunoisolation. Instead, the APA capsule surrounding each engineered-cell population was intended to provide the principal immunoisolating interface, whereas the external mesh maintained the microcapsules within the device and permitted fluid and molecular exchange through the chamber boundary. Consequently, host cells would not be physically excluded by the nylon mesh itself and could approach the external surfaces of the retained APA microcapsules.

APA encapsulation also removed the cell-retention function previously assigned to the PEDOT coating on the platinum-mesh electrodes. Because individual engineered cells were now confined within microcapsules and capsule retention was provided by the redesigned chamber interface, reduction of the electrode openings by a hydrogel coating was no longer required for payload retention. The opposing platinum-mesh electrodes were therefore retained without PEDOT in the redesigned cellular compartment. Although PEDOT can provide favorable electrode-interface properties, its removal simplified the chamber architecture and avoided retaining a material that was no longer necessary for mechanical cell confinement. The electrical consequences of this modification were not assumed to be negligible and required separate evaluation under the redesigned stimulation conditions.

The access interface was simplified concurrently from two silicone ports to a single self-sealing loading port. APA microcapsules were introduced through this port directly into the space between the opposing electrodes. A dedicated second venting port was no longer incorporated because the permeable nylon mesh provided a pathway for displacement of medium during capsule loading. The resulting APA-compatible BioHybrid architecture is schematically illustrated in Figure 2.5, highlighting the spatial relationship between the cellular chamber, retention mesh, platinum-mesh electrode assembly, loading port, and electronic compartment.

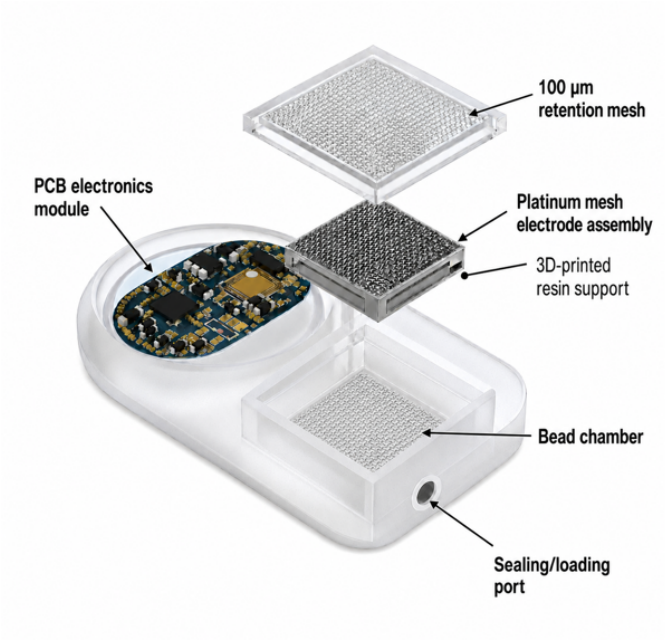


Figure 2.5: Exploded view of the redesigned APA-compatible BioHybrid device. The cellular compartment features a nominal 100 m retention mesh, a platinum-mesh electrode assembly, a 3D-printed frame, and a chamber dedicated to APA microcapsules. There's also a self-sealing silicone port for loading capsules and taking samples, and right next to it, an electronics compartment holds the PCB and stimulation hardware. In the redesigned architecture, the external mesh primarily provides mechanical retention of the APA microcapsules, whereas the capsules themselves are intended to provide the principal immunoisolating interface for the engineered cellular payload.

2.7.3 Device Assembly, Sterilization, and Preconditioning

Before assembly, the 3D-printed BioHybrid device body underwent a post-processing and cleaning procedure to remove residual material from fabrication and prepare the structure for biological use. Printed bodies were initially cleaned with isopropanol and subsequently treated with an Alconox-based laboratory detergent for approximately 10 min. The components were then extensively rinsed with deionized water for approximately 30 min to remove residual detergent, dried, and sterilized by autoclaving. Autoclaving was performed at this stage on the cleaned 3D-printed device body before integration of the nylon mesh and silicone components.
The approximately 100 μm nylon retention mesh was cut to the geometry required to cover the cellular-chamber opening using a laser cutter. Mesh pieces were rinsed with Alconox and deionized water, then dried before being put together. The nylon mesh was fixed around the chamber interface using NuSil MED3-4220 silicone adhesive, which was applied along the mesh edge, making sure the center stayed open. The mesh was pressed flat against the chamber for a tight seal around its edge, and the silicone adhesive was cured at 60°C overnight.
A self-sealing loading port was made with NuSil MED3-4213 silicone. This let a needle access the cell chamber directly while keeping it closed otherwise. Once cured, the silicone could be punctured to load APA capsules and would reseal when the needle was pulled out. This meant capsules could be loaded through just one port without leaving a permanent opening in the device wall.
Because the nylon mesh and silicone components were incorporated after autoclaving of the printed body, the completed device underwent a final chemical sterilization step immediately before biological loading. Fully assembled devices were completely immersed in 70% ethanol and subsequently subjected to three sequential immersion washes in sterile PBS to remove residual ethanol. After the final PBS wash, devices were completely immersed in complete culture medium to precondition the cellular compartment and permeable interfaces before introduction of APA microcapsules. Immediately before loading, each device was completely filled with culture medium and subjected to vacuum degassing to minimize trapped air within the cellular chamber and permeable interfaces. Devices were then visually inspected to confirm complete wetting and the absence of obvious residual air bubbles before APA microcapsule injection.

2.7.4 APA Microcapsule Loading into the Redesigned Device

APA loading into the redesigned BioHybrid device was performed according to the experimentally determined capsule concentration of each fabrication batch. Before loading the devices, the final APA suspension was gently mixed, since the

microcapsules tended to settle quickly. To figure out the capsule concentration, repeated samples of a known volume were taken. The amount of suspension needed for the target bead dose was then calculated based on the average capsule count.
In the in vitro feasibility test, devices were paired mainly by the number of APA microcapsules added to each chamber - not by an exact cell count inside those capsules. This experiment was designed to assess practical capsule loading and retention and to determine whether secreted SEAP could be detected outside the redesigned device; it was therefore not intended to reproduce precisely the approximately 4×10^4-cell payload used in the previous naked-cell configuration.
Immediately before loading, the APA suspension was gently resuspended to redistribute sedimented microcapsules. The suspension was aspirated into a syringe equipped with a 19G needle, and the self-sealing silicone port was punctured. Microcapsules were added slowly to the chamber to keep turbulence, capsule breakage, and air bubbles to a minimum. As the capsules came in, the culture medium could exit through a nylon mesh (about 100 m), which let the chamber fill up - no extra vent port needed.
Once the capsule suspension was in, the needle was pulled out and the silicone port closed back up on its own. The chamber was then checked visually to confirm that APA microcapsules were present and spread out between the electrodes, and to spot any obvious leaks, areas where capsules were piling up, or trapped bubbles.

2.7.5 Short-Term In Vitro Assessment of SEAP Release from the Mesh-Based Device

A short-term in vitro proof-of-concept experiment was performed to determine whether APA-encapsulated engineered HEK293 cells could be functionally maintained within the redesigned BioHybrid device and whether molecular exchange could occur between the internal cellular compartment and the surrounding external medium. Two experimental conditions were evaluated: untreated devices and devices exposed externally to 60 mM KCl as a chemical depolarization condition. Three independent devices were prepared per condition ($n = 3$).
After APA loading, each device contained approximately 700 μL of complete culture medium within the internal cellular compartment and was kept fully immersed in 5 mL of external culture medium within an individual well. In the untreated condition, both compartments contained standard culture medium. In the KCl condition, KCl was added exclusively to the 5 mL external medium to a final concentration of 60 mM; no KCl was added directly to the internal 700 μL device compartment. This configuration was used to determine whether an externally applied ionic stimulus could reach the encapsulated cellular population through the redesigned mesh-based interface and subsequently induce the depolarization-responsive SEAP pathway.

SEAP samples were collected independently from the internal cellular compartment and from the external surrounding medium at Day 1 and Day 3. The Day 3 endpoint provided a complete paired inside–outside dataset for all devices and was therefore used as the principal quantitative comparison. The experiment was terminated after Day 3 because its objective was to provide an initial device-level feasibility assessment of molecular exchange and stimulated reporter release rather than to evaluate long-term device performance. Sustained exposure to 60 mM KCl was additionally considered unsuitable as a prolonged culture condition because the chemical-depolarization experiments described in Section 2.5.2 demonstrated a substantial reduction in cellular metabolic activity following extended exposure.
SEAP concentration was quantified using the chemiluminescent assay described in Section 2.1.3. To account for the different volumes of the internal and external compartments, measured concentrations were converted to total SEAP amount by multiplying the measured concentration by the corresponding compartment volume, using 0.7 mL for the internal cellular compartment and 5.0 mL for the external well compartment. The resulting amount was subsequently normalized to the number of APA microcapsules loaded into the corresponding device and expressed as SEAP amount per loaded APA bead (ng/bead).
Normalization by capsules number was used to account for device-to-device variability in the number of microcapsules introduced during loading. The experiment focused on how well molecules could move in both directions in the new setup: for inward access, they looked at how cells responded when KCl was added only to the outside compartment. For outward movement, they checked how much cell-released SEAP showed up in the surrounding medium. These measurements were not used to calculate absolute permeability coefficients, diffusion coefficients, or membrane transport rates.

2.8 Data Processing and Statistical Analysis

Quantitative data were processed and plotted using GraphPad Prism (GraphPad Software, Boston, MA, USA). Data presentation depended on the experimental design and included individual measurements, means, standard deviations, fold changes, normalized values, and concentration values derived from calibration curves where appropriate. The number and nature of experimental replicates used for each assay are reported in the corresponding methodological subsection and figure legend. Technical replicate measurements originating from the same experimental sample were averaged, pooled, or otherwise treated according to the specific experimental design and were not considered independent biological replicates.

SEAP calibration data were analyzed separately for each detector gain and concentration range as described in Section 2.1.3. Blank-corrected standard signals were fitted by linear regression, and the corresponding slope, intercept, and coefficient of determination (R^2) were obtained. Experimental SEAP data were analyzed as calculated concentration, cumulative amount, normalized output, or fold change depending on the specific experiment. Electrical-stimulation responses were normalized to the corresponding unstimulated electrode-control condition, whereas KCl-induced responses were compared with the corresponding untreated condition. For morphological characterization, quantitative equivalent-diameter and circularity analyses were performed on 100 individual structures from one representative alginate-only batch and one representative APA batch generated after optimization of the fabrication parameters. Individual bead and capsule measurements were displayed using violin plots to visualize the corresponding object-level distributions. Additional fabrication batches produced using the same standardized parameters were evaluated qualitatively by bright-field microscopy to assess whether overall bead and capsule morphology remained comparable with the representative analyzed batches. Some extra batches were made, but these weren't included in the main quantitative shape analysis. So, any stats comparing capsule diameter and circularity only show differences within those two main batches - not across totally separate batches.

Cell counts after recovery were adjusted based on the exact total number of beads processed, and expressed as total, live, or dead cells per bead, as needed. For the long-term recovery experiment, cell measurements taken repeatedly from the same pooled suspension were considered technical repeats, not independent biological samples. PrestoBlue fluorescence was corrected using the corresponding medium-only, cell-free, or empty-capsule background and subsequently normalized to the appropriate experimental reference condition. PrestoBlue-derived measurements were interpreted as relative metabolic activity rather than as direct measurements of cell viability, viable-cell number, or proliferation.

ELISA-derived TNF-α and IL-6 concentrations were calculated from the corresponding calibration curves and corrected for sample dilution where applicable. Flow-cytometry datasets were processed according to the gating strategy described in Section 2.6.2. Frequencies of live cells and activation-associated T-cell populations were reported descriptively. CFSE fluorescence was acquired as an intended proliferation readout; however, because the resulting profiles did not provide a clearly resolved dilution pattern or adequate positive-control separation, no quantitative CFSE-based proliferation endpoint was derived.

For the dextran-transport experiments, background fluorescence from outside the capsules was subtracted out. The main number used to measure tracer movement was the fluorescence at the center; normalized intensity curves from the center were then compared to see how tracers moved at different rates. Different dyes were

used for the low- and high-weight dextrans, so absolute brightness wasn't compared between all the conditions.
For the device-level release experiment, SEAP concentration was converted to total compartment amount using the corresponding internal or external medium volume and was subsequently normalized to the number of APA microcapsules loaded into each device. These values were used as functional measures of reporter recovery from the internal and external compartments and were not used to derive absolute membrane permeability or transport coefficients.
Statistical inference was limited to comparisons for which a formal statistical test was considered appropriate. The specific statistical test used for each dataset, together with the corresponding sample size and replicate definition, is reported in the relevant figure legend. A value of $p < 0.05$ was considered statistically significant.

Chapter 3

Results and Discussion

3.1 Preliminary Analytical and Electrical Characterization

Before evaluating the biological response of the engineered cells and the subsequent APA-based platform, the analytical and electrical systems used throughout the experimental work were characterized. This preliminary phase included calibration of the chemiluminescent SEAP assay across different detector-gain settings and characterization of the electrical output generated by the C-Dish/C-PACE stimulation platform. These measurements established the analytical and physical reference conditions used for interpretation of the subsequent cellular experiments.

3.1.1 SEAP Calibration and Detector-Gain Selection

The chemiluminescent SEAP assay was characterized across multiple detector-gain settings to identify an acquisition condition suitable for subsequent comparison of experimental samples. Separate calibration curves were generated for the low concentration range (0.03125–1 ng/mL) and the high concentration range (0.3125–10 ng/mL). Across the investigated gains, SEAP concentration and blank-corrected chemiluminescence showed a strong approximately linear relationship within both calibration ranges, while the magnitude of the detected signal increased markedly with increasing detector gain.
Gain 125 was selected as the fixed working condition for subsequent cross-experiment comparisons. At this setting, the low-range calibration was described by

$$RLU_{\mathrm{net}} = 204.8C - 2.656,$$

with $R^2 = 0.9897$, whereas the high-range calibration followed

$$RLU_{\mathrm{net}} = 191.5C + 3.846,$$

with $R^2 = 0.9985$, where C represents SEAP concentration in ng/mL. The corresponding calibration curves are shown in Figure 3.1. The comparable slopes obtained from the independently prepared low- and high-range calibration series were consistent with a similar concentration-dependent assay response across their overlapping concentration region.

As the detector gain went up, so did the signal amplification - which showed up as steeper slopes on the calibration curves. At low gain settings like 100 or 110, the change in measured RLU for each unit of SEAP concentration was small, so signals from samples with low reporter levels stayed weak. On the other hand, when the gain was set above 125, the calibration curves got much steeper. That meant a little bump in SEAP concentration caused a much larger change in signal, but it also meant that high-output samples ran into limited headroom pretty quickly.

In the end, gain 125 struck a reasonable balance. It was sensitive enough to pick up weaker signals, but still left enough measuring room when SEAP secretion was high. This was especially important because the later experiments covered a wide range of sample types - from cells with just baseline secretion and those left alone, to others that got chemical or electrical stimulation. Plus, sticking with a single, fixed gain helped keep things consistent across experiments, since using AutoGain can make results less comparable due to variable amplification. The regression

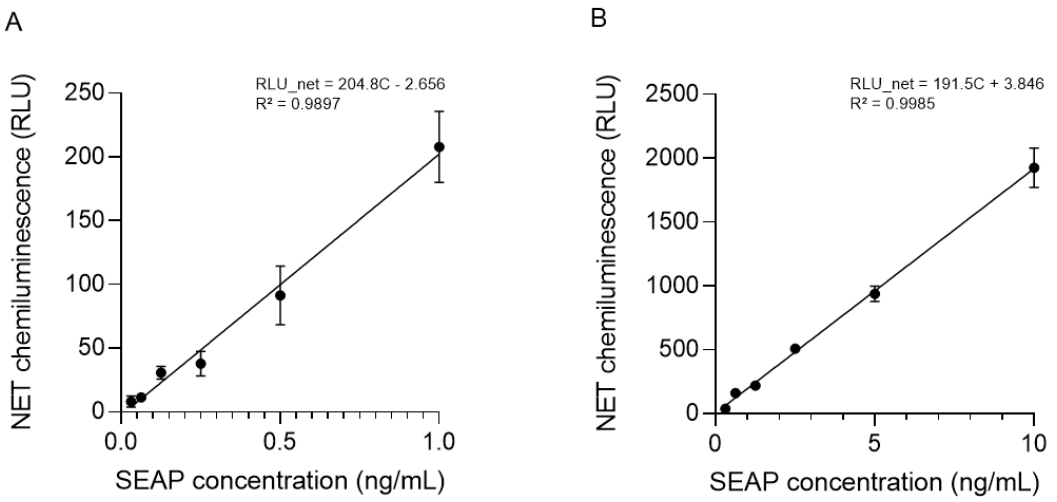


Figure 3.1: SEAP calibration curves acquired at detector gain 125. (A) Low-range calibration from 0.03125 to 1 ng/mL. (B) High-range calibration from 0.3125 to 10 ng/mL. Data points represent mean ± SD of triplicate measurements after subtraction of the corresponding matrix-blank signal. Solid lines indicate linear regression fits. The corresponding regression equations and coefficients of determination (R^2) are reported within each panel.

parameters obtained across the complete detector-gain series are summarized in

Table 3.1. Several higher-gain conditions displayed coefficients of determination comparable to or slightly greater than those obtained at gain 125. The working gain was therefore not selected solely on the basis of R^2, but according to the combined requirements of linear response, sufficient signal amplification at low SEAP concentrations, and maintenance of an appropriate measurement range for subsequent biological experiments.

Table 3.1: Linear-regression parameters obtained for the low- and high-range SEAP calibration curves at different detector gains. Concentrations for both calibration ranges are expressed in ng/mL. Gain 125, subsequently selected for cross-experiment comparisons, is highlighted in bold.

	Low range (0.03125–1 ng/mL)		High range (0.3125–10 ng/mL)	
Gain	Regression equation	R^2	Regression equation	R^2
100	$y = 58.9x - 0.8611$	0.9835	$y = 48.788x - 2.1401$	0.9983
110	$y = 66.9x - 1.9755$	0.9834	$y = 57.009x - 0.9486$	0.9974
125	$\mathbf{y = 204.8x - 2.656}$	**0.9897**	$\mathbf{y = 191.5x + 3.846}$	**0.9985**
150	$y = 1161.8x - 12.618$	0.9944	$y = 1100.7x + 22.194$	0.9992
175	$y = 2856.7x - 80.252$	0.9858	$y = 2561.3x + 93.275$	0.9987
200	$y = 6342.7x - 178.8$	0.9963	$y = 5658.1x + 138.89$	0.9988
225	$y = 23465x - 183.36$	0.9869	$y = 21817x + 838.4$	0.9981
255	$y = 71797x - 1822.3$	0.9799	$y = 64532x + 5430.4$	0.9969

3.1.2 C-Dish/C-PACE Electrical Characterization

Cell-free characterization of the C-Dish/C-PACE system showed a strong approximately linear relationship between applied voltage and measured peak current across both electrode-platform configurations and all tested medium conditions. Linear regression yielded coefficients of determination ranging from $R^2 = 0.9956$ to $R^2 = 1.000$, confirming that current delivery increased predictably over the investigated 1–32 V range. The current–voltage relationships obtained for C-Dish 95 and C-Dish 40 are shown in Figure 3.2.

The volume of conductive medium had a pronounced effect on the current delivered by the system. For C-Dish 95, the regression slopes obtained at 2 mL were 2.626 and 2.829 mA/V in PBS and DMEM, respectively, whereas at 5 mL the corresponding slopes increased to 7.415 and 6.999 mA/V. A similar pattern was observed for C-Dish 40, with slopes of 2.978 and 2.829 mA/V at 2 mL and 7.398 and 7.188 mA/V at 5 mL for PBS and DMEM, respectively. Thus, increasing the medium volume from 2 to 5 mL substantially increased the current generated at a given applied voltage in both electrode configurations. This behavior is consistent with a reduction in the effective electrical resistance of the conductive path when a larger volume of electrolyte is present between the electrodes.

In contrast, differences between PBS and DMEM were comparatively limited when the medium volume and C-Dish configuration were kept constant. The effect of solution volume was therefore substantially greater than the effect of medium composition under the conditions investigated. The two C-Dish models also displayed broadly comparable electrical behavior. This was particularly evident under the 5 mL DMEM condition subsequently used for preliminary cellular stimulation experiments. At an applied voltage of 10 V, peak current was approximately 71.1 mA for C-Dish 95 and 72.7 mA for C-Dish 40, while at 20 V the corresponding currents were approximately 140.7 and 144.7 mA, respectively.
These measurements demonstrate that applied voltage alone does not fully define the electrical conditions generated within the culture well, since the resulting current was strongly dependent on the volume of conductive medium. The close current–voltage behavior of the newer C-Dish 95 and the earlier C-Dish 40 further indicated that the overall electrical response of the stimulation platform was preserved across the two available electrode configurations. Accordingly, measured peak current under the relevant DMEM and volume conditions was used as a complementary experimental descriptor of the delivered stimulation when interpreting the subsequent cellular-response experiments.

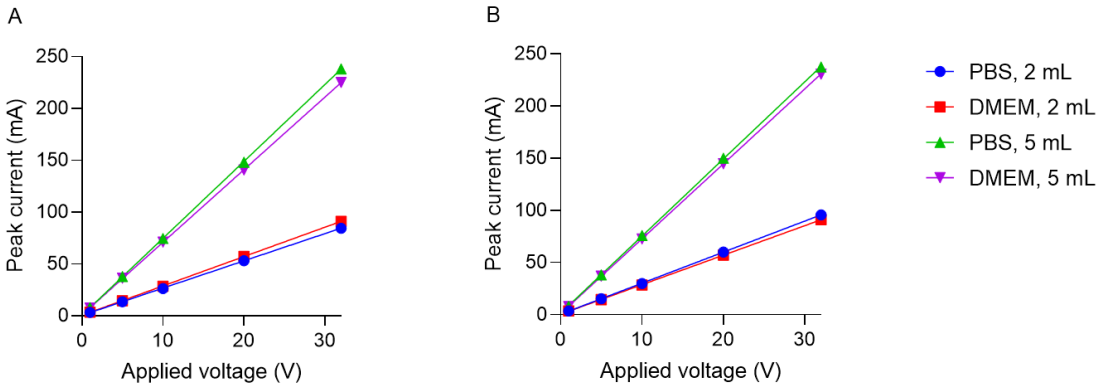


Figure 3.2: Cell-free electrical characterization of the C-Dish/C-PACE stimulation platform. Current–voltage relationships were measured for (A) C-Dish 95 and (B) C-Dish 40 using PBS or DMEM at volumes of 2 or 5 mL per well. Peak current was calculated from the voltage drop measured across a 30 Ω shunt resistor. Data are presented as mean ± SD of three replicate measurements ($n = 3$) for each condition, and solid lines indicate linear regression fits. Applied voltage and measured peak current showed a strongly linear relationship under all tested conditions ($R^2 = 0.9956$–1.000).

3.1.3 Preliminary Electrical Stimulation of Non-Encapsulated HEK293 Cells

Following characterization of the C-Dish/C-PACE platform, the electrical responsiveness of non-encapsulated engineered HEK293 cells was investigated through a series of exploratory voltage–duration experiments.We tested voltages of 2, 7.5, 10, 20, and 40 V, running each for either 1, 4, 8, or 24 hours. Since these voltage tests happened one after another during early protocol tweaking instead of in a fully balanced design, each series was compared to its own unstimulated-electrode (US) control, set at 100%. So, instead of careful cross-voltage stats, we looked at trends - mainly how cells responded based on both voltage and how long they were stimulated.

At the 24-hour SEAP readout, response patterns clearly depended on both the voltage used and the length of stimulation (Figure 3.3A).Low-voltage stimulation (2 V) consistently produced less SEAP than the US baseline. At 7.5 V, there wasn't much change at short exposure, but after 24 hours, the response crept just above control levels. The 10 V series showed a steady boost as exposure got longer - by 8 and 24 hours, SEAP nearly matched or nudged past the US reference. In contrast, 20 V produced its strongest early response after 4 h of stimulation, reaching approximately 140% of US, followed by lower values at longer stimulation durations. The most pronounced short-duration response was observed at 40 V after 1 h, where SEAP reached approximately 280% of US; however, this condition displayed substantial variability and the response declined markedly as stimulation duration increased.

The 96-h SEAP endpoint revealed a different response pattern (Figure 3.3B). Since 2 V barely moved the needle in initial screens, we didn't bother measuring SEAP at 96 hours for that set. Of all the conditions left, 10 V stood out: after 8 and 24 hours, SEAP shot up to about 330-340% of control. In contrast, 7.5 V usually stayed at or below baseline, while 20 V gave a mild increase early but dropped off the longer stimulation continued. At 40 V, a strong response was observed after 1 h of stimulation, whereas longer stimulation periods resulted in substantially reduced SEAP levels. These findings indicate that increasing stimulation amplitude did not produce a proportional increase in reporter output and instead revealed a strong dependence on the interaction between voltage and exposure duration.

Metabolic activity measured at the final 96-h endpoint showed a general reduction relative to the corresponding US control as stimulation intensity and/or exposure duration increased (Figure 3.3C). Looking at metabolic activity, cells treated with 2 V held onto higher activity throughout. At 7.5 and 10 V, metabolism fell gradually as stimulation time increased, but the drop wasn't as sharp as for the higher voltages. With 20 V, activity fell even faster and hit very low levels after 24 hours. The highest tested voltage, 40 V, led to severe metabolic loss, especially with longer

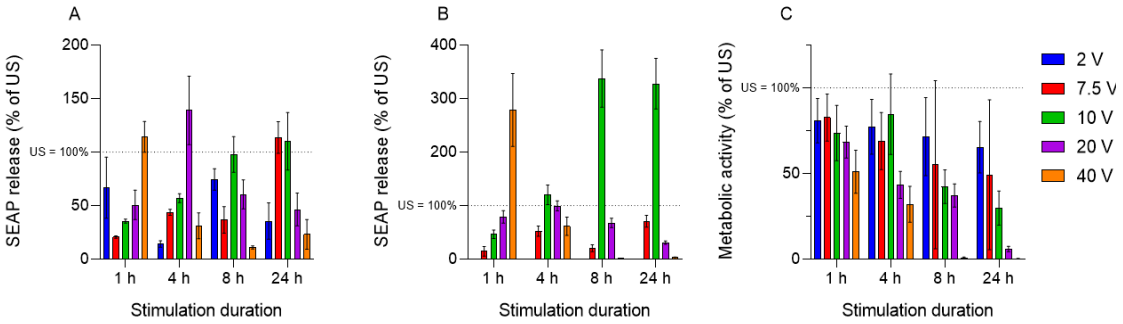


Figure 3.3: Exploratory electrical stimulation of non-encapsulated engineered HEK293 cells using the C-Dish/C-PACE platform. Cells were stimulated at 2, 7.5, 10, 20, or 40 V for 1, 4, 8, or 24 h. (A) SEAP response measured 24 h after initiation of stimulation. (B) SEAP response measured at the 96-h endpoint. The 96-h SEAP endpoint was not acquired for the 2 V series following the weak response observed during the initial exploratory screening. (C) MTT metabolic activity measurements at 96 hours were normalized to the corresponding unstimulated-electrode control (US = 100%) and are shown as mean ± SD, using three wells for each group. Dotted lines in the plots mark the US baseline. Because these voltage tests were run one after another as part of protocol refinement, we interpreted the trends descriptively, not as a single full-factorial experiment.

exposures.

Pulling it all together, the SEAP and MTT data point to a trade-off between voltage and stimulation time for activating these engineered HEK293 cells. Pushing the voltage high for short stretches could trigger strong reporter signals, but the effect faded - and metabolic health fell off - if the stimulation dragged on. Using intermediate voltages didn't cause a big immediate jump, but certain durations ended up supporting stronger SEAP outputs by the end of the run. In particular, among the exploratory conditions tested, 10 V combined with 8–24 h of stimulation generated the highest relative SEAP signal at 96 h, although this was accompanied by a reduction in metabolic activity.

The 96-h SEAP measurements represent accumulated reporter present in the culture medium rather than an instantaneous secretion rate at Day 4, since only a small supernatant sample was removed at the 24-h endpoint and the culture medium was not otherwise replaced. The high late SEAP signal observed in selected conditions therefore reflects the integrated consequence of electrically induced reporter expression, secretion, accumulation, and subsequent cellular persistence rather than sustained secretion by an unchanged viable cell population. These preliminary experiments were consequently used to define a practical stimulation window for subsequent protocol refinement rather than to identify a definitive optimal electrical condition.

3.2 In Vitro Characterization of Alginate and APA Microcapsules

The structural and biological properties of the encapsulation system were evaluated following fabrication of cell-loaded alginate beads and fully coated APA microcapsules. Characterization first focused on the morphology of the two formulations, followed by assessment of cellular viability, cell recovery, and molecular transport through the APA structure.

3.2.1 Morphological Characterization

Bright-field microscopy revealed clear morphological differences between cell-loaded alginate-only beads and fully coated APA microcapsules (Figure 3.4A,B). Alginate-only beads displayed greater heterogeneity in overall contour and shape, with a larger proportion of irregular and less uniformly rounded structures. In contrast, the final APA microcapsules exhibited more clearly defined boundaries and a more consistently rounded morphology.

Quantitative morphometric analysis of one representative fabrication batch per formulation confirmed differences in both equivalent diameter and circularity distributions (Figure 3.4C,D). The APA population showed a distribution shifted toward smaller equivalent diameters compared with the alginate-only population, together with a narrower distribution of measurements. Within the representative batches analyzed, the equivalent-diameter distributions differed significantly between the two formulations (Mann–Whitney U test, $p < 0.0001$).

A marked difference was also observed in circularity. Alginate-only beads displayed a broader distribution, including a substantial fraction of structures with lower circularity values, whereas APA microcapsules were predominantly concentrated close to a circularity index of 1. The object-level distributions in the batches they looked at were clearly different (Mann-Whitney U test, $p < 0.0001$). What they saw matched up with the bright-field images too - the final APA microcapsules looked more regular and had a more consistent shape overall.

The analysis included measurements from 100 individual structures were analyzed per group, using one representative batch of alginate-only beads and one of APA microcapsules. Additional batches generated using the same standardized fabrication parameters showed qualitatively comparable morphologies during routine bright-field inspection but were not included in the quantitative morphometric analysis. Accordingly, the statistical comparisons describe object-level differences within the representative batches and should not be interpreted as independent batch-level statistical replication.

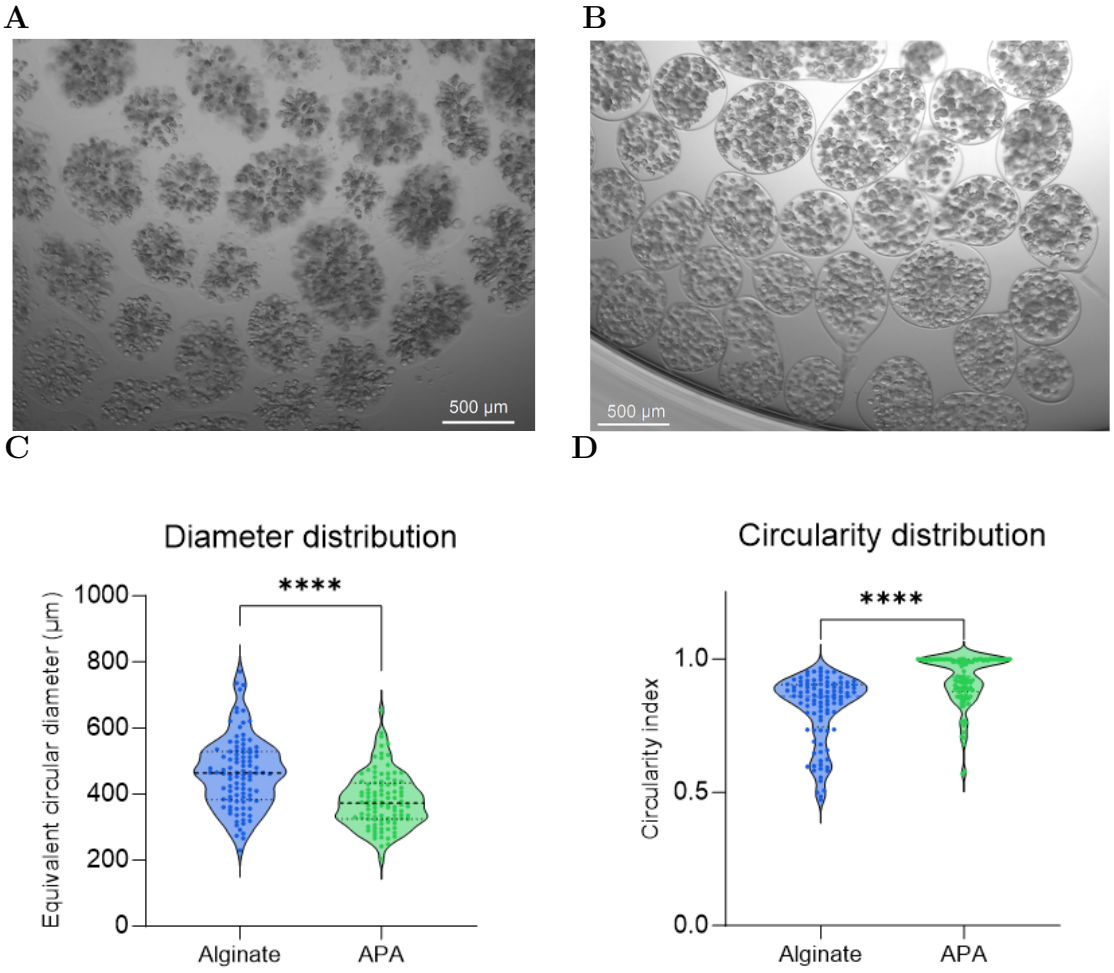


Figure 3.4: Morphological characterization of cell-loaded alginate-only beads and fully coated APA microcapsules. (A) Representative bright-field image of cell-loaded alginate-only beads. (B) Representative bright-field image of cell-loaded APA microcapsules. Scale bars, 500 μm. (C) Equivalent-diameter distribution and (D) circularity distribution of alginate-only beads and APA microcapsules. Quantitative morphometric analysis was performed on $n = 100$ individual structures per group from one representative fabrication batch for each formulation. Individual measurements are displayed within the violin distributions. Equivalent diameter and circularity distributions were compared using the Mann–Whitney U test; $^{****}p < 0.0001$. Statistical comparisons therefore represent object-level differences within the analyzed batches rather than independent batch-level replication.

3.2.2 Qualitative Assessment of Cell Viability within APA Microcapsules

Cell viability within APA microcapsules was qualitatively assessed by Live/Dead fluorescence staining at Days 0, 1, 3, and 7 following encapsulation. Representative images acquired in the Calcein AM and EthD-1 channels, together with the corresponding overlays, are shown in Figure 3.5. Calcein-positive cells were readily detectable within the capsules at all investigated time points, consistent with the persistence of viable cells within the APA environment throughout the 7-day observation period.

EthD-1-positive cells were also present at each time point, indicating that a fraction of the encapsulated population had lost membrane integrity during culture. Even when dead cells were present, the fluorescence images kept showing quite a few Calcein-positive (live) cells throughout the inside of the capsule, from Day 0 all the way to Day 7. Overlay images made it obvious that live and dead cells were mixed together inside a single capsule, letting you see where they were located compared to the capsule edge.

The amount and brightness of fluorescent cells changed from field to field and at different time points, but the Live/Dead assay was mostly used just to look at where cells were located, not to calculate the exact percentage of viable cells. Differences in fluorescence abundance between images were therefore not interpreted as direct temporal changes in the fraction of viable cells. Quantitative assessment of the recoverable cell population over time was instead performed independently through bead decapsulation and cell counting, as described in the following subsection.

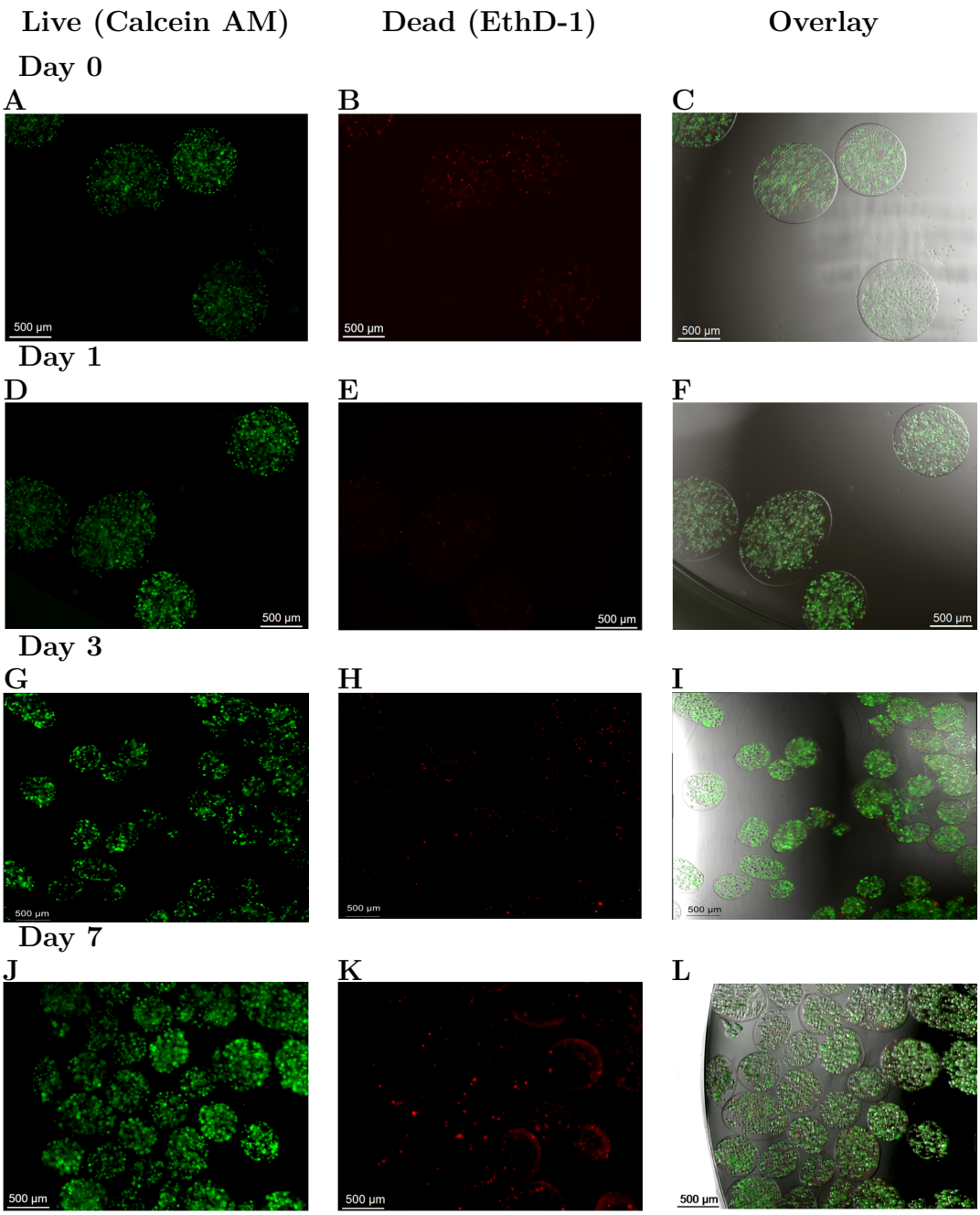


Figure 3.5: Live/Dead staining of engineered HEK293 cells in APA microcapsules across 7 days in culture. Typical fluorescence images are shown for Day 0 (A-C), Day 1 (D-F), Day 3 (G-I), and Day 7 (J-L). Calcein AM staining marks cells with intact membranes and active esterases (so they're alive), while EthD-1 highlights cells with damaged membranes. The overlay shows where live and dead cells are positioned within the capsules. Scale bars, 500 μm. The assay was used for qualitative visualization of cell viability and distribution and was not used to derive quantitative viability percentages.

3.2.3 Longitudinal Cell Recovery from Alginate Beads

Decapsulation-based cell recovery was used to follow the recoverable cell population within alginate-only beads over 7 days of culture. Alginate-only beads were analyzed because they could be reproducibly dissolved using citrate/EDTA, whereas mature APA microcapsules could not be consistently decapsulated without introducing additional variability in cell recovery. Pictures of the capsules before and after dissolving the beads are in Figure 3.6D,E.

The total number of cells you could recover from each bead went up over the course of the experiment (see Figure 3.6A). There were around 400-500 cells per bead at Days 0 and 1, which then climbed to about 900 cells per bead by Day 3 and roughly 1700 by Day 7. So even though not much changed in the first 24 hours after encapsulation, between Days 1 and 7, the number of recoverable cells grew quite a bit.

Viability (measured by trypan-blue exclusion and shown in Figure 3.6B) didn't follow the same trend. Right after encapsulation, only about 40% of the cells were alive. That jumped to about 60-65% on Day 1, peaked close to 95% on Day 3, and then dropped back to around 70% by Day 7. The low viability at Day 0 lines up with the stress cells go through during encapsulation and recovery, while the big improvement by Day 3 shows that a steady population of live cells made it through the early adjustment period inside the hydrogel.

Analysis of the absolute numbers of live and dead recovered cells provided additional information beyond viability percentage alone (Figure 3.6C). At Day 0, dead recovered cells represented a substantial fraction of the total recoverable population. By Day 3, the marked increase in total recovered cells was driven predominantly by the live-cell fraction, with comparatively few dead cells recovered. Although the percentage viability declined between Days 3 and 7, the absolute number of recovered live cells continued to increase because the total recoverable cell population was substantially larger at Day 7. Consequently, the decrease in percentage viability at the final time point did not correspond to a reduction in the absolute number of viable cells recovered per bead.

The progressive increase in recovered cell number is compatible with expansion of the encapsulated cell population during culture. However, the decapsulation assay quantifies cells successfully retrieved after bead dissolution rather than directly tracking cell division within individual beads. Temporal differences in recovery efficiency, cell aggregation, or susceptibility to the decapsulation procedure could therefore also contribute to the measured values. For this reason, the observed increase was interpreted as an expansion of the *recoverable cell population* rather than as a direct quantitative measurement of proliferation.

The variability shown in Figure 3.6A,B reflects repeated technical measurements of the same pooled recovered-cell suspension at each time point. Three subsamples

were analyzed using both chambers of the automated cell-counting slide, generating six technical readings per time point. These measurements characterize technical counting variability and do not represent independent biological replicates; accordingly, no inferential statistical comparisons between time points were performed.

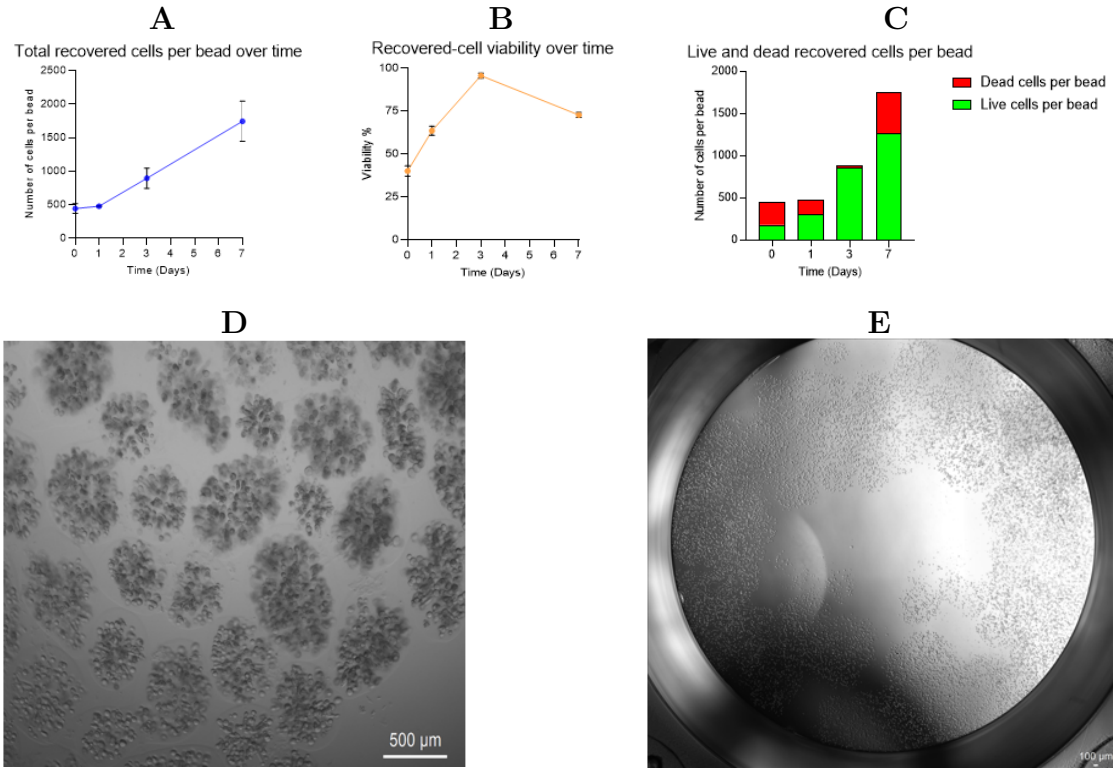


Figure 3.6: Longitudinal recovery of engineered HEK293 cells from alginate-only beads over 7 days of culture. (A) Number of total recovered cells per bead at Days 0, 1, 3, and 7. (B) Viability of the recovered cells using trypan-blue exclusion. (C) Numbers of live and dead cells recovered from each bead at each measured time. (D) Bright-field image of cell-filled alginate beads before dissolving. (E) Typical field after breaking down the beads with citrate/EDTA, releasing the encapsulated cells. The reported recovery values were calculated based on the combined number of beads in each pooled sample. For each time point, three subsamples of the pooled recovered-cell suspension were measured in both chambers of the automated cell-counting slide, yielding six technical readings. Data in (A) and (B) are presented as mean ± SD of these six technical measurements. The error bars therefore represent technical counting variability and not independent biological replication.

3.2.4 Molecular Transport through APA Microcapsules

Molecular transport through the APA microcapsule structure was evaluated using fluorescent dextrans spanning molecular weights from 3 to 70 kDa. After correcting

for background, fluorescence measurements at the capsule center showed clear differences in how the four tracers moved inside (Figure 3.7A). The 3 and 10 kDa dextrans quickly built up fluorescence in the center, reaching levels near their eventual maximum within just the first several minutes. In comparison, the 40 and 70 kDa tracers took much longer for their signal to rise, pointing to a slower movement into the capsule core.

For the 3 kDa tracer, the signal jumped up fast and then stayed about the same for the rest of the experiment. The 10 kDa dextran followed a similar pattern - rising quickly, leveling off early, and not changing much after that. The larger tracers acted differently: the 40 kDa dextran climbed steadily for about an hour, then started to vary more as time passed, while the 70 kDa tracer kept increasing slowly and only started to flatten out near the end of the observation window.

Because the dextrans were conjugated to different fluorophores, absolute fluorescence amplitudes were not directly compared across molecular-weight groups. Instead, center fluorescence for each tracer was normalized to its corresponding plateau value, allowing comparison of the relative progression toward the tracer-specific plateau signal observed over the measured time course (Figure 3.7B). Over the common 0–60 min interval, both low-molecular-weight tracers approached their plateau rapidly, whereas the 40 and 70 kDa dextrans displayed slower normalized penetration kinetics. This split between the small and large tracers showed up most clearly right at the start. When looking at sample fluorescence images for the 3 and 10 kDa dextrans (Figure 3.8), you could already see the tracers inside the capsule early on, and soon the signal spread throughout the capsule as incubation continued. These examples were used because the smaller tracers made it easy to see where they went, thanks to their strong fluorescence contrast. Since the low-molecular-weight tracers were so visible, most of the quantitative comparison between tracers was done using the center fluorescence measurements, not just the microscopy snapshots.

Overall, the data show that APA microcapsules let dextran molecules move inward across the whole range of tested molecular weights, but the bigger tracers made their way in more slowly. This experiment was set up to look at relative transport rates, not to determine an exact permeability value or to define a strict molecular-weight limit for the APA membrane.

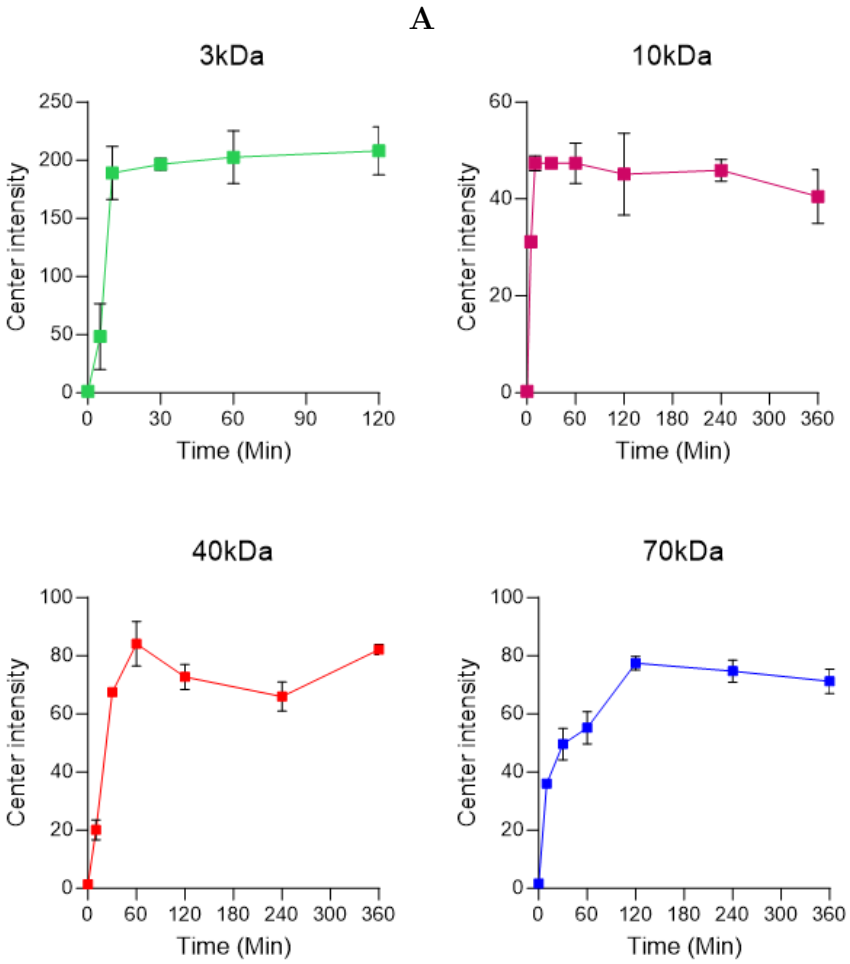


Figure 3.7: Molecular-weight-dependent penetration of fluorescent dextrans into empty APA microcapsules. (A) Background-corrected center-fluorescence kinetics measured independently for 3, 10, 40, and 70 kDa dextrans over their respective observation periods. Data are presented as mean ± SD from six independent APA microcapsules ($n = 6$) analyzed at each tracer and time point. Because the 3 and 10 kDa dextrans were tetramethylrhodamine-labeled whereas the 40 and 70 kDa dextrans were Texas Red-labeled, raw fluorescence amplitudes were not directly compared between tracers.

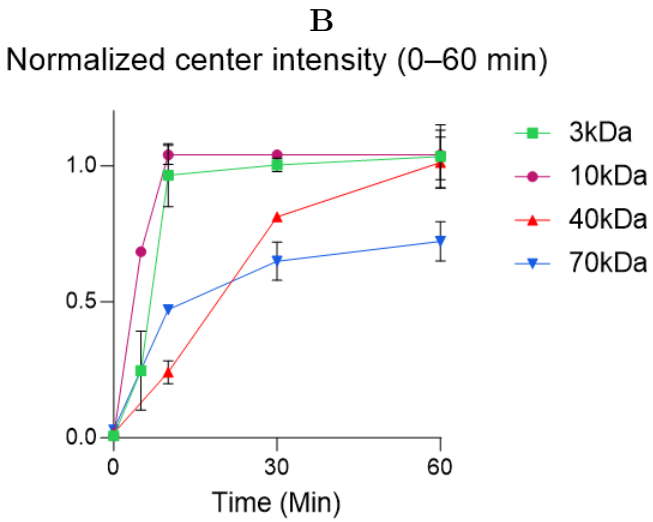


Figure 3.7: Molecular-weight-dependent penetration of fluorescent dextrans into empty APA microcapsules, continued. (B) Comparison of normalized center fluorescence over the common 0–60 min interval. For each tracer, fluorescence values were normalized to the corresponding plateau value measured over its complete time course.

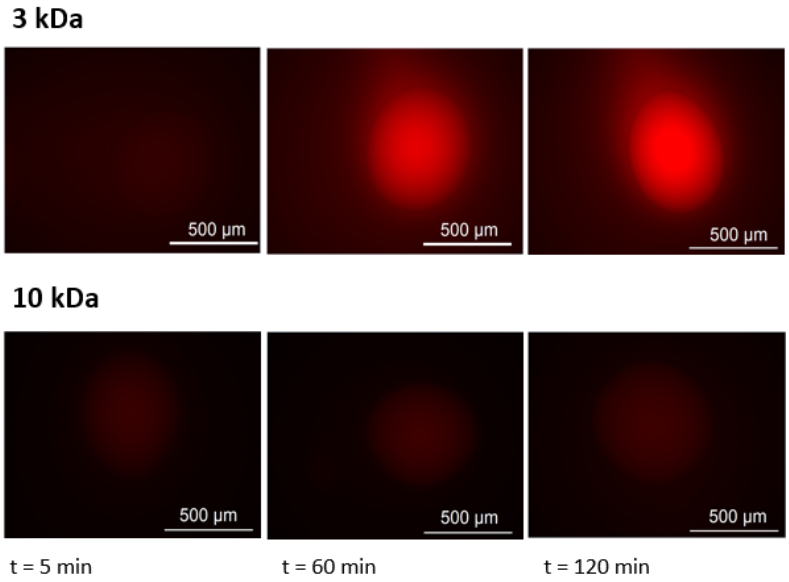


Figure 3.8: Representative fluorescence images illustrating penetration of low-molecular-weight dextrans into empty APA microcapsules. Images show 3 kDa and 10 kDa fluorescent dextrans at 5, 60, and 120 min after tracer exposure. The images are presented as qualitative examples of spatial tracer penetration and were not used for direct cross-tracer comparison of fluorescence magnitude. Scale bars, 500 μm.

3.3 Functional Characterization of Encapsulated Cells

Following structural and transport characterization of the encapsulation system, the functional behavior of the engineered cells was evaluated by measuring basal SEAP secretion and cellular metabolic activity. Non-encapsulated adherent cells, non-encapsulated cells cultured under non-adherent conditions, and APA-encapsulated cells were compared over 7 days to determine whether encapsulation altered basal reporter output or the maintenance of cellular metabolic activity.

3.3.1 Basal SEAP Secretion and Metabolic Activity

All three culture configurations showed progressive accumulation of SEAP over the 7-day observation period (Figure 3.9A). Accumulated SEAP remained comparatively low during the first 3 days and increased markedly between Days 3 and 7. At the end point, APA-encapsulated cells had the highest total SEAP release, around 780 ng. Non-encapsulated cells grown without attachment came in just behind at about 750 ng. Adherent cells had a smaller total - roughly 650 ng. Even in the first three days, you could already see these gaps, with the APA-encapsulated cells trending higher from the start.

So, APA encapsulation didn't block the constant reporter protein from getting out - those cells still released SEAP into the medium. The fact that APA-encapsulated and non-adherent cells ended up with similarly high SEAP levels by Day 7 suggests that: the hydrogel environment was compatible with basal reporter production, over the seven-day culture period. Since each measurement tracked SEAP built up in separate cultures over time - not the immediate secretion rate - the reported numbers show the amount of SEAP, accumulated in the culture medium by each endpoint.

Metabolic activity changed differently depending on the culture setup (Figure 3.9B). Each group's data was normalized to its own Day 1 value (set as 100%). Because PrestoBlue incubation times weren't the same for naked and APA-encapsulated cells, the results mainly show how activity changed over time within each group rather than allowing direct comparison between groups. Adherent cells had a sharp jump in activity at Day 3, peaking around 150% of the starting value, but then dropped off a bit by Day 7 (still above where they began). In contrast, non-adherent cells displayed a reduction in relative metabolic activity at Day 3 before recovering to approximately the Day 1 level by Day 7. APA-encapsulated cells maintained a more moderate but progressive increase, reaching approximately 110% at Day 3 and 120% at Day 7.

The PrestoBlue assay reflects overall metabolic activity and was therefore not

interpreted as a direct measurement of viable cell number or proliferation. Nevertheless, the maintenance of metabolic activity above the Day 1 reference in the APA condition, together with the strong increase in accumulated SEAP by Day 7, supported the persistence of a functionally active encapsulated-cell population. Representative bright-field images acquired at Day 7 further illustrated the different cellular organizations generated by the two non-adherent environments (Figure 3.9C,D). Non-encapsulated cells cultured in non-adherent plates formed discrete three-dimensional aggregates, whereas APA microcapsules retained densely populated cellular structures within the hydrogel compartment.

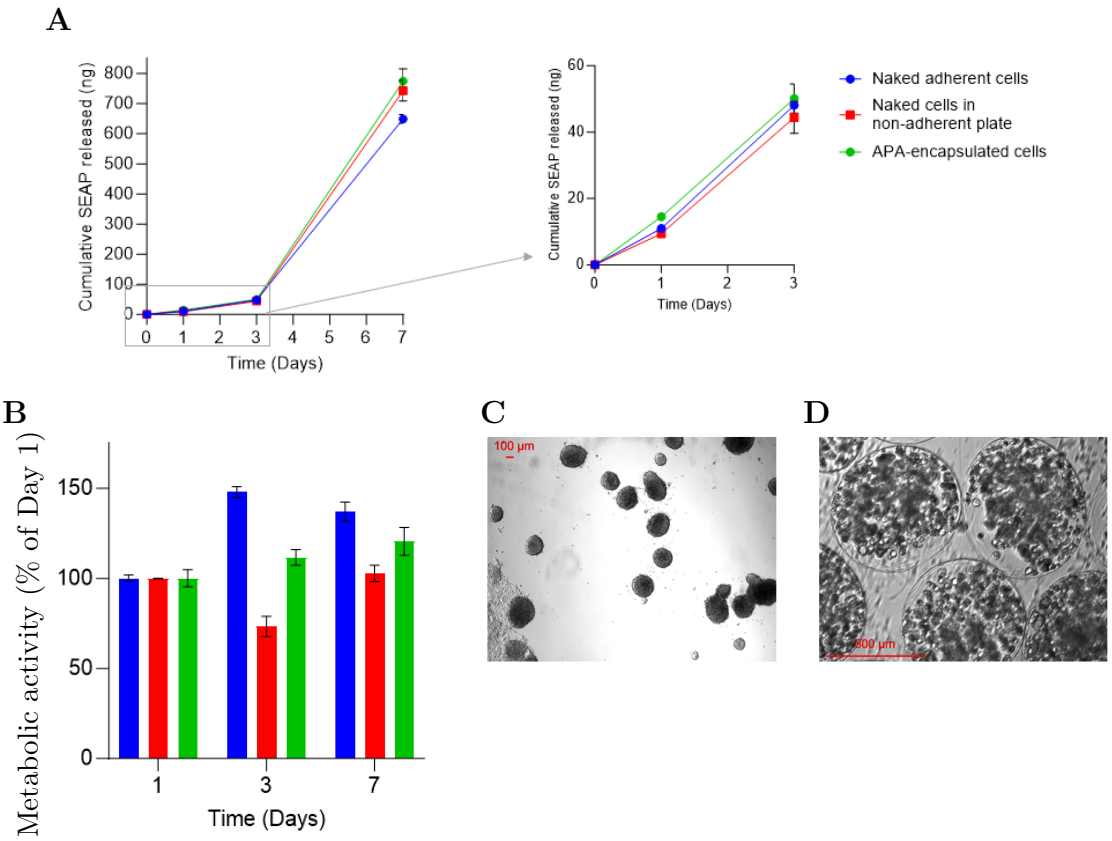


Figure 3.9: Basal functional characterization of engineered HEK293 cells cultured under adherent, non-adherent, or APA-encapsulated conditions. (A) Cumulative SEAP release measured at Days 1, 3, and 7. The enlarged inset shows the early 0–3-day interval to facilitate visualization of differences that are compressed by the larger Day 7 response. (B) Relative metabolic activity measured using PrestoBlue and normalized within each culture condition to the corresponding Day 1 value, defined as 100%. (C) Representative bright-field image at Day 7 of non-encapsulated engineered HEK293 cells cultured in a non-adherent plate, showing formation of three-dimensional cellular aggregates. (D) Representative bright-field image at Day 7 of APA-encapsulated engineered HEK293 cells. Scale bars are indicated within the corresponding microscopy panels. Cell-containing conditions were evaluated in triplicate, and quantitative data are presented as mean ± SD. PrestoBlue measurements represent relative metabolic activity and were not interpreted as direct measurements of cell number or viability.

3.3.2 Chemical Depolarization with KCl

Sustained chemical depolarization with 60 mM KCl produced a marked increase in SEAP output in both non-encapsulated and APA-encapsulated engineered HEK293 cells (Figure 3.10A). SEAP release was expressed as fold-change relative to the corresponding untreated condition, defined as 1. On Day 1, KCl-treated nonencapsulated cells pumped out about 16 times more SEAP, while APA-encapsulated cells had about a 10-fold increase. This strong output kept up on Day 3, with nonencapsulated cells still showing around 15-fold induction and APA-encapsulated ones at about 12-fold. Even inside the multilayer hydrogel, encapsulated cells held on to their ability to trigger the depolarization-sensitive Ca2+ /NFAT pathway, which says a lot about how well they function in the APA setup. Although the magnitude of KCl-induced SEAP release was lower in APA-encapsulated cells than in the corresponding non-encapsulated condition, substantial reporter induction was maintained at both investigated time points.

The pronounced secretory response was accompanied by a substantial reduction in cellular metabolic activity after 72 h of continuous KCl exposure (Figure 3.10B). At Day 3, metabolic activity corresponded to approximately 35% of the untreated reference in non-encapsulated cells and approximately 32% in APA-encapsulated cells. Thus, prolonged depolarization produced strong functional activation but was associated with a marked reduction in metabolic activity in both culture configurations.

Taken together, these data indicate that APA encapsulation preserved the ability of the engineered HEK293 cells to respond to membrane depolarization and activate SEAP production. At the same time, the reduced metabolic activity observed following sustained 60 mM KCl exposure indicates a clear activation–tolerability trade-off. The KCl condition was therefore interpreted as a strong positive functional stimulus rather than as an optimized long-term activation regime.

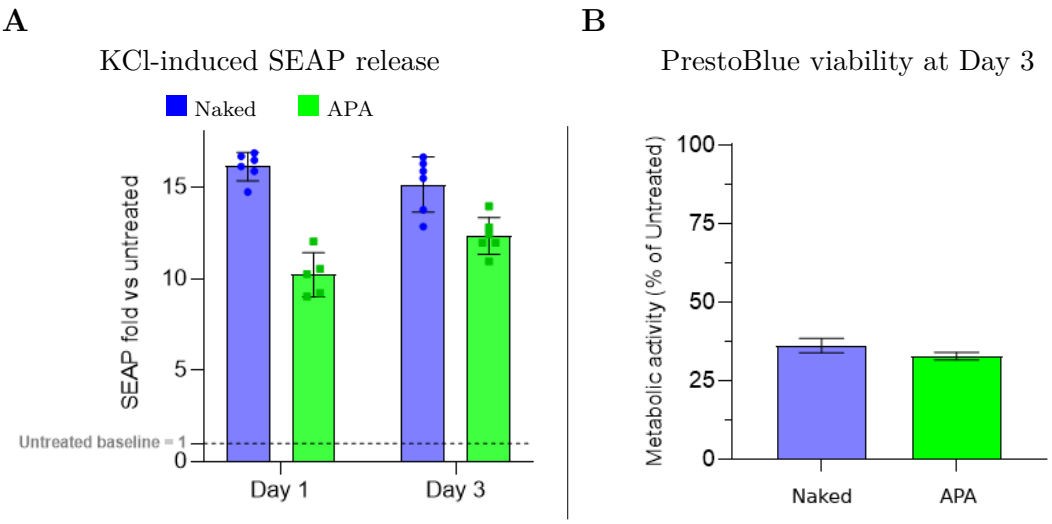


Figure 3.10: Functional response of engineered HEK293 cells to sustained chemical depolarization with 60 mM KCl. (A) KCl-induced SEAP release at Days 1 and 3 in non-encapsulated and APA-encapsulated cells, expressed as fold-change relative to the corresponding untreated condition, defined as 1. (B) Metabolic activity measured by PrestoBlue at Day 3 and expressed as a percentage of the corresponding untreated condition, defined as 100%. Data are presented as mean ± SD from six independent wells per condition ($n = 6$). KCl exposure was maintained continuously for 72 h. PrestoBlue measurements were interpreted as relative metabolic activity and not as a direct measurement of cell viability or cell number.

3.3.3 Electrical Stimulation of APA-Encapsulated Cells

Electrical stimulation of APA-encapsulated engineered HEK293 cells was first explored using the C-Dish/C-PACE platform. These early tests were meant to screen different variables - stimulus strength, how long the stimulation lasted, medium volume, and the C-Dish setup changed from run to run. Because of all these differences, we didn't treat the data as a uniform, controlled set. Instead, the goal here was to figure out which stimulation conditions could produce measurable SEAP responses while still letting the cells stay active, giving us a practical starting point for more focused experiments with the custom electrode.

The stimulation parameters identified during the C-Dish screening phase were not transferred directly to the custom platform, because electrode spacing, exposed surface area, bead distribution, medium geometry, and current distribution differed substantially between the two systems. The exploratory experiments were therefore used only to guide selection of the initial voltage range for the subsequent device-relevant stimulation experiment.

A standardized experiment was then performed using a custom-made configuration consisting of an upper and a lower platinum-mesh electrode, with APA microcapsules positioned within the stimulation region between the two opposing surfaces

(Figure 2.4). The electrodes were connected to the external stimulation source through platinum wires, and the encapsulated cells were stimulated for 4 h at 2.5, 5, 10, or 20 V. SEAP output was evaluated at Days 1 and 3 and normalized to the corresponding unstimulated electrode-control condition, which was defined as a fold-change of 1.

At Day 1, the strongest SEAP response was observed at 5 V, reaching approximately 1.5-fold relative to the unstimulated electrode control (Figure 3.11A). Lower stimulation levels of 2.5 V and 10 V only boosted SEAP output by about 1.2 times compared to controls. Cranking it up to 20 V, on the other hand, nearly wiped out SEAP production - levels dropped close to zero.

By Day 3, things looked a bit different: SEAP output at 2.5 V stayed just slightly higher than the baseline, while the 5 V condition ended up about the same as the control on average but with a lot of variability between wells. The 10 V condition actually slipped under the control level, and 20 V once again left almost no SEAP response. So, the strong initial SEAP boost at 5 V didn't stick around at the later time point.

Metabolic activity measured at Day 3 showed a clear decline depending on the voltage(see Figure 3.11B). At 2.5 V, metabolic activity was still about 70% of what was seen in unstimulated controls. This decreased to approximately 50% at 5 V and to approximately 35–40% at 10 V. At 20 V, metabolic activity was reduced to only approximately 5% of the unstimulated reference, indicating a severe reduction in cellular metabolic activity under the highest stimulation amplitude.

When SEAP output and metabolic activity were considered together, the custom-electrode experiment revealed a clear stimulation–tolerability trade-off. Among the tested conditions, 5 V produced the largest early increase in SEAP release, while retaining greater metabolic activity than the 10- and 20-V groups. Although 5 V produced the strongest early SEAP response, the increase was modest and wasn't maintained at Day 3. These results don't point to a single best stimulation setup. Instead, they suggest an initial range to work with as we fine-tune settings like amplitude, exposure time, waveform, and other electrical details specific to the device. The dramatic drop in metabolic activity and the almost total SEAP shutdown at 20 V make it clear that pushing the intensity too high doesn't sit well with APA-encapsulated cells in this setup.

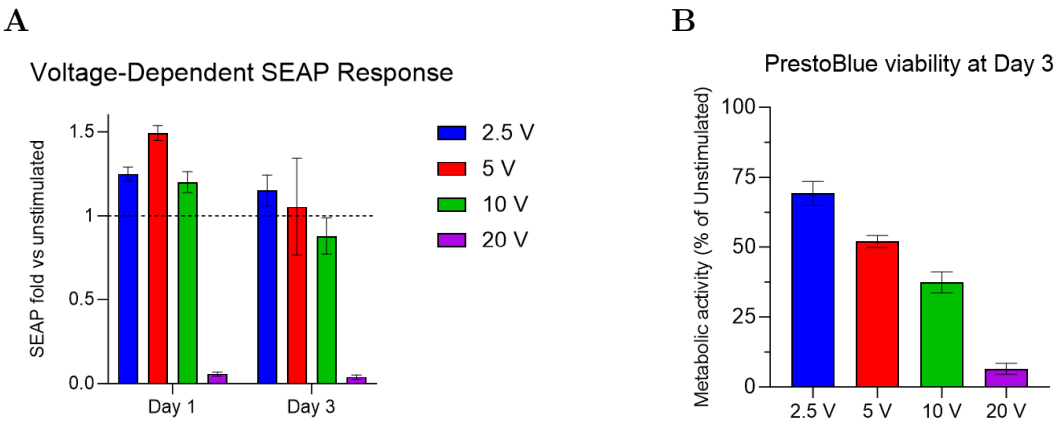


Figure 3.11: Functional response of APA-encapsulated engineered HEK293 cells to electrical stimulation using the custom platinum-mesh electrode configuration. (A) SEAP response measured at Days 1 and 3 following 4 h of stimulation at 2.5, 5, 10, or 20 V. SEAP output was normalized to the corresponding unstimulated electrode-control condition, defined as 1; the dashed horizontal line indicates this reference. (B) Metabolic activity measured by PrestoBlue at Day 3 and normalized to the unstimulated electrode-control condition, defined as 100%. Data are presented as mean ± SD from three replicate wells per condition ($n = 3$). PrestoBlue measurements were interpreted as relative metabolic activity rather than as a direct measurement of cell viability or cell number.

3.4 In Vitro Immunocompatibility and Immunoresistance Assessment

The interaction between the APA encapsulation system and immune cells was evaluated using a two-stage in vitro approach. An initial screening experiment was performed with RAW 264.7 macrophages to assess the innate inflammatory response associated with empty and cell-loaded APA microcapsules. This was followed by a more complex challenge using primary rat splenocytes, incorporating cytokine secretion, parallel assessment of SEAP production from the engineered-cell payload, flow-cytometric characterization of splenocyte viability and T-cell activation-associated markers, and CFSE acquisition as an intended proliferation readout.

3.4.1 RAW 264.7 Macrophage Response to APA Microcapsules

The preliminary macrophage co-culture assay was used to determine whether exposure to empty or cell-loaded APA microcapsules induced an early TNF-α response in RAW 264.7 cells. During the first 24 h of culture, TNF-α concentrations

remained at or below the lower bound of the reliably quantifiable standard-curve range (31.3 pg/mL) across the analyzed conditions (Figure 3.12A). No reliably quantifiable early increase in TNF-α was therefore detected following macrophage exposure to either empty or cell-loaded APA microcapsules.

A clear increase in TNF-α concentration became apparent at the 72-h endpoint in the macrophage-containing groups. RAW 264.7 cells cultured alone reached approximately 130 pg/mL, while RAW cells co-cultured with empty APA microcapsules showed a similar concentration of approximately 135–140 pg/mL. The RAW + cell-loaded APA setup had the highest average TNF-α levels, hitting around 220-230 pg/mL (see Figure 3.12B). When cell-loaded APA microcapsules were kept without macrophages, TNF-α stayed at the very low end of the measurable range, which basically shows that the TNF- in co-culture mostly came from the macrophages themselves.

Although the RAW + cell-loaded APA group showed higher TNF-α after 72 hours than the RAW + empty APA group, this difference didn't reach statistical significance by one-way ANOVA with Dunnett's test. So, there isn't solid evidence that adding the engineered cells inside the capsules triggered a bigger macrophage inflammatory response compared to using the APA material by itself. In fact, there wasn't any reliably measurable increase in TNF-α within the first 24 hours. TNF-α levels only went up after 72 hours in all groups with macrophages. The LPS-stimulated RAW 264.7 condition generated a markedly stronger TNF-α response than the principal experimental groups and confirmed the responsiveness of the macrophage model to a defined pro-inflammatory stimulus. Because the magnitude of the LPS response was substantially greater than that of the APA-containing and basal macrophage conditions, it was not included in Figure 3.12 to preserve visualization of the lower-range experimental responses.

Because RAW 264.7 cells are a simplified model for innate immunity, this was taken mainly as a basic check for immune compatibility - not proof that the encapsulation fully isolated or protected the cells from an immune response. The TNF-α spike showed up late, and there was a lot of variability at 72 hours, which led to further testing with primary rat splenocytes. This approach uses a broader mix of immune cells and lets you track both secreted inflammatory signals and lymphocyte activation.

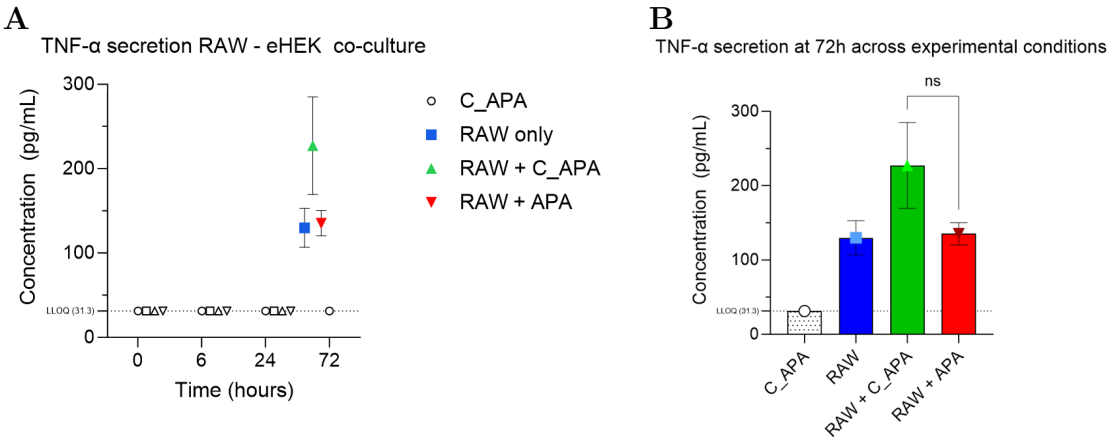


Figure 3.12: TNF-α response of RAW 264.7 macrophages following exposure to APA microcapsules. (A) Time-course analysis of TNF-α secretion at 0, 6, 24, and 72 h in cell-loaded APA microcapsules without macrophages (C_APA), RAW 264.7 cells alone, RAW cells co-cultured with cell-loaded APA microcapsules, and RAW cells co-cultured with empty APA microcapsules. (B) Comparison of TNF-α concentrations among experimental conditions at 72 h. The numbers here are shown as mean $\pm$ SD for three wells per condition ($n = 3$). The dashed horizontal line on the graph marks the lowest reliable measurement at 31.3 pg/mL; anything falling below this is shown at the threshold value for clarity. One-way ANOVA with Dunnett's test was used for group comparisons. At 72 hours, there was no statistically significant difference (ns) between RAW + cell-loaded APA and RAW + empty APA groups.

3.4.2 Primary Rat Splenocyte Challenge

Following the preliminary RAW 264.7 macrophage assay, the APA encapsulation system was evaluated in a more complex immune environment using primary rat splenocytes. The experiment combined soluble inflammatory readouts with measurement of SEAP secretion from the engineered-cell payload and flow-cytometric characterization of splenocyte viability and T-cell activation-associated markers.
TNF-α production showed a predominantly early response following establishment of the co-cultures (Figure 3.13). At 24 hours, splenocytes alone produced about 42 pg/mL of TNF-α. When co-cultured with cell-loaded APA microcapsules, average TNF-α shot up to roughly 143 pg/mL. Empty APA microcapsules gave the largest mean TNF-α response out of the main groups, reaching around 238 pg/mL, though the results varied a lot from well to well. Naked engineered HEK293 cells grown with splenocytes produced about 49 pg/mL - nearly the same as splenocytes by themselves. Cell-loaded APA microcapsules maintained without splenocytes remained at approximately 48 pg/mL.
By 72 h, TNF-α concentrations in the principal experimental groups had converged toward substantially lower values, generally ranging from approximately 33 to 59 pg/mL. This pattern was consistent with a stronger response during the earlier

phase of the immune challenge. However, because only a partial medium replacement was performed at 24 h, the 72-h samples contained contributions from both analyte remaining after the partial medium replacement and additional production during the subsequent 24–72-h period and were therefore not interpreted as isolated 24–72-h secretion measurements. LPS-stimulated splenocytes produced a much stronger TNF-α response than the main experimental groups, which confirms that the primary splenocyte prep was fully able to trigger a strong inflammatory reaction in these experiments. Since the LPS condition mainly served as a positive control and its signal ended up at the very top, or even above, the range used for direct comparison, it wasn't included in the main graphs.
The lowest concentration included in the TNF-α standard curve was 31.3 pg/mL and was therefore used as the operational lower bound of the reliably quantifiable standard-curve range for interpretation of the experimental data. Values approaching or falling below this threshold were not interpreted as precise quantitative differences.

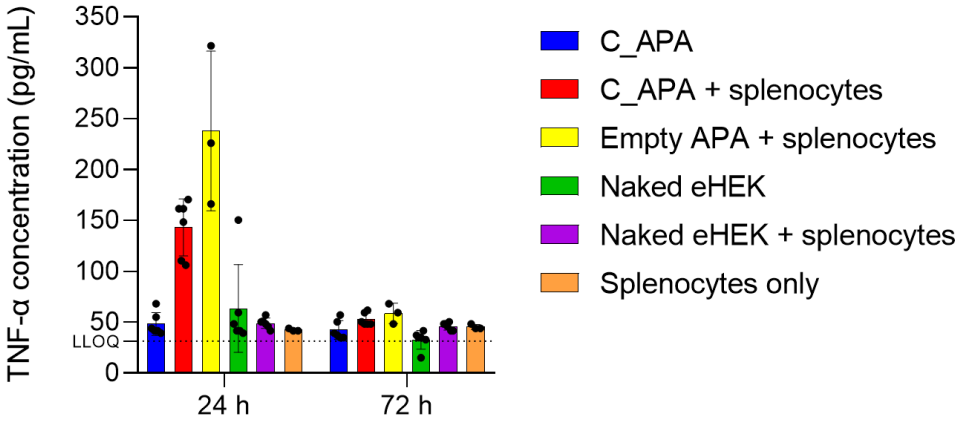


Figure 3.13: TNF-α production during the primary rat splenocyte challenge. TNF-α concentrations were measured at 24 and 72 h in cell-loaded APA microcapsules without splenocytes (C_APA), cell-loaded APA microcapsules co-cultured with splenocytes, empty APA microcapsules co-cultured with splenocytes, naked engineered HEK293 cells, naked engineered HEK293 cells co-cultured with splenocytes, and splenocytes cultured alone. Each point in the plots shows a separate replicate well, and the bars give the mean ± SD. The dashed horizontal line marks the lowest reliably quantifiable value on the standard curve (31.3 pg/mL). LPS-stimulated splenocytes were looked at on their own as the positive control and aren't shown with the others, since their TNF-α concentrations were so high that they needed a different scale.

IL-6 levels were also checked at 24 and 72 hours as another inflammatory measure, but the assay didn't give a strong enough quantitative signal to really compare biological differences. The standard curve didn't work well at the concentrations seen in the samples, and most measured values were pretty close to background.

Even the LPS control didn't show a clear IL-6 response in these conditions. The IL-6 dataset was therefore not included in the quantitative comparative analysis, and the absence of an interpretable signal was considered an analytical limitation rather than evidence of absent IL-6 production.
Functional activity of the engineered-cell payload was evaluated in parallel by quantifying SEAP amounts measured in the culture supernatants (Figure 3.14). At Day 1, cell-loaded APA microcapsules maintained without splenocytes produced approximately 13 ng SEAP, whereas the corresponding splenocyte co-culture produced approximately 59 ng. A similar but smaller jump was seen in naked engineered cells: SEAP levels rose from about 4 ng without splenocytes to roughly 13 ng when splenocytes were present. By Day 3, that difference got even bigger. Cell-loaded APA microcapsules kept on their own showed about 21 ng SEAP in the supernatant, while those mixed with splenocytes hit around 125 ng. Naked engineered cells increased from approximately 24 ng without splenocytes to approximately 49 ng in the corresponding co-culture. Thus, exposure to the primary immune-cell population was associated with increased SEAP output in both cellular configurations, with the largest difference observed for APA-encapsulated cells. Because SEAP expression is controlled by the electrogenetic NFAT-responsive circuit, the increased reporter output was interpreted as altered functional activity during immune co-culture rather than as direct evidence of enhanced cell number, improved viability, or immunoprotection. As for the cytokine measurements, the Day 3 samples contained residual reporter remaining after the partial medium replacement together with subsequently secreted SEAP and were therefore interpreted as endpoint reporter amounts rather than as an isolated secretion interval.

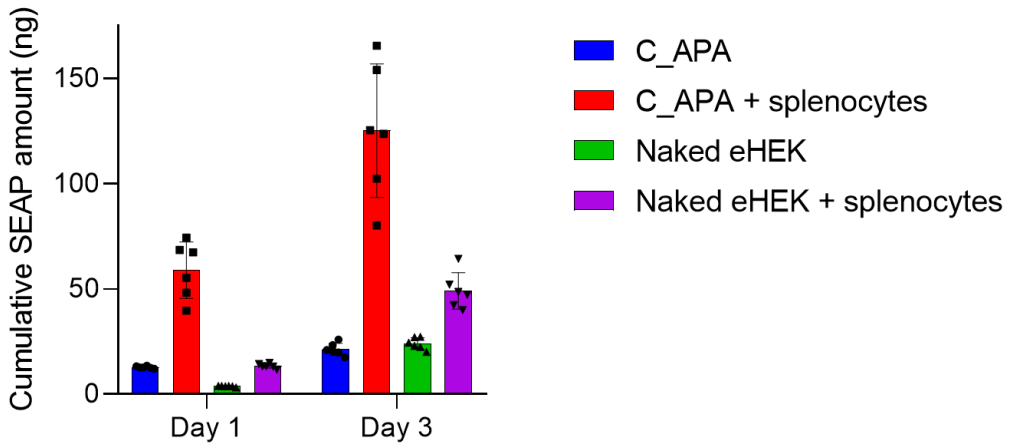


Figure 3.14: SEAP amounts measured during the primary rat splenocyte challenge. Cell-loaded APA microcapsules (C_APA) and naked engineered HEK293 cells were maintained either alone or in co-culture with primary rat splenocytes. SEAP amounts were determined at Day 1 and Day 3. Individual points represent replicate wells and bars show mean ± SD ($n = 6$ per condition).

Flow cytometry was subsequently used to characterize the splenocyte population recovered at the experimental endpoint. The proportion of live cells remained broadly comparable among the principal untreated experimental conditions (Figure 3.15). Cell-loaded APA + splenocyte cultures, empty APA + splenocyte cultures, naked engineered-cell + splenocyte cultures, and splenocytes cultured alone showed mean live-cell fractions of approximately 76–79%. LPS-stimulated splenocytes showed a lower mean viability of approximately 70%, whereas the PHA-treated group remained close to 77%. These observations indicated that exposure to cell-loaded APA microcapsules did not produce an obvious loss of splenocyte viability relative to the corresponding untreated comparator groups.

One acquisition from the cell-loaded APA + splenocyte group failed to yield a sufficient number of events within the initial scatter gate and was excluded from downstream flow-cytometric analysis. Consequently, five evaluable samples were available for this condition, whereas the originally prepared replicate numbers were retained for the remaining groups.

T-cell activation-associated phenotypes were examined within the $CD3^+$ population using CD25 and CD44 expression (Figure 3.16). The proportion of $CD4^+CD25^+$ T cells remained highly similar across the principal untreated conditions, with mean values of approximately 9–10%. Cell-loaded APA + splenocytes, empty APA + splenocytes, naked engineered HEK293 cells + splenocytes, and splenocytes alone therefore showed no clear separation in this readout. LPS-treated splenocytes displayed a lower mean $CD4^+CD25^+$ fraction of approximately 6.6%, while the PHA-stimulated condition remained near 9%.

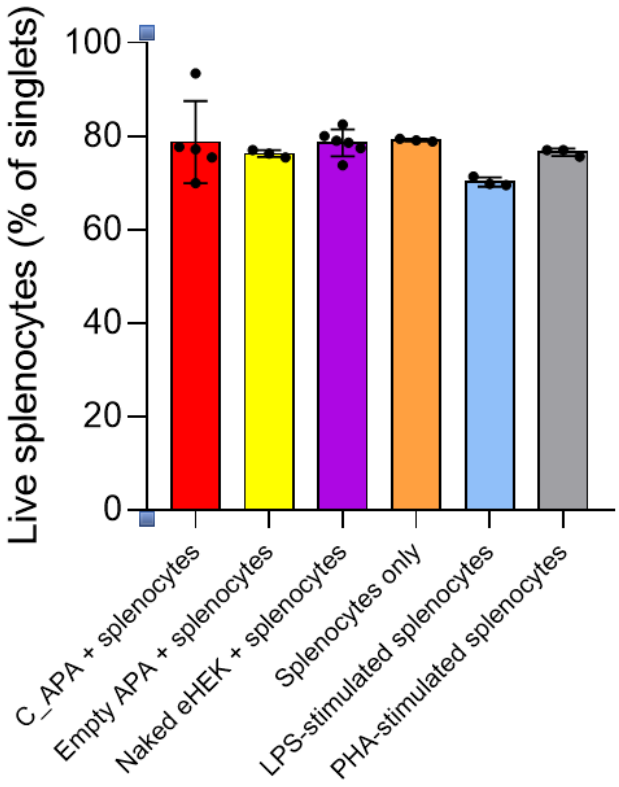


Figure 3.15: Viability of primary rat splenocytes following the 72-h immune challenge. Live cells were identified using LIVE/DEAD Fixable Blue following singlet discrimination and are expressed as a percentage of singlets. Individual points represent evaluable wells and bars show mean ± SD. For the cell-loaded APA plus splenocyte group, five samples were usable because one had to be thrown out (not enough valid events). For other groups, n was either 3 or 6, depending on the experiment.

There was a similar but only slight change for $CD4^+CD44^+$ T cells. With APA plus splenocytes, the average percentage crept up to about 67-68%, versus 62-64% in the other conditions. Still, neither LPS nor PHA caused a strong jump in $CD4^+CD44^+$ frequency compared to unstimulated splenocytes. Because of that, results for CD25 and CD44 were just described but not used to make any firm claims about T-cell activation or suppression. The PHA positive control in particular failed to show the sharp separation you'd expect, making it tough to draw any real conclusions from these activation marker results.
CFSE fluorescence was acquired as an intended measure of splenocyte proliferation. However, the acquired profiles did not show a clearly resolved CFSE-dilution pattern or distinct proliferation generations relative to the PHA-stimulated positive-control condition. In the absence of a robust positive-control separation and a

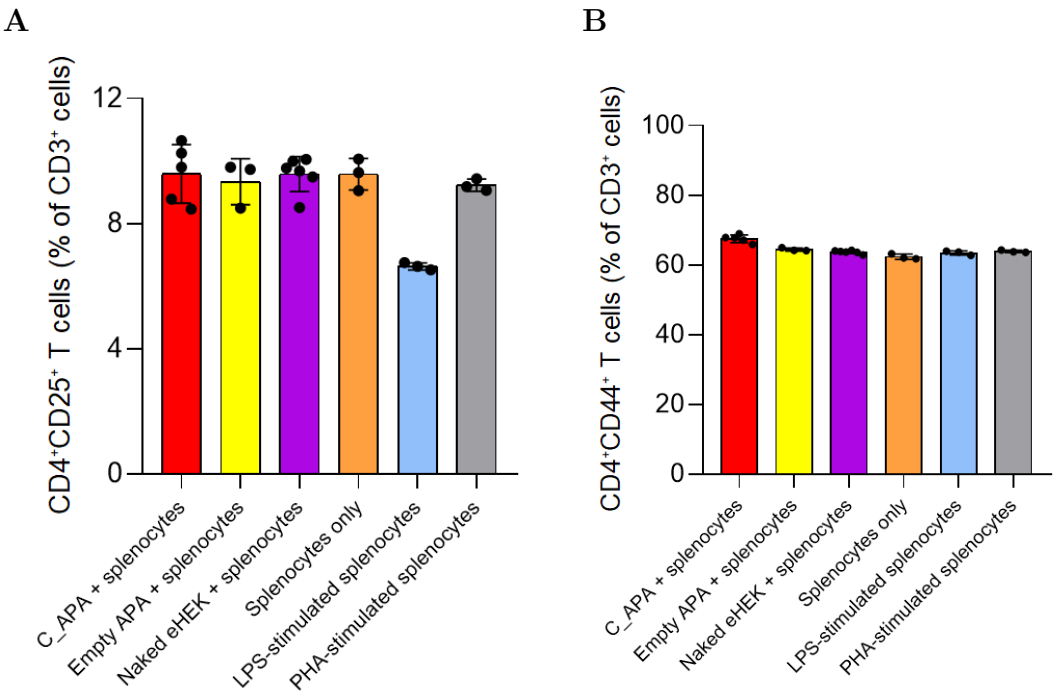


Figure 3.16: Flow-cytometric assessment of activation-associated markers in primary rat $CD3^+$ T cells following the immune challenge. (A) $CD4^+CD25^+$ cells expressed as a percentage of $CD3^+$ T cells. (B) $CD4^+CD44^+$ cells expressed as a percentage of $CD3^+$ T cells. Individual points represent evaluable wells and bars show mean ± SD. One sample from the cell-loaded APA + splenocyte group was excluded because of failed flow-cytometric acquisition. The limited separation of the PHA positive-control condition was taken into account when interpreting both activation-associated readouts.

validated quantitative proliferation endpoint, CFSE fluorescence was not subjected to comparative quantitative analysis.

A representative flow-cytometric gating strategy from the splenocyte-only control condition is shown in Figure 3.17. Events were first selected according to forward- and side-scatter characteristics, followed by singlet discrimination and exclusion of cells positive for the LIVE/DEAD viability dye. $CD45^+$ leukocytes and subsequently $CD3^+$ T cells were identified before analysis of the $CD4^+CD25^+$ and $CD4^+CD44^+$ populations. Taken together, the primary splenocyte challenge provided complementary information on inflammatory signaling, engineered-cell function, and immune-cell status. The TNF-α assay found higher early TNF-α in the APA co-cultures, but the LPS positive control worked as expected, and splenocyte health was mostly maintained in the main test groups. SEAP levels really shot up during immune co-culture - especially for engineered cells inside APA capsules. On the other hand, the T-cell activation and proliferation results just weren't clear enough (even in the positive-control groups) to say much about adaptive immune

activation. These findings therefore provide a preliminary characterization of the interaction between the APA system and primary immune cells, but do not by themselves demonstrate complete immunoisolation or immunoresistance.

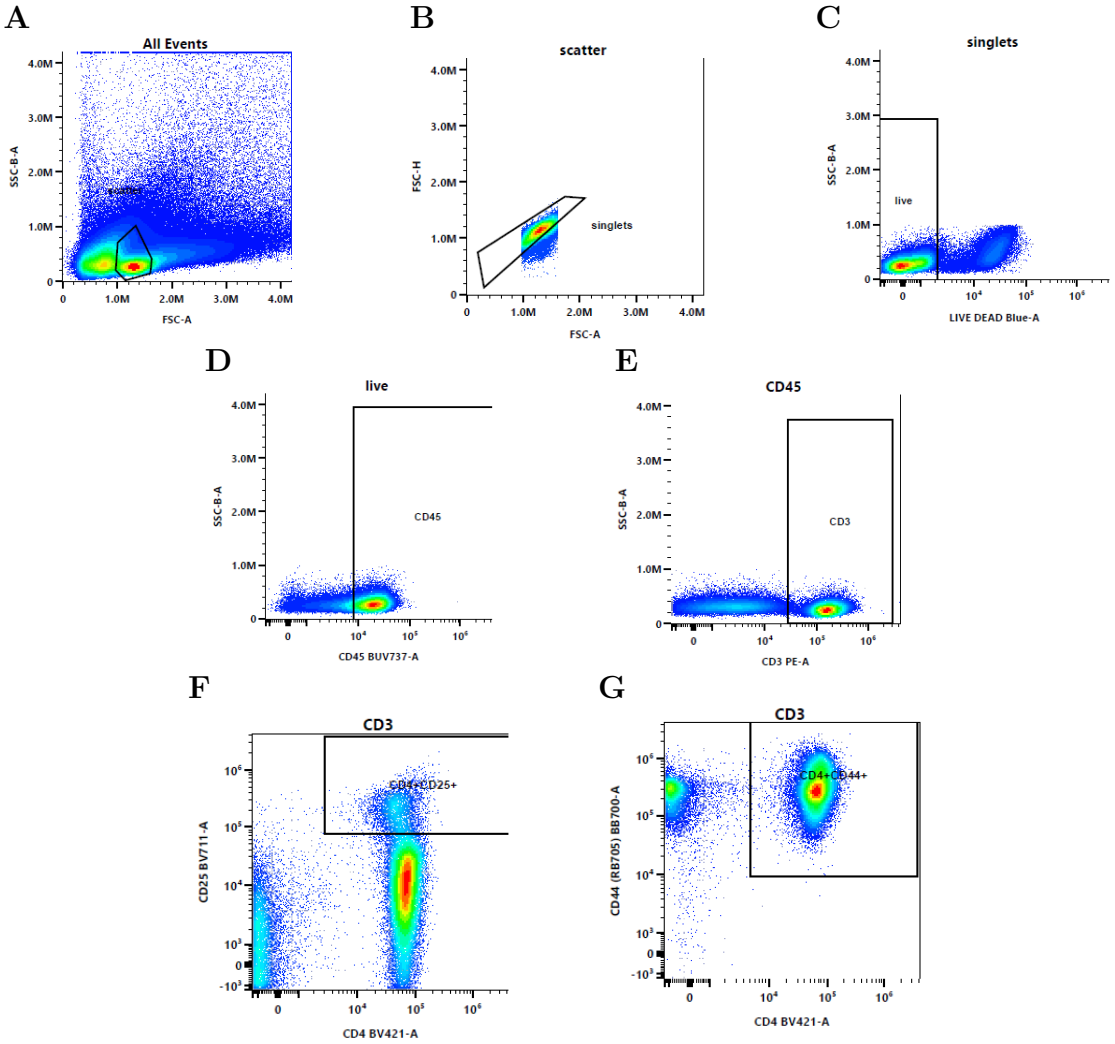


Figure 3.17: Representative flow-cytometric gating strategy used for analysis of primary rat splenocytes. The example shown corresponds to a splenocyte-only control sample. (A) Initial selection based on forward- and side-scatter characteristics. (B) Singlet discrimination using FSC-A and FSC-H. (C) Identification of live cells using LIVE/DEAD Fixable Blue. (D) Selection of $CD45^+$ leukocytes. (E) Identification of $CD3^+$ T cells within the $CD45^+$ population. (F) Identification of the $CD4^+CD25^+$ population within $CD3^+$ T cells. (G) Identification of the $CD4^+CD44^+$ population within $CD3^+$ T cells.

3.5 Integration of APA Microcapsules into the Redesigned BioHybrid Device

Following the in vitro characterization of APA microcapsules, the encapsulation strategy was integrated into the redesigned BioHybrid cellular compartment. Device-level evaluation focused on three aspects: dimensional assessment of the initially proposed 3D-printed retention mesh, practical loading and retention of APA microcapsules within the redesigned chamber, and functional detection of SEAP released from the encapsulated cellular payload into the surrounding medium.

3.5.1 Evaluation of the 3D-Printed Retention Mesh

An initial device design incorporated the capsule-retention mesh directly into the 3D-printed cellular compartment, with nominal openings of approximately 200 μm. Surface and optical analysis using the Keyence profiler showed a lot of size variation in the printed structures (see Figure 3.18A–C). When looking at individual pores in the mesh, the size range overlapped quite a bit with what was measured for APA microcapsule diameters (Figure 3.18D).
Because some printed openings approached the diameters of the smallest APA capsules, the mesh couldn't be considered reliable for capsule retention. The integrated 3D-printed mesh was therefore not pursued as the final retention interface. Instead, a separate nylon mesh with a nominal opening size of approximately 100 μm was selected. This dimension remained substantially below the observed APA capsule diameter range while providing a considerably more open interface than the 30-nm PES membrane used in the previous naked-cell device configuration.

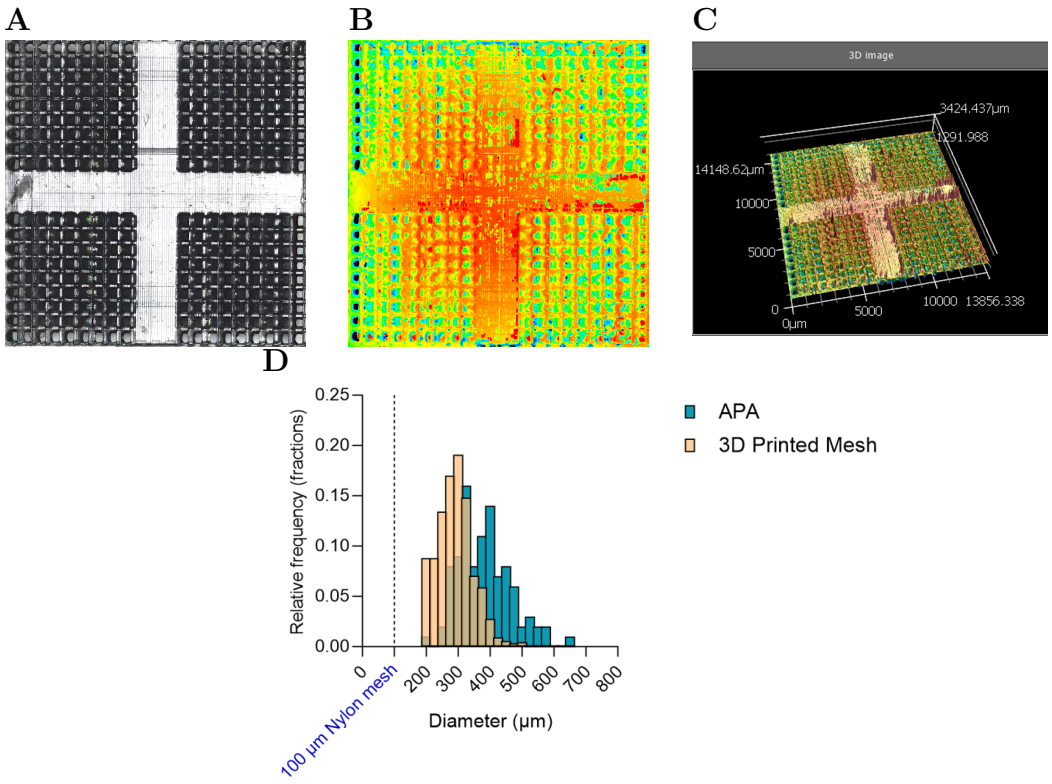


Figure 3.18: Characterization of the initially developed 3D-printed capsule-retention mesh and comparison with the APA microcapsule size distribution. (A) Representative optical image of the printed mesh acquired using the Keyence optical profiling system. (B) Corresponding surface-height map. (C) Three-dimensional reconstruction of the analyzed mesh region. (D) Distribution of individual 3D-printed mesh pore diameters compared with the experimentally measured APA microcapsule diameter distribution. The dashed vertical line indicates the nominal 100 μm opening of the nylon mesh subsequently selected for the redesigned device. The overlap between the printed pore-size distribution and the lower range of APA capsule diameters supported replacement of the integrated mesh with the independent 100 μm nylon retention mesh.

3.5.2 APA Loading and Retention within the Redesigned Cellular Chamber

APA microcapsules could be introduced through the single self-sealing loading port and positioned within the cellular compartment between the opposing platinum-mesh electrodes. While loading, the internal medium moved through the nylon membrane, so the chamber could be filled without needing a second vent port. After injecting, a quick look showed microcapsules were inside the chamber, with no big air bubbles or any visible capsule leaks past the outer mesh.
They made sure to load devices based on the actual number of APA microcapsules per chamber, not just an estimate of how many cells each capsule held. In untreated devices, there were 72.0 ± 14.1 beads each; devices in the 60 mM KCl group had 68.7 ± 9.5 beads per device. Because both groups had about the same average capsule count, it made sense to compare and normalize SEAP output by beads for each device afterward.
This showed it was practical to load and keep the APA microcapsules inside the new compartment design. The loading procedure was interpreted as a practical feasibility assessment rather than as a quantitative retention-efficiency study, because complete post-experimental recovery of all loaded beads and direct calculation of a percentage retention efficiency were not performed as independent quantitative endpoints.

3.5.3 Device-Level SEAP Release across the Mesh-Based Interface

Functional molecular exchange across the redesigned BioHybrid cellular compartment was evaluated using APA-loaded devices maintained under untreated conditions or exposed to 60 mM KCl exclusively through the external surrounding medium. SEAP was quantified independently in the internal cellular compartment and in the external well medium. To account for device-to-device differences in capsule loading, the total SEAP amount recovered from each compartment was normalized to the number of APA microcapsules introduced into the corresponding device.
At Day 3, SEAP was detectable in both the internal and external compartments under untreated conditions (Figure 3.19). Recovery of reporter protein from the external medium showed that SEAP secreted by the encapsulated engineered cells was able to leave the internal cellular chamber and cross the redesigned mesh-based device boundary.
A substantially greater SEAP response was observed following external KCl exposure. Importantly, KCl had been added only to the surrounding 5 mL external medium and was not introduced directly into the 700 μL internal cellular compartment. The increase in SEAP output therefore indicates that the externally

applied ionic stimulus gained access to the cellular compartment and reached the APA-encapsulated engineered cells at a level sufficient to activate the depolarization-sensitive Ca^{2+}/NFAT pathway. When they later detected more SEAP in the outer compartment, it proved the secreted reporter could get out of the device after being triggered.

Together, the results show the device allows molecules to move both ways: small ions from the medium can get in, and the protein made by the encapsulated cells can get out. This represents an important distinction from the previous nanoporous device configuration, in which outward reporter recovery was strongly restricted. Nevertheless, the present experiment was designed as a proof-of-concept functional assessment and did not quantify KCl equilibration kinetics, SEAP permeability, diffusion coefficients, or the fraction of total secreted protein crossing the device boundary.

The normalized SEAP amount recovered from the external compartment was greater than that remaining within the internal compartment, particularly following KCl stimulation. This difference should not be interpreted as a direct concentration gradient because the two compartments had markedly different volumes (0.7 mL internally and 5 mL externally). Instead, the data indicate that a substantial amount of the reporter secreted by the APA-encapsulated cells was recoverable from the surrounding medium during the investigated culture period.

Taken together, these findings support the feasibility of mechanically retaining APA microcapsules within the redesigned BioHybrid architecture while preserving functional communication between the encapsulated cellular payload and its surrounding environment. The short-term device experiment therefore established the feasibility of combining APA-based cellular confinement with a substantially more open macroscopic retention interface.

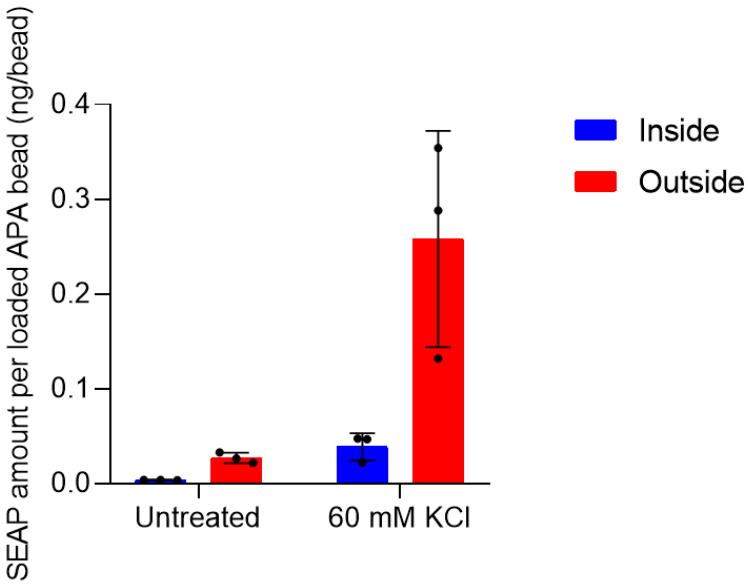


Figure 3.19: SEAP release from APA-encapsulated engineered HEK293 cells loaded into the redesigned mesh-based BioHybrid device at Day 3. Devices were maintained under untreated conditions or exposed to 60 mM KCl added exclusively to the external 5 mL surrounding medium; no KCl was added directly to the 700 μL internal cellular compartment. They measured SEAP levels separately inside and outside each compartment, normalizing the totals by loaded bead count and reporting as ng per bead. Single points are separate devices, and bars are mean $\pm$ SD ($n = 3$ for each type). The increased SEAP response following external KCl stimulation, indicates: that the ionic trigger reached the encapsulated cells, while detection of SEAP in the surrounding medium confirms outward reporter release.

Chapter 4

Conclusions

4.1 From Encapsulation to a Functional Electrogenetic Cell Platform

The aim of this thesis was to determine whether alginate–poly-L-lysine–alginate (APA) microencapsulation could provide a feasible alternative to direct loading of engineered cells into an implantable electrical-stimulation chamber. The work originated from limitations identified in the previous BioHybrid architecture, in which freely suspended engineered HEK293 cells depended largely on the macroscopic device itself for localization, retention, and separation from the surrounding environment. This configuration coupled cellular containment to a restrictive external membrane and provided limited control over the spatial organization of the cellular population. The strategy developed in this work instead transferred these functions, at least in part, to the individual cellular units by enclosing the electrogenetically engineered HEK293 cells within APA microcapsules. This created a hierarchical architecture in which the microcapsule provides local cellular confinement and the principal candidate immunoisolating interface, whereas the macroscopic device can primarily perform retention, stimulation, and technological integration.

The experimental results support the feasibility of this approach at several complementary levels. A reproducible fabrication workflow was established for the generation of alginate beads and their conversion into APA microcapsules. Quantitative morphometric analysis of representative optimized batches showed that the final APA structures exhibited a more regular and circular morphology than alginate-only beads, while subsequent batches produced under the same standardized fabrication conditions showed qualitatively comparable characteristics. The process therefore provided a sufficiently consistent encapsulation platform for the subsequent biological and functional studies, although the quantitative morphology dataset represented object-level measurements from representative batches rather

than independent batch-level replication.
Encapsulation was also compatible with maintenance of an active cellular population over the investigated culture period. Live/Dead microscopy was consistent with the persistence of Calcein-positive cells within APA microcapsules from Day 0 through Day 7, while longitudinal recovery from parallel alginate-only beads showed an increase in the recoverable cellular population during culture. Because mature APA capsules could not be reproducibly decapsulated and the recovery measurements were based on pooled samples and technical counting replicates, these observations cannot be interpreted as a direct quantitative measurement of proliferation within intact APA microcapsules. Nevertheless, together with the maintenance of metabolic activity and reporter secretion, they support the persistence of a functionally active cellular population following encapsulation.
The APA structure let engineered cells keep up their necessary molecular exchange with the outside world. Tests with fluorescent dextran tracers (from 3 to 70 kDa) showed that these molecules could make their way inside empty APA microcapsules - just more slowly as their size went up. So, while the measurements didn't pin down a hard permeability limit or a precise cut-off, they did show how transport changes depending on molecule size. The multilayer capsule wasn't a brick wall; it allowed movement across the range tested. This property was particularly relevant to the present application because both access of extracellular signals to the encapsulated cells and release of the engineered cellular product depend on transport through the surrounding hydrogel. More broadly, this behavior is consistent with the established view that transport across alginate-based immunoisolating capsules is governed by both molecular properties and capsule microstructure rather than by molecular weight alone [19, 12].
On the functional side, the engineered cells kept doing their job after being encapsulated. APA-encapsulated cells kept steadily releasing SEAP throughout a weeklong culture, and total reporter output stayed strong. Chemical depolarization with 60 mM KCl sent SEAP secretion way up, whether or not cells were in capsules. Within this study, KCl worked as an electrode-free positive control - proof that the Ca^{2+}/NFAT pathway still worked after APA encapsulation. Its use was therefore intended to confirm preservation of the engineered signaling circuit rather than to define a physiologically sustainable stimulation condition.
Electrical stimulation represented a more demanding functional test because encapsulation modifies the ionic, geometric, and spatial environment between the stimulating electrodes and the engineered cells. Preliminary C-Dish experiments with non-encapsulated cells demonstrated that reporter output depended strongly on both stimulation amplitude and exposure duration and that increasing voltage did not produce a proportional increase in SEAP secretion. The same general trade-off remained evident after encapsulation. Using the custom platinum-mesh

electrode configuration, APA-encapsulated cells retained measurable electrical responsiveness, with the strongest early reporter increase observed at 5 V among the conditions investigated. Increasing voltage was progressively associated with a reduction in cellular metabolic activity, while 20 V resulted in marked reductions in both metabolic activity and reporter output.
These findings demonstrate that APA encapsulation does not abolish electrical responsiveness of the engineered HEK293 platform. However, the stimulation conditions evaluated in this thesis did not identify a definitive operating point capable of simultaneously producing a strong and sustained SEAP response while preserving high cellular metabolic activity. The electrical experiments should therefore be considered an initial definition of a device-relevant stimulation window rather than an optimized stimulation protocol. Identification of this balance represents one of the principal unresolved technical challenges of the platform. The need to define such an operating window is consistent with the broader electrogenetic literature, in which stimulation intensity, duration, waveform, and electrical modality are treated as system-defining parameters that must be optimized together with cellular function [15, 17, 29].
Taken together, the structural, transport, and functional experiments support the ability of APA encapsulation to meet the principal requirements of the engineered cellular component: physical confinement, persistence of metabolically active cells, molecular accessibility, constitutive reporter secretion, and preservation of chemically and electrically inducible function. But the results highlight that the system's parts are tightly linked. How the capsule is built and how molecules get in and out affect how cells get nutrients and activation signals. How you stimulate the cells doesn't just change the end result - it can shift the cell's metabolism too. So, APA capsules aren't just passive containers for engineered cells; they act as active biological interfaces. This interpretation also aligns with contemporary biohybrid design principles, which emphasize co-design of the cellular, biomaterial, and electronic components rather than optimization of each subsystem in isolation [4].

4.2 Integration of the APA Strategy into the BioHybrid Device

The second major contribution of this thesis was the translation of the encapsulation strategy from an isolated in vitro platform into the redesigned BioHybrid cellular compartment. This required reconsidering how the principal functions of the system were distributed between the microcapsule and the macroscopic device. In the previous naked-cell configuration, the external 30-nm PES membrane simultaneously contributed to cellular containment, host separation, and molecular exchange.

Because APA encapsulation provides direct confinement of the engineered cellular population and constitutes the principal candidate immunoisolating interface, the redesigned device could instead employ a substantially more open external structure whose primary function was mechanical retention of the microcapsules. This distribution of functions is conceptually consistent with hybrid cell-encapsulation strategies in which local immunoprotection and cellular confinement are combined with a retrievable macroscopic device that provides positioning, handling, and integration with the surrounding host environment [14, 2, 4].
The first proposed solution consisted of an approximately 200 μm retention mesh integrated directly into the 3D-printed cellular chamber. Profilometric characterization demonstrated substantial variability in the dimensions of the printed openings and showed overlap between the pore-size distribution and the lower range of the APA microcapsule diameter distribution. This configuration was therefore considered unsuitable for reliable capsule retention. The result also highlighted a practical manufacturing constraint: nominal CAD dimensions cannot necessarily be translated into reproducible small-scale printed features when the design approaches the resolution limits of the fabrication process.
The integrated printed mesh was consequently replaced by a separate nylon mesh with nominal openings of approximately 100 μm. This design also made it easier to keep capsules separated from the rest of the population, while keeping things more open than the tight nanoporous PES membrane used before. In this setup, the nylon mesh holds capsules inside the chamber, and the APA capsules are intended to provide the main immunoisolating interface, while the nylon mesh, primarily, provides mechanical retention. Moving containment to the APA capsules is a sharp shift from the previous open-cell setup.
The redesigned chamber could subsequently be loaded through a single self-sealing silicone port, and APA microcapsules could be introduced and visually retained within the interelectrode region. The final device-level experiment was intentionally designed as a short-term in vitro proof-of-concept rather than as an attempt to reproduce the approximately 40,000-cell payload previously used for naked-cell loading or to establish long-term device performance. Capsule loading was therefore standardized primarily according to the number of microcapsules introduced into each chamber, allowing practical loading, retention, and molecular exchange through the redesigned architecture to be evaluated.
The Day 3 experiment provided functional evidence that communication between the encapsulated cellular population and the external environment remained possible after device integration. SEAP produced by the engineered cells was recovered from the external 5 mL medium, demonstrating outward transport of the secreted reporter from the internal cellular compartment. Importantly, in tests, the 60 mM KCl stimulus was only added outside the device - none went straight into the chamber. Yet SEAP secretion still rose, backing up that signals from outside could

reach the cells, and that the cells could respond from within. Taken together, these findings show there's two-way functional molecular exchange in the new system: an outside ionic signal can reach the encapsulated cells, and SEAP protein can make its way back out. But these data shouldn't be mistaken for exact permeability or molecular transport measurements - instead, they address whether swapping out the old nanoporous interface for a mesh and APA combo keeps capsules inside while still letting in and out what matters biologically
Within the short experimental period investigated, this requirement was supported at a proof-of-concept level. The redesigned architecture therefore supports the broader concept underlying this thesis: instead of requiring a single macroscopic membrane to provide cellular retention, immunological protection, and molecular transport simultaneously, these functions can be distributed across different physical scales. APA microcapsules provide local confinement of the engineered cellular population, while the macroscopic mesh retains the capsules within a retrievable and electrically addressable device and maintains a comparatively open interface with the external environment. The resulting architecture therefore reflects a broader design principle in cell-based implants: selective biological protection can be positioned close to the cellular payload while the macroscopic device provides retrieval, spatial organization, and technological integration without necessarily serving as the principal molecular barrier [2, 4].

4.3 Limitations and Concluding Remarks

The conclusions of this thesis must be interpreted within the scope of an in vitro proof-of-concept study. Quantitative morphometric characterization was based on representative optimized batches rather than independent quantitative batch-level replication, while longitudinal cell recovery relied on alginate-only beads because mature APA microcapsules could not be reproducibly dissolved under the same conditions. The resulting recovery measurements therefore provided an operational estimate of the recoverable cellular population rather than a direct determination of the absolute number or proliferation rate of cells within intact APA microcapsules. Similarly, the dextran tracer test gives only a relative sense of how well different molecules can get through APA - not an exact number for permeability or diffusion. Tracers as large as 70 kDa made it through, but that doesn't guarantee all biologically relevant molecules will act the same way under real conditions.
The main functional challenge here cropped up with electrical stimulation. Encapsulated HEK293 cells still responded to electrical cues, but the settings tested didn't give both a big SEAP output and healthy, active cells at the same time. Mild voltage barely budged the reporter, while stronger shocks started to wear the cells down and hurt their ability to produce SEAP at all. Further optimization

will therefore require systematic evaluation of stimulation amplitude, duration, frequency, waveform, current delivery, electrode geometry, and repeated-stimulation schedules using the final APA-compatible configuration. Establishing an operating window that produces a sufficiently strong functional output without compromising the long-term state of the encapsulated cellular population remains a major prerequisite for further development of the electrogenetic platform [15, 17, 29].
Another big question mark is how well this APA setup guards against immune attacks. The RAW 264.7 macrophage test and the follow-up with primary rat splenocytes were initial screens before moving into animal studies. The macrophage assay showed no reliably quantifiable increase in TNF-α, during the first 24 hours, followed by increased TNF-α concentrations at 72 hours, then the splenocyte experiment brought in a more varied immune-cell group, letting researchers check things like cytokine production, splenocyte health, markers of activation, and SEAP release all at once. These tests were useful starting points, but not enough to decide if APA capsules can really provide solid immunoprotection in a living animal.
Specifically, the T-cell and CFSE data didn't show clear enough differences in positive controls to confirm anything definite about adaptive immune activation or cell proliferation. More than that, a capsule in an animal faces a totally different environment from what's possible with short in vitro experiments. Recruitment of innate and adaptive immune cells, protein adsorption, fibrotic overgrowth, local vascularization, cytokine gradients, mechanical stress, capsule stability, and chronic foreign-body responses must ultimately be evaluated in vivo before the immunoisolating performance of the APA formulation can be established [21, 9, 13, 10].
The planned in vivo rat studies were not performed within the timeframe of this thesis. This progression was deliberately postponed until sufficiently informative in vitro data had first been obtained for capsule fabrication, cell function, molecular transport, immune-cell interaction, and device integration. The primary splenocyte challenge therefore represented an intermediate step between simplified in vitro immune screening and future in vivo evaluation rather than a substitute for animal implantation. Consequently, the present results should be interpreted as evidence of preliminary immunocompatibility and feasibility, not as demonstration of complete immunoisolation or long-term immunoresistance.
The same limitation applies to the redesigned BioHybrid device. Device integration was only checked in vitro and just for a few days, with most measurements at Day 3. These trials showed capsules could be loaded and kept in place, responded to ionic signals, and released SEAP protein to the outside. But since there hasn't been testing after implantation, we still can't say much about whether capsules stay put long term, how they interact with real tissue, if they trigger fibrosis, what in vivo exchange looks like, how the cells behave over time, or what happens between the mesh and host tissue over weeks or months.

For an integrated bioelectronic implant, long-term validation must also address the abiotic components of the system. Fluid ingress, packaging integrity, long-term electrical stability, and power delivery can become limiting independently of the biological payload and must therefore be evaluated together with cellular and immunological performance [25, 27, 4].
An in vivo rat study will therefore be required not only to determine whether APA microcapsules provide sufficient protection to the engineered cellular payload, but also to evaluate the integrated biological and engineering behavior of the redesigned device. In this context, immunoprotection and device performance cannot be considered independent questions: cellular survival, local host response, capsule integrity, molecular transport, and accessibility of the encapsulated cells to electrical stimulation will all contribute to the long-term performance of the implanted system.
Within these limitations, the overall objective of this thesis was achieved. A reproducible APA-based workflow was established for encapsulating electrogenetically engineered HEK293 cells, and the resulting microcapsules supported the persistence of a functionally active cellular population, molecular exchange, reporter secretion, chemical activation, and preliminary electrical responsiveness. The encapsulated cells could subsequently be incorporated into a redesigned BioHybrid cellular chamber using a 100 μm nylon retention interface, where they remained functionally accessible to the surrounding environment and released their engineered output across the device boundary.
The principal contribution of this work is therefore not the optimization of a single biomaterial or device component, but the development and experimental validation of a multiscale cell-loading strategy in which microencapsulation and macroscopic device retention perform complementary functions. By transferring cellular confinement and the principal candidate immunoprotective interface to the level of the individual APA microcapsule, the BioHybrid architecture can employ a more permissive external boundary while retaining the engineered cellular payload within a retrievable and electrically addressable device.
The present work consequently establishes a foundation for further development of the platform while clearly identifying its two most important unresolved requirements: optimization of electrical stimulation to achieve a favorable balance between induced secretory output and cellular preservation, and demonstration of effective long-term immunoprotection and integrated device function in vivo.

Chapter 5

Future Perspectives

5.1 Optimization and Repetition of the Primary Splenocyte Challenge

Before progressing to in vivo implantation, the interaction between APA microcapsules and primary immune cells should be reassessed using an optimized splenocyte co-culture protocol. The primary rat splenocyte experiment performed in this thesis provided an important intermediate step between the simplified RAW 264.7 macrophage model and future animal studies, but several immune endpoints were not sufficiently robust to support definitive conclusions regarding adaptive immune activation or proliferation.

A repeated experiment should therefore retain the general comparison between cell-loaded APA microcapsules, empty APA microcapsules, naked engineered HEK293 cells, and the corresponding immune-cell controls, while improving the analytical conditions used for T-cell activation and proliferation. Particular attention should be given to the positive-control conditions, since the PHA-treated samples did not provide sufficiently clear separation in the CD25, CD44, and CFSE readouts during the first experiment. Optimization of stimulant concentration, exposure duration, flow-cytometry timing, and CFSE labeling and acquisition conditions should therefore precede repetition of the complete assay.

The repeated study should also aim to increase biological replication and confidence in the reproducibility of the immune-cell response. Cytokine production, splenocyte viability, activation-associated phenotypes, and proliferation should be interpreted together rather than as isolated endpoints. In parallel, SEAP secretion from the engineered-cell population should continue to be monitored to determine whether immune-cell exposure alters the functional state of the encapsulated cells.

The objective of this second splenocyte study would not be to demonstrate complete immunoisolation in vitro, which cannot be established in a simplified co-culture

system, but to obtain a more reliable indication of whether APA encapsulation attenuates immune-mediated effects on the engineered cellular payload. Immunoisolation depends on both exclusion of direct immune-cell contact and control of soluble inflammatory mediators and host–material interactions that cannot be fully reproduced in a simplified in vitro model [2, 12, 19, 21, 9]. A robust in vitro immune dataset would therefore provide a stronger rationale for subsequent implantation experiments.

5.2 Long-Term In Vitro Validation of the APA-Loaded Device

Following short-term demonstration of APA loading and molecular exchange through the redesigned device, the next engineering step should be an extended in vitro study of the complete APA-loaded cellular chamber. The Day 3 experiment performed in this thesis supported the feasibility of introducing and retaining microcapsules over the short experimental period within the redesigned compartment and showed that molecular communication between the internal chamber and the external environment remained possible. Longer-term experiments are required to determine whether these properties remain stable during repeated manipulation and prolonged culture.

Long-term validation should include assessment of APA microcapsule integrity inside the device. Capsule morphology, rupture, deformation, aggregation, and retention should be monitored over time to determine whether prolonged confinement within the chamber or repeated experimental handling produces mechanical damage. Long-term structural stability is particularly relevant for alginate-based immunoisolation systems because swelling, degradation, defects, or loss of capsule integrity can alter both cellular containment and molecular transport [12, 21, 16, 2]. This detail matters because the capsules sit in a pretty tight space between the electrodes and need to hold up for as long as the device is working.

The self-sealing silicone loading and sampling port also deserves a look after repeated use. In the planned setup, a small-gauge needle and limited sampling volume should be evaluated to determine whether, internal supernatant can be withdrawn without aspirating or damaging microcapsules of APA. Repeated sampling cycles should therefore be performed to determine whether the port maintains its ability to reseal after multiple punctures and whether progressive leakage, structural damage, or contamination of the chamber occurs.

The sampling procedure should simultaneously be evaluated for its compatibility with the encapsulated payload. Withdrawal of internal supernatant should be performed using a needle and sampling volume sufficiently small to avoid aspiration or mechanical disruption of the APA microcapsules. By sampling like this multiple

times, you can track SEAP levels in the internal compartment over time, and at the same time check if the capsules are still intact and where they're supposed to be after the device has been used again and again. Over the long haul, it's important to keep an eye on SEAP concentrations and (if it makes sense) the actual amounts in both the inner and outer parts of the device. Add to that occasional checks of how capsules are arranged, whether the chamber is still solid, how the nylon mesh is holding up, and what shape the silicone port is in. At selected endpoints, metabolic activity and capsule morphology should additionally be evaluated. Long-term monitoring is particularly important for engineered-cell implants because cellular state, transgene expression, secretion, and responsiveness can change during prolonged culture or implantation [1, 2]. This experiment would therefore provide information not only on long-term cellular function but also on the operational robustness of the complete sampling and retention architecture.

5.3 Repeated Electrical Stimulation in the Fully Integrated APA Device

Once long-term mechanical stability of the APA-loaded chamber has been demonstrated, the next step should be integration of repeated electrical stimulation into the complete device configuration. The experiments performed in this thesis demonstrated electrical responsiveness of APA-encapsulated cells using a custom platinum-mesh setup and separately demonstrated functional molecular exchange after loading the capsules into the redesigned BioHybrid chamber. Previous electrogenetic and electronically actuated designer-cell systems have demonstrated that engineered mammalian cells can be remotely controlled within implantable or encapsulated configurations, supporting the feasibility of combining cellular encapsulation with technological actuation [15, 17, 23, 24]. Future work should combine these two elements within the same fully integrated system.
The complete device should therefore be loaded with APA-encapsulated engineered HEK293 cells, equipped with the final platinum-mesh electrode configuration, and subjected to repeated electrical stimulation cycles over an extended culture period. This experiment should use electrical stimulation as the principal activation strategy, with KCl retained only as a positive functional control where appropriate, and reproduce as closely as possible the intended operating conditions of an implanted electrogenetic device.
A major objective will be to determine whether the encapsulated cells remain repeatedly inducible rather than merely responsive to a single stimulation event. SEAP output should be quantified after successive stimulation cycles, while basal secretion between activations should be monitored to determine whether repeated electrical exposure alters the background activity of the engineered Ca^{2+}/NFAT

pathway. Particular attention should be given to progressive changes in response magnitude that could indicate cellular adaptation, functional exhaustion, or cumulative electrical stress. Long-term preservation of stimulus responsiveness is a central requirement for engineered-cell therapeutic systems intended for repeated or chronic activation [1, 4].
Electrical stimulation should be evaluated together with cellular metabolic activity and capsule integrity. The stimulation parameters explored in the present thesis did not identify a definitive condition that combined strong SEAP induction with preservation of high metabolic activity. Future optimization should therefore consider not only voltage amplitude but also current delivery, pulse duration, frequency, waveform, stimulation duration, inter-stimulation interval, and total number of repeated activation cycles. These parameters can substantially influence the magnitude and tolerability of electrogenetic activation and have been shown to affect engineered-cell responses in electrically controlled mammalian systems [15, 17, 29, 4].
Direct electrical characterization of the APA-loaded device would also be important. Measurement of the current delivered under the final chamber geometry would provide a more informative experimental descriptor of the delivered stimulation than applied voltage alone, since the electrical environment depends on electrode spacing, exposed area, medium volume, capsule distribution, and ionic conductivity [4, 5].
The combined long-term and repeated-stimulation experiment would represent a key in vitro validation step before implantation. Demonstration that APA microcapsules remain structurally intact, that the silicone port tolerates repeated sampling, and that the encapsulated cells maintain electrically inducible SEAP secretion over multiple cycles would provide a substantially stronger basis for subsequent in vivo evaluation.

5.4 In Vivo Validation of Immunoprotection and Integrated Device Performance

Following optimization of the in vitro immune assay and demonstration of long-term device stability under repeated electrical stimulation, the redesigned BioHybrid platform should be evaluated in vivo. A rat implantation study would represent the critical next step for determining whether the APA microcapsules provide sufficient protection to the engineered cellular payload and whether the complete device remains functional within a physiological environment. In vivo performance cannot be inferred from in vitro molecular-transport measurements through the capsules or short-term immune-cell co-culture alone because the implanted system is exposed simultaneously to inflammatory, fibrotic, transport, and tissue-integration processes

[2, 9].
The in vivo study should evaluate the local foreign-body response generated by both the APA microcapsules and the macroscopic device. Histological examination of the implantation site should assess inflammatory-cell recruitment, macrophage accumulation, foreign-body giant-cell formation, fibroblast infiltration, extracellular-matrix deposition, and development of a fibrotic capsule around the implant. The thickness and organization of fibrotic tissue would be particularly relevant because even a biologically tolerated implant may become functionally compromised if a dense fibrotic layer increases the transport distance between the surrounding vasculature and the encapsulated cells [21, 9, 13, 10, 2].
It's also worth looking into how the host tissue reacts to the roughly 100 μm nylon mesh. Unlike the old nanoporous membrane, this mesh doesn't keep out host cells, so inflammatory and stromal cells can move right up to the outer surface of the capsules. In live studies, it should be clear if this setup causes cells to move into the mesh, cluster around individual capsules, or start building up scar tissue that could slow down molecular exchange. Pericapsular cellular adhesion and fibrotic overgrowth are well-established limitations of alginate-based transplantation systems and can strongly influence long-term graft function [9, 10].
At the systemic level, SEAP should be monitored in blood as a functional indicator of whether the engineered reporter produced within the device can cross the APA and device interfaces and reach the circulation. Longitudinal blood sampling would allow assessment of basal reporter availability and, following electrical stimulation, whether a measurable increase in circulating SEAP can be detected. Detection of a systemically accessible engineered output following electrical activation has previously been demonstrated in implantable electrogenetic systems and provides a relevant precedent for this type of functional evaluation [15, 17].
The implanted device should also be evaluated after explantation. Retrieved APA microcapsules should be examined for structural integrity, morphology, cellular viability, and preservation of the engineered phenotype. If possible, taking out the capsules and testing them again outside the body could show whether they still respond to electrical signals after time spent implanted. The device should also be checked to see if the nylon mesh, silicone port, electrodes, and chamber are all still intact.
Comparing how viable and functional the cells are before and after they go in, along with looking at tissue samples, would help sort out whether problems are caused by the biology itself or by how the body is reacting to the device. Similarly, histological evidence of inflammation or fibrosis should be interpreted together with systemic SEAP measurements and post-explant functional assays. This integrated analysis would provide a more meaningful evaluation of device performance than any single endpoint alone.
Ultimately, the in vivo study should answer two central questions that remain

unresolved after the present thesis: whether APA microcapsules provide sufficient long-term immunoprotection to preserve the engineered cellular payload, and whether the complete BioHybrid device can maintain functional molecular exchange and electrically controlled secretion after implantation.

5.5 Toward a Therapeutic and Closed-Loop BioHybrid System

SEAP was used throughout this thesis as a reporter of activation of the engineered electrogenetic pathway and not as the intended therapeutic output. Once long-term cellular survival, immunoprotection, device stability, and repeated electrical responsiveness have been demonstrated, the platform could be adapted to control secretion of a therapeutically relevant protein. Engineered mammalian cells are increasingly being investigated as programmable therapeutic production platforms capable of coupling defined inputs to secretion of biologically active molecules [1, 4]. Such a transition would require renewed characterization because the molecular size, secretion kinetics, biological activity, required therapeutic concentration, and systemic half-life of the selected molecule may differ substantially from those of SEAP.

The transport behavior of the selected therapeutic product would therefore need to be evaluated directly through the APA microcapsule and the complete device architecture. Molecular transport through encapsulation systems depends not only on molecular size but also on barrier thickness, network structure, molecular charge, and interactions with the polymer matrix [12, 2]. The observed dextran penetration across the investigated molecular-weight range and recovery of SEAP outside the device provide a basis for this development but cannot substitute for molecule-specific transport and pharmacodynamic characterization.

Closed-loop regulation can also be implemented at the biological level. For example, glucose-responsive β-cell-mimetic designer cells have been engineered to couple a physiological metabolic input directly to therapeutic transgene expression, enabling autonomous correction of hyperglycemia in diabetic mice [30]. Such biologically self-regulated systems differ from the externally actuated electrogenetic strategy considered here, but they illustrate the broader potential of engineered mammalian cells to integrate sensing and therapeutic secretion within the same living component.

A further long-term objective would be integration of the electrogenetic cellular component into a closed-loop control system. The present BioHybrid concept provides externally controlled electrical actuation, but it does not yet autonomously determine when stimulation is required. A fully closed-loop configuration would incorporate a sensor capable of monitoring a relevant physiological variable, an

electronic controller that interprets the measured signal, and the existing electrical interface that activates the engineered cellular population when a predefined intervention is required [5, 4].

The resulting system would establish a complete functional sequence from physiological sensing to electronic decision-making, electrical stimulation, cellular activation, therapeutic-protein secretion, and subsequent physiological response. Such an architecture would exploit the complementary strengths of electronics and engineered cells: rapid and programmable sensing and control on the electronic side, together with the capacity for biological synthesis and secretion of complex therapeutic molecules on the cellular side [4, 5].

Different levels of such integration have already been demonstrated experimentally. Smartphone-linked optogenetic systems have coupled external digital control to engineered-cell activation, whereas glucose-powered metabolic fuel-cell platforms have moved toward self-sufficient bioelectronic operation by using the physiological variable itself as part of the energy and control architecture [7, 28].

Closed-loop translation should, however, follow rather than precede validation of the intermediate biological and engineering steps. Long-term immune protection, repeated electrical responsiveness, reliable molecular transport, device integrity, and predictable therapeutic output must first be established independently and then within the integrated implant. Existing electrogenetic studies provide proof of principle that electronic control can regulate engineered cellular outputs in vivo, but translation toward a durable closed-loop implant requires integration of sensing, control, actuation, transport, and long-term biological stability within the same platform [15, 17, 5]. The work presented in this thesis provides the initial biological and engineering foundation for this progression by demonstrating that APA-encapsulated electrogenetically engineered cells can be incorporated into a mechanically retained device architecture designed for electrical addressing.

References

[1] Caleb J. Bashor, Isaac B. Hilton, Hozefa Bandukwala, Devyn M. Smith, and Omid Veiseh. «Engineering the next generation of cell-based therapeutics». In: *Nature Reviews Drug Discovery* 21.9 (2022), pp. 655–675. DOI: 10.1038/s41573-022-00476-6 (cit. on pp. 1–3, 12–14, 102, 103, 105).

[2] Marco Farina, Jenolyn F. Alexander, Usha Thekkedath, Mauro Ferrari, and Alessandro Grattoni. «Cell encapsulation: Overcoming barriers in cell transplantation in diabetes and beyond». In: *Advanced Drug Delivery Reviews* 139 (2019), pp. 92–115. DOI: 10.1016/j.addr.2018.04.018 (cit. on pp. 1–6, 10, 11, 17, 96, 97, 101, 102, 104, 105).

[3] Haifeng Ye, Marie Daoud-El Baba, Ren-Wang Peng, and Martin Fussenegger. «A synthetic optogenetic transcription device enhances blood-glucose homeostasis in mice». In: *Science* 332.6037 (2011), pp. 1565–1568. DOI: 10.1126/science.1203535 (cit. on pp. 1, 13).

[4] Jonathan Rivnay, Ritu Raman, Jacob T. Robinson, Christian Schreib, Tzahi Cohen-Karni, Kate E. Galloway, and Omid Veiseh. «Integrating bioelectronics with cell-based synthetic biology». In: *Nature Reviews Bioengineering* 3 (2025), pp. 317–332. DOI: 10.1038/s44222-024-00262-6 (cit. on pp. 1, 3, 6–8, 11–15, 17, 18, 95–97, 99, 103, 105, 106).

[5] Marco M. Paci, Tamoghna Saha, Omeed Djassemi, Steven Wu, Corrine Ying Xuan Chua, Joseph Wang, and Alessandro Grattoni. «Smart closed-loop drug delivery systems». In: *Nature Reviews Bioengineering* 3.10 (2025), pp. 816–834. DOI: 10.1038/s44222-025-00328-z (cit. on pp. 1, 14, 15, 18, 103, 106).

[6] Marc Folcher et al. «Mind-controlled transgene expression by a wireless-powered optogenetic designer cell implant». In: *Nature Communications* 5 (2014), p. 5392. DOI: 10.1038/ncomms6392 (cit. on pp. 1, 17, 18).

[7] Jiawei Shao et al. «Smartphone-controlled optogenetically engineered cells enable semiautomatic glucose homeostasis in diabetic mice». In: *Science Translational Medicine* 9.387 (2017), eaal2298. DOI: 10.1126/scitranslmed.aal2298 (cit. on pp. 1, 13, 18, 106).

[8] Assem Ashimova, Sergey Yegorov, Baurzhan Negmetzhanov, and Gonzalo Hortelano. «Cell Encapsulation Within Alginate Microcapsules: Immunological Challenges and Outlook». In: *Frontiers in Bioengineering and Biotechnology* 7 (2019), p. 380. DOI: 10.3389/fbioe.2019.00380 (cit. on pp. 2, 4, 10).

[9] Omid Veiseh et al. «Size- and shape-dependent foreign body immune response to materials implanted in rodents and non-human primates». In: *Nature Materials* 14.6 (2015), pp. 643–651. DOI: 10.1038/nmat4290 (cit. on pp. 3, 4, 8, 9, 98, 101, 104).

[10] Matthew A. Bochenek et al. «Alginate encapsulation as long-term immune protection of allogeneic pancreatic islet cells transplanted into the omental bursa of macaques». In: *Nature Biomedical Engineering* 2.11 (2018), pp. 810–821. DOI: 10.1038/s41551-018-0275-1 (cit. on pp. 3, 5, 10, 98, 104).

[11] Clark K. Colton. «Oxygen supply to encapsulated therapeutic cells». In: *Advanced Drug Delivery Reviews* 67–68 (2014), pp. 93–110. DOI: 10.1016/j.addr.2014.02.007 (cit. on pp. 3, 6).

[12] Genaro Alberto Paredes Juárez, Milica Spasojevic, Marijke M. Faas, and Paul de Vos. «Immunological and Technical Considerations in Application of Alginate-Based Microencapsulation Systems». In: *Frontiers in Bioengineering and Biotechnology* 2 (2014), p. 26. DOI: 10.3389/fbioe.2014.00026 (cit. on pp. 3–11, 94, 101, 105).

[13] Arturo J. Vegas et al. «Combinatorial hydrogel library enables identification of materials that mitigate the foreign body response in primates». In: *Nature Biotechnology* 34.3 (2016), pp. 345–352. DOI: 10.1038/nbt.3462 (cit. on pp. 4, 9, 98, 104).

[14] Esther S. O'Sullivan, Arturo Vegas, Daniel G. Anderson, and Gordon C. Weir. «Islets transplanted in immunoisolation devices: a review of the progress and the challenges that remain». In: *Endocrine Reviews* 32.6 (2011), pp. 827–844. DOI: 10.1210/er.2010-0026 (cit. on pp. 5, 96).

[15] Krzysztof Krawczyk et al. «Electrogenetic cellular insulin release for real-time glycemic control in type 1 diabetic mice». In: *Science* 368.6494 (2020), pp. 993–1001. DOI: 10.1126/science.aau7187 (cit. on pp. 5, 12–18, 24, 95, 98, 102–104, 106).

[16] Raha Ahmad Raus, Wan Mohd Fazli Wan Nawawi, and Ricca Rahman Nasaruddin. «Alginate and alginate composites for biomedical applications». In: *Asian Journal of Pharmaceutical Sciences* 16.3 (2021), pp. 280–306. DOI: 10.1016/j.ajps.2020.10.001 (cit. on pp. 7, 8, 101).

[17] Jinbo Huang, Shuai Xue, Peter Buchmann, Ana Palma Teixeira, and Martin Fussenegger. «An electrogenetic interface to program mammalian gene expression by direct current». In: *Nature Metabolism* 5.8 (2023), pp. 1395–1407. DOI: 10.1038/s42255-023-00850-7 (cit. on pp. 8, 11–14, 95, 98, 102–104, 106).

[18] W. F. Kendall, M. D. Darrabie, H. M. El-Shewy, and E. C. Opara. «Effect of alginate composition and purity on alginate microspheres». In: *Journal of Microencapsulation* 21.8 (2004), pp. 821–828. DOI: 10.1080/02652040400015452 (cit. on p. 8).

[19] Bård Kulseng, Beate Thu, Terje Espevik, and Gudmund Skjåk-Bræk. «Alginate polylysine microcapsules as immune barrier: permeability of cytokines and immunoglobulins over the capsule membrane». In: *Cell Transplantation* 6.4 (1997), pp. 387–394. DOI: 10.1177/096368979700600405 (cit. on pp. 9, 94, 101).

[20] Berit L. Strand, Liv Ryan, Peter In't Veld, Bård Kulseng, Anne Mari Rokstad, Gudmund Skjåk-Bræk, and Terje Espevik. «Poly-L-lysine induces fibrosis on alginate microcapsules via the induction of cytokines». In: *Cell Transplantation* 10.3 (2001), pp. 263–275. DOI: 10.3727/000000001783986800 (cit. on p. 10).

[21] Gorka Orive, Susan K. Tam, José Luis Pedraz, and Jean-Pierre Hallé. «Biocompatibility of alginate–poly-L-lysine microcapsules for cell therapy». In: *Biomaterials* 27.20 (2006), pp. 3691–3700. DOI: 10.1016/j.biomaterials.2006.02.048 (cit. on pp. 10, 98, 101, 104).

[22] Sarah A. Stanley, Jeremy Sauer, Ravi S. Kane, Jonathan S. Dordick, and Jeffrey M. Friedman. «Remote regulation of glucose homeostasis in mice using genetically encoded nanoparticles». In: *Nature Medicine* 21 (2015), pp. 92–98. DOI: 10.1038/nm.3730 (cit. on p. 13).

[23] Haijie Zhao, Shuai Xue, Marie-Didiée Hussherr, Ana Palma Teixeira, and Martin Fussenegger. «Autonomous push button-controlled rapid insulin release from a piezoelectrically activated subcutaneous cell implant». In: *Science Advances* 8.24 (2022), eabm4389. DOI: 10.1126/sciadv.abm4389 (cit. on pp. 13, 14, 18, 102).

[24] Zhihua Lin, Preetam Guha Ray, Jinbo Huang, Peter Buchmann, and Martin Fussenegger. «Electromagnetic wireless remote control of mammalian transgene expression». In: *Nature Nanotechnology* 20.8 (2025), pp. 1071–1078. DOI: 10.1038/s41565-025-01929-w (cit. on pp. 15, 102).

[25] Enming Song, Jinghua Li, and John A. Rogers. «Barrier materials for flexible bioelectronic implants with chronic stability—current approaches and future directions». In: *APL Materials* 7.5 (2019), p. 050902. DOI: 10.1063/1.5094415 (cit. on pp. 17, 99).

[26] Emilie Audouard et al. «Bioelectronic cell-based device provides a strategy for the treatment of the experimental model of multiple sclerosis». In: *Journal of Controlled Release* 352 (2022), pp. 994–1008. DOI: 10.1016/j.jconrel.2022.11.008 (cit. on pp. 17, 18).

[27] Vishnu Nair, Ashley N. Dalrymple, Zhanghao Yu, Gaurav Balakrishnan, Christopher J. Bettinger, Douglas J. Weber, Kaiyuan Yang, and Jacob T. Robinson. «Miniature battery-free bioelectronics». In: *Science* 382.6671 (2023), eabn4732. DOI: 10.1126/science.abn4732 (cit. on pp. 18, 99).

[28] Debasis Maity, Preetam Guha Ray, Peter Buchmann, Maysam Mansouri, and Martin Fussenegger. «Blood-glucose-powered metabolic fuel cell for self-sufficient bioelectronics». In: *Advanced Materials* 35.21 (2023), p. 2300890. DOI: 10.1002/adma.202300890 (cit. on pp. 18, 106).

[29] Maysam Mansouri and Martin Fussenegger. «Electrogenetics: Bridging synthetic biology and electronics to remotely control the behavior of mammalian designer cells». In: *Current Opinion in Chemical Biology* 68 (2022), p. 102151. DOI: 10.1016/j.cbpa.2022.102151 (cit. on pp. 95, 98, 103).

[30] Mingqi Xie, Haifeng Ye, Hui Wang, Ghislaine Charpin-El Hamri, Claude Lormeau, Pratik Saxena, Jörg Stelling, and Martin Fussenegger. «β-cell-mimetic designer cells provide closed-loop glycemic control». In: *Science* 354.6317 (2016), pp. 1296–1301. DOI: 10.1126/science.aaf4006 (cit. on p. 105).

Self-declaration on the use of generative AI

Generative AI tools were used as support during the preparation of this thesis for language editing, text organization, readability, and refinement. The author reviewed all the data, interpretations, and decisions for this work, and checked all AI-assisted content against actual scientific sources. Full responsibility for the accuracy, originality, and integrity of this work falls to the author.